

## Department of Precision and Microsystems Engineering

### Scanning mirror redesign of the EasyScan retinal imaging system

Vilius Čechanavičius

Report no : 2020.060  
Coach : ir. J.P.Kappelhof  
Professor : Dr. N. Bhattacharya  
Specialisation : Optomechatronics  
Type of report : Master of Science Thesis  
Date : December 4, 2020



# Scanning mirror redesign of the EasyScan retinal imaging system

by

## Vilius Cechanavicius

to obtain the degree of Master of Science  
at the Delft University of Technology,  
to be defended publicly on Friday December 4, 2020 at 09:30 AM.

Student number: 4825306  
Project duration: September 17, 2019 – October 30, 2020  
Thesis committee: Dr. S.H. HosseinNia, TU Delft chair  
Dr. N. Bhattacharya, TU Delft  
Ir. J.P. Kappelhof, TU Delft supervisor  
Dr. E. van Dijk, EasyScan supervisor

*This thesis is confidential and cannot be made public until December 4th, 2022.*

An electronic version of this thesis is available at <http://repository.tudelft.nl/>.



# Abstract

EasyScan is a scanning system, which images the retina. The condition of the retina can help identify various diseases, such as glaucoma, diabetic retinopathy, cataract, macular degeneration and others. It is a commercially successful device that has sold thousands of units worldwide. However, the scanner is facing lifetime issues, as the scanner mirrors will become obsolete in the foreseeable future.

Possible ways of improving the optical system by reducing the required scan amplitude were investigated. Optical tests with fine pitch lenticular lenses, diffractive optical elements, and linear diffuser were conducted. No optical improvement was achieved; therefore, the scanner design was based on the functional requirements of the original system. Actuation methods and guiding mechanisms for low cost, low volume applications were studied. The proposed design for both the low frequency (LF) and high frequency (HF) scanners is a compact reluctance force actuated scanner mirror. However, design issues for the LF scanner guiding mechanism were encountered, that could not be solved in time. Nonetheless, a prototype of the HF scanner was finalized and managed to achieve the required  $\pm 3$  mrad amplitude at a frequency of 4650 Hz. The scanner was validated on an actual EasyScan optical module. However, reliability issues still need to be solved before making the scanner production ready, for which possible solutions are discussed.



# Preface

This thesis is written to achieve the Master's degree in Mechanical engineering for the programme of High-tech engineering with a focus in Opto-mechatronics. The thesis was conducted in collaboration with EasyScan and Hittech Multin. The first four months of the thesis were spent at EasyScan, whereas the rest of the project was conducted at Hittech Multin.

Firstly, I would like to thank my supervisor Pieter Kappelhof who made this thesis possible. Pieter always would find time to discuss issues, or directed me to someone who would help me to solve the issues, which made the whole process go smoothly. I would like to thank Erik van Dijk for giving me the opportunity to work on the EasyScan and trusting my ideas. Furthermore, I am grateful to everyone at Hittech Multin, who were very friendly, and would gladly help me out every step of the way. Also, I would like to thank Lennino Cacace and the whole TU Delft Opto-mechatronics group with whom we had really great discussions about each other's projects. Finally, I would like to thank my girlfriend Deimante, who moved with me to the Netherlands to support me on this journey, and had the patience to endure these two busy years.

*Vilius Cechanavicius  
Delft, November 2020*

# Contents

List of Figures	viii
List of Tables	xi
1 Introduction	2
1.1 Working principle of the EasyScan	2
1.2 Problem statement	4
1.3 System requirements	5
1.4 Driving electronics	6
1.5 Mirror dimensions	6
1.6 Amplitude requirement	7
1.7 Available space	7
1.8 LF scanner trajectory	8
1.9 Literature survey results	8
1.9.1 Scanning technologies	9
1.9.2 Intensity uniformity techniques	10
1.10 Project proposal	10
2 Intensity uniformity techniques	12
2.1 Linear diffusor	12
2.1.1 Experiments	13
2.2 Diffractive optical elements	13
2.2.1 Experiments	13
2.3 Lenticular lens	14
2.3.1 Experiments	15
2.4 Conclusion on optical solutions	16
3 System level scanner design	17
3.1 System level design outline	17
3.2 Desired mechanical properties of the scanner	17
3.3 Actuation methods	18
3.3.1 Piezo	18
3.3.2 Voice coil	20
3.3.3 Reluctance	22
3.3.4 Comparison	22
3.4 Guiding mechanisms	24
3.4.1 Bearings	25
3.4.2 Flexures	25
3.5 Scanner concept feasibility	27
4 Detailed scanner design	28
4.1 Detailed design outline	28
4.2 Magnetic design	28
4.2.1 Magnetic circuit selection	28
4.2.2 Magnetic circuit FEA comparison	31
4.2.3 Magnetic material general properties	33
4.2.4 Magnetically soft materials	33
4.2.5 Magnet selection	34
4.2.6 Side air gaps and cross section sizing	36
4.2.7 Coil yoke gap sizing	38
4.2.8 Coil design	39



4.2.9	Torque constant and magnetic stiffness . . . . .	41
4.2.10	Magnetic forces . . . . .	43
4.3	LF flexure stiffness and scanner dynamics . . . . .	43
4.4	HF flexure stiffness and scanner dynamics . . . . .	48
4.5	Mechanical design . . . . .	50
4.5.1	Flexure material selection . . . . .	50
4.5.2	Machinability considerations . . . . .	51
4.5.3	Flat torsion beam kinematics . . . . .	51
4.5.4	Flexure geometry design . . . . .	51
4.5.5	Fatigue stress . . . . .	52
4.5.6	HF flexure design . . . . .	52
4.5.7	Boundary condition influence to frequency . . . . .	58
4.5.8	Operational loads . . . . .	60
4.5.9	Shock loads . . . . .	62
4.5.10	LF flexure design . . . . .	63
4.5.11	U torsion beam for LF flexure . . . . .	64
4.6	Error budget and sensitivity analysis . . . . .	66
4.7	Finalized magnetic actuator . . . . .	68
4.8	Scanner assembly . . . . .	69
5	Design validation . . . . .	72
5.1	Validation outline . . . . .	72
5.2	Coil test . . . . .	72
5.3	Scanner amplitude measurement setup . . . . .	73
5.4	Scanner amplitude measurement results . . . . .	74
5.4.1	Yoke position influence . . . . .	74
5.4.2	Flexure model results . . . . .	75
5.4.3	Mounting influence on frequency . . . . .	77
5.4.4	Side air gap size influence . . . . .	78
5.4.5	Frequency dependence on amplitude . . . . .	78
5.4.6	Prototype test in the EasyScan OPMOD . . . . .	79
6	Conclusion and recommendations . . . . .	82
6.1	HF scanner . . . . .	82
6.2	LF scanner . . . . .	83
6.3	Scanner cost . . . . .	83
	Appendices . . . . .	84
A	Appendix Magnetic circuit basics . . . . .	86
A.1	Main relations and determination of magnetic flux . . . . .	86
A.2	Determination of force . . . . .	88
B	Appendix Piezo actuator technical data . . . . .	90
B.1	Maximum operational settings . . . . .	90
C	Appendix Magnetic circuit parameter expressions . . . . .	91
C.1	Configuration 1 . . . . .	91
C.2	Configuration 2 . . . . .	91
C.3	Configuration 3 . . . . .	91
C.4	Configuration 4 . . . . .	92
C.5	Configuration 5 . . . . .	92
D	Appendix Inertia of a rectangular body . . . . .	93
	Bibliography . . . . .	94

# List of Figures

1.1	Left: the EasyScan. Right:Image of the retina scanned with the EasyScan . . . . .	2
1.2	Schematic of main optical components of the EasyScan . . . . .	3
1.3	Light transmission from lenticular lens to the cylindrical lens and the projected Talbot Pattern. . . . .	3
1.4	Image of flat test target used during the optical alignment procedure of the OPMOD. On the left is an image produced when the HF mirror off. On the right is an image produced when the HF mirror on. Image on the left has an unacceptable quality. . . . .	4
1.5	Spatial beam relation comparison between a convex lens and a lenticular lens. From patent <i>NL2005253C2</i> by Michiel Herman Mensink and Julien Coyne, 2010, World Intellectual Property Organization . . . . .	4
1.6	Scanners currently used in the EasyScan . . . . .	5
1.7	Schematic showcasing parameters important for design . . . . .	5
1.8	Driving electronics of the HF scanner . . . . .	6
1.9	Driving electronics of the LF scanner . . . . .	6
1.10	Available scanner space for the HF and LF scanner . . . . .	8
1.11	Motion trajectory of the LF scanner . . . . .	8
1.12	Summary of contemporary scanning technologies with respect to the operational requirements of the HF and LF scanners . . . . .	9
1.13	Summary of intensity uniformity techniques discussed in the literature survey . . . . .	10
2.1	Tested optical elements . . . . .	12
2.2	Scanned test image comparison between the lenticular lens and the linear diffuser. . . . .	13
2.3	List of tested DOE models manufactured by <i>Holoeye</i> . . . . .	13
2.4	Scanned test image comparison between the lenticular lens and the DOE. . . . .	14
2.5	Left: Parameter table of lenticular lenses available from the current supplier. Right: Image of Talbot pattern with the half length and quarter length specified . . . . .	15
2.6	Scanned test image comparison between the original lenticular lens (pitch 0,3 mm) and the finest pitch lenticular lens (pitch 0,02 mm) . . . . .	15
2.7	Frequency content of a test image scanned with the original lenticular lens (pitch 0,3 mm) and with the finest pitch lenticular lens (pitch 0,02 mm) . . . . .	16
3.1	Sketch of a 1 DOF scanner configuration . . . . .	17
3.2	Left: Table with parameters of piezo actuators from <i>Physik Instrumente</i> . Right: Corresponding maximum piezo actuator operating current and power at the operational frequency of 4650 Hz. . . . .	19
3.3	Left: flexure actuated by a piezo into a resonant mode. Right: Figure of maximum inertial force generated by the piezo . . . . .	20
3.4	The smallest COTS voice coil of <i>Akribis</i> [24] . . . . .	20
3.5	Left: Voice coil configuration - cross-section view. Center: Voice coil configuration - top view. Right: Magnetic circuit of the voice coil configuration. . . . .	21
3.6	Left: Reluctance actuator configuration. Right: Magnetic circuit of reluctance actuator. . . . .	23
3.7	Computed output force and motor constant for the selected actuator configurations with additional relevant parameter . . . . .	24
3.8	Freedom and constraint spaces for a 1 DOF rotational flexure described by FACT methodology [29] . . . . .	25
3.9	Torsion beam concepts . . . . .	26
3.10	Cross flexure designs by <i>JPE B.V.</i> [7] . . . . .	26
3.11	Left: Butterfly flexure[30]. Right: Notch flexure. . . . .	27
4.1	Assumed flux and force direction for the configuration 4 magnetic circuit . . . . .	29
4.2	COMSOL model of magnetic circuit configuration 1. . . . .	31

4.3	Magnetic field density distributions of circuit configurations 1 and 4 . . . . .	31
4.4	Configuration 1+ based model and computed magnetic field . . . . .	32
4.5	Comparison of magnetic flux density of circuit configuration 4 with yoke material AISI430 and ARMCO, when the air gap size is $t = 0.5$ mm and the magnet is a 2 mm cube. . . . .	34
4.6	Demagnetisation curves of neodymium grades N52 and 42H [3] . . . . .	35
4.7	44H grade magnet torque/inertia ratio comparison with respect to the air gap size . . . . .	36
4.8	HF and LF scanner mover inertia with respect to flexure thickness . . . . .	36
4.9	Magnet clearance values for HF and LF scanner . . . . .	37
4.10	Left: Scanner yoke geometry with visualised sources of damping. Right: Topology of a torsional squeeze-film damper[35] . . . . .	38
4.11	Damping ratio of both damping sources evaluated for the HF scanner versus the gap distance . . . . .	38
4.12	Computed torques and forces acting on the scanner with a side gap of 1 mm and a current of 250 mA . . . . .	39
4.13	Flux linkage distribution with respect to excitation current and to mover rotation. . . . .	40
4.14	Actuator torque distribution with respect to actuation current and rotation angle . . . . .	42
4.15	Left: Actuator constant distribution with respect to current and rotation. Right: Negative magnetic stiffness distribution with respect to current and rotation. . . . .	43
4.16	Distribution of the magnetic forces acting on the magnet . . . . .	43
4.17	Desired LF scanner trajectory, velocity and acceleration plots . . . . .	44
4.18	Torque required to actuate the LF scanner in sawtooth motion. The total torque and spring torque are showcased separately . . . . .	45
4.19	LF scanner modelled with <i>Simscape</i> . . . . .	45
4.20	Voltage input of the LF scanner when $I_{LF} = 1 \times 10^{-9}$ kgm <sup>2</sup> , $\zeta = 5\%$ , $k_{LF} = 1.42 \times 10^{-2}$ Nm/rad, $R = 10.9\Omega$ . . . . .	46
4.21	Voltage input of the LF scanner when $I_{LF} = 1 \times 10^{-9}$ kgm <sup>2</sup> , $\zeta = 5\%$ , $k_{LF} = 1.70 \times 10^{-2}$ Nm/rad, $R = 10.9\Omega$ . . . . .	46
4.22	Angular position, velocity and acceleration of the LF scanner actuated from a stationary position when $I_{LF} = 1 \times 10^{-9}$ kgm <sup>2</sup> , $\zeta = 5\%$ , $k_{LF} = 1.70 \times 10^{-2}$ Nm/rad, $R = 10.9\Omega$ . . . . .	47
4.23	Plot of the resultant LF scanner angular velocity vs predicted velocity when $I_{LF} = 1 \times 10^{-9}$ kgm <sup>2</sup> , $\zeta = 5\%$ , $k_{LF} = 1.70 \times 10^{-2}$ Nm/rad, $R = 10.9\Omega$ . . . . .	47
4.24	LF scanner current when $I_{LF} = 1 \times 10^{-9}$ kgm <sup>2</sup> , $\zeta = 5\%$ , $k_{LF} = 1.70 \times 10^{-2}$ Nm/rad, $R = 10.9\Omega$ . . . . .	47
4.25	<i>Simscape</i> model of the HF scanner . . . . .	49
4.26	The rotation angle of the HF scanner when $I_{HF} = 1.09 \times 10^{-9}$ kgm <sup>2</sup> , $\zeta = 5\%$ , $f_{HF} = 4670$ Hz, $R = 10.9\Omega$ . . . . .	49
4.27	Current of the HF scanner when $I_{HF} = 1.09 \times 10^{-9}$ kgm <sup>2</sup> , $\zeta = 5\%$ , $f_{HF} = 4670$ Hz, $R = 10.9\Omega$ . . . . .	49
4.28	Generated EMF voltage of the HF scanner when $I_{HF} = 1.09 \times 10^{-9}$ kgm <sup>2</sup> , $\zeta = 5\%$ , $f_{HF} = 4670$ Hz, $R = 10.9\Omega$ . . . . .	50
4.29	Bode plot of the HF scanner, when the input is the voltage, and the output is the rotation angle. . . . .	50
4.30	Flexure sketch with visualised constraints . . . . .	51
4.31	HF scanner flexure sketch . . . . .	51
4.32	Unconstrained DOF of the flexure . . . . .	52
4.33	Fixation sketch of the unconstrained translational DOF . . . . .	53
4.34	Fixation sketch of the unconstrained rotational DOF . . . . .	53
4.35	HF flexure configurations for flexure material of AISI301 and titanium grade 5 at resonance frequency of 4670 Hz . . . . .	55
4.36	Computed HF flexure configurations that have higher order modes at least 6 times higher than first mode, and a maximum stress that is lower than the fatigue limit . . . . .	55
4.37	HF mirror position in the OPMOD . . . . .	56
4.38	Left:Preliminary HF flexure configuration. Right: Preliminary HF flexure configuration mounted in the housing. . . . .	56
4.39	FEA model assumptions and boundary conditions . . . . .	57
4.40	First mode of each of the selected flexure designs for stainless steel AISI 301 and titanium grade 5 . . . . .	57
4.41	Tapped joint stress distribution frustums used to determine joint stiffness . . . . .	58
4.42	FEA boundary condition comparison for AISI 301 flexure $t = 0.3$ mm; $w = 1.0$ mm; $l = 1.15$ mm . . . . .	59
4.43	First 5 modes of each flexure model . . . . .	60
4.44	Load schematic of HF scanner used in the dynamic analysis . . . . .	61

4.45 HF scanner stress and displacement when loaded by a $F = 0.131\text{ N}$ lateral force at a frequency of $f=4650\text{ Hz}$ . . . . .	61
4.46 HF scanner displacement frequency response when loaded by a $F = 0.137\text{ N}$ lateral force . . . . .	61
4.47 HF scanner stress frequency response when loaded by a $F = 0.137\text{ N}$ lateral force . . . . .	62
4.48 HF scanner stress frequency response when loaded by a $F = 0.137\text{ N}$ lateral force . . . . .	62
4.49 Flexure stresses due to a 25 G load in all three direction . . . . .	62
4.50 Available space around the LF mirror . . . . .	63
4.51 Computed results for AISI 301 when the higher order mode frequency factor is $f_{thumb} = 1, 3$ and the fatigue stress is $\sigma_{301} = 552\text{ MPa}$ . . . . .	64
4.52 U shaped cross-section of torsion beam . . . . .	64
4.53 Computed LF U shape torsion beam results for AISI 301 when the higher order mode frequency factor is $f_{thumb} = 10$ and the fatigue stress is $\sigma_{301} = 552\text{ MPa}$ . . . . .	65
4.54 CAD model of the LF flexure with the U shape torsion beam . . . . .	66
4.55 First five modes of the LF scanner with the U shape torsion beam . . . . .	66
4.56 Sensitivity analysis design variables . . . . .	67
4.57 Finalized HF scanner design . . . . .	68
4.58 Magnetic field density of the finalized HF scanner when the current is $I = 0.18\text{ A}$ . . . . .	69
4.59 Flexure gluing jig . . . . .	69
4.60 Left: Flexure in gluing jig with applied glue. Right: Mirror and magnet glued to flexure . . . . .	70
4.61 Left: Magnet centred with feeler gauges. Center: Flexure mounted in housing. Right: Front view of scanner . . . . .	70
4.62 Left: Manual coil winding assembly. Right: Wounded coil . . . . .	70
4.63 Left: Setting coil yoke position with feeler gauge. Right: Fully assembled HF scanner mounted in the OPMOD of the EasyScan . . . . .	71
5.1 Plot of the measured temperature of the coil . . . . .	73
5.2 Scanner amplitude measurement test setup . . . . .	73
5.3 Top: stationary beam reflected from the original scanner. Bottom: moving beam reflected from the original scanner at max amplitude . . . . .	74
5.4 Flexure 1 mounted without a washer amplitude, while operating at the resonance frequency . . . . .	75
5.5 Best recorded performance results of each flexure . . . . .	76
5.6 Saturated images of the scan line. The two upper scan lines are of acceptable quality. The bottom three scan lines are unacceptable and are a result of bad mounting . . . . .	77
5.7 Resonance frequency dependence on input signal with a corresponding amplitude . . . . .	78
5.8 Calibrated test images for green laser of the original scanner and the prototype . . . . .	79
5.9 Scanning amplitude comparison between the original and the prototype scanner. Both of scanners were driven by the OPMOD and the according amplitudes are referenced to the potentiometer value of the OPMOD. . . . .	80
5.10 Prototype and original scanner beam shapes with respect to potentiometer setting. . . . .	80
5.11 Scanned prototype test images with straight and warped beams . . . . .	81
6.1 Scanner part cost comparison . . . . .	83
A.1 Left: An arbitrary schematic of an electric circuit. Center: A magnetic circuit schematic analogous to the electric circuit on the left. Right: Configuration of magnetic circuit which corresponds to the magnetic circuit schematic. . . . .	87
A.2 Left: Magnetic circuit configuration with two loops. Right: Schematic of the magnetic circuit on the left. . . . .	87
A.3 Rectangular volume with stress tensor components highlighted . . . . .	89
B.1 Maximum operating settings of various piezo actuators of <i>Physik Instrumente</i> . . . . .	90
D.1 Inertia of a rectangular body about an axis $O$ . . . . .	93

# List of Tables

1.1	Requirements for the EasyScan scanner redesign . . . . .	5
1.2	HF scanner amplitude measurements . . . . .	7
1.3	General properties of piezo, voice coil, reluctance actuation methods . . . . .	10
2.1	Lenticular lens parameters . . . . .	14
2.2	Calibrated amplitude and image intensity of the tested optical elements . . . . .	16
3.1	Magnetic circuit parameters for comparison of actuators . . . . .	23
3.2	Rotational DOF flexure comparison . . . . .	27
4.1	Magnetic circuit numeric values assumed for comparison of different circuits . . . . .	28
4.2	Magnetic circuit configuration . . . . .	30
4.3	Computed output forces and torques of circuit configurations 1, 1+ and 4 with respect to the air gap size $t$ . . . . .	32
4.4	Magnetically soft materials . . . . .	33
4.5	Magnetic properties of common neodymium grades . . . . .	34
4.6	Available 44H grade magnets of relevant dimensions of <i>Supermagnete</i> . . . . .	35
4.7	Current density of various wire gauges . . . . .	39
4.8	Polynomial fit values for the flux linkage distribution . . . . .	41
4.9	Current density of various wire gauges . . . . .	41
4.10	Polynomial approximation of the actuation torque with respect to rotation and current . . . . .	42
4.11	Most suitable available flexure materials . . . . .	50
4.12	Maximum fatigue stress of stainless steel and titanium . . . . .	52
4.13	Design variable limits for the HF scanner flexure . . . . .	55
4.14	Flexure versions manufactured for testing . . . . .	59
4.15	Loads acting on the HF scanner magnet at a rotation of 0 mrad and at a current of 45.3 mA . . . . .	60
4.16	Design variable limits for the HF scanner flexure . . . . .	63
4.17	Design variable limits for the HF scanner flexure . . . . .	65
4.18	Error budget analysis for the HF scanner . . . . .	67
4.19	Technical data of adhesive <i>3M™ Scotch-Weld™ 2216</i> . . . . .	70
5.1	Tested HF flexure and ferromagnetic housing models . . . . .	72

# Abbreviations

3D - Three dimensional  
AC-DC - Analog to digital  
AWG - American wire gauge  
CAD - Computer aided design  
COTS - Commercial off the shelf  
DOF - Degree of freedom  
EDM - Electrical discharge machining  
EMF - Electromotive force  
Eur - Euro  
FACT - Freedom and Constraint Topology  
FWHM - Full width half maximum  
HF - High frequency  
LCOS - Liquid crystal on silicon  
LF - Low frequency  
MEMS - Microelectromechanical systems  
MMF - Magnetomotive force  
NRE - Non-recurring engineering  
P-P - Peak to peak  
RMS - Root mean square  
Op-amp - Operational amplifier  
OPMOD - Optical module  
Q factor - Quality factor  
SLM - Spatial light modulation  
S-N curve - Plot of cyclic stress S versus cycles N to failure

## Introduction

Retina is the most light-sensitive layer of the human eye, which transforms the image focused on the retina into electrical neural impulses which are sent to the brain to create visual perception. The condition of the retina can help diagnose various diseases and disorders such as: glaucoma, diabetic retinopathy, cataract, macular degeneration, retinal detachment, central serous retinopathy. Numerous retina imaging methods have been developed over the year [21]. In 2007 a Dutch company i-Optics developed the prototype of a scanning laser ophthalmology type retina scanner named the EasyScan. What makes the EasyScan a great product, is that it can take images of the retina through 1.5 mm diameter pupils, which means dilation of the pupil is no longer required, therefore not causing short term inconveniences for the users. Additionally, the room illumination where the EasyScan is situated does not affect its performance. The total weight of the EasyScan is less than 11 kg which makes it a very versatile device that can be used at any clinic or optician.

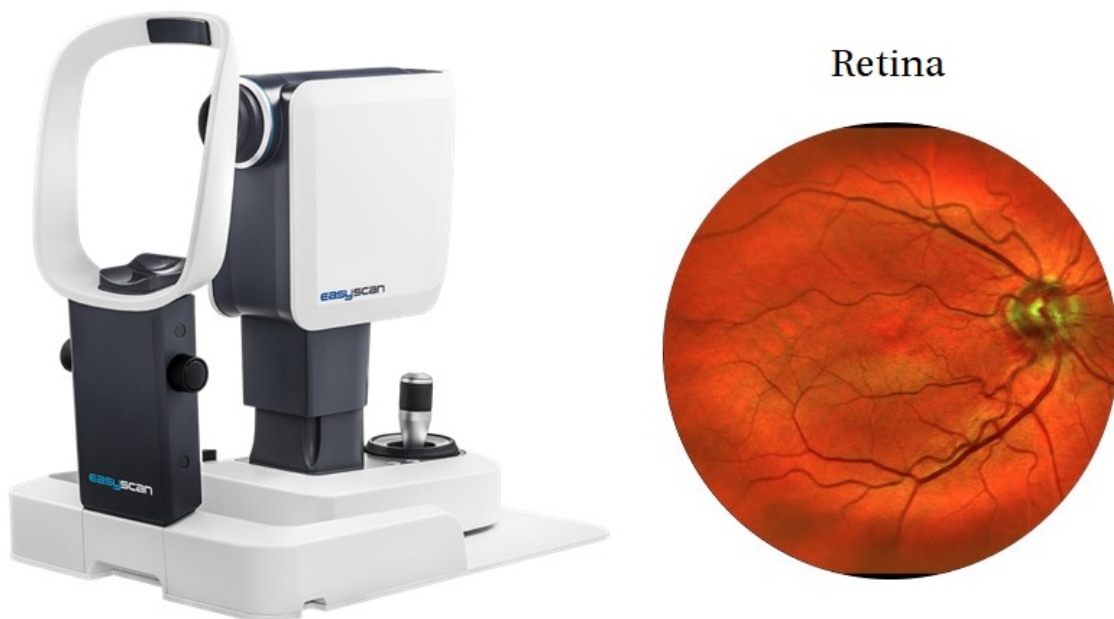


Figure 1.1: Left: the EasyScan. Right: Image of the retina scanned with the EasyScan

### 1.1. Working principle of the EasyScan

The main component of the EasyScan is the optical module - OPMOD. Figure 1.2 illustrates the schematic of the main optical components of the OPMOD. Two laser diode light sources are used in the system: a green laser with central wavelength of 520 nm and a red laser with a central wavelength of 785 nm, with a spectral width of 2 nm at FWHM. Different wavelengths of photons penetrate separate layers of the retina, which

allows to extract more information about the retina. The light from the lasers propagates up to the high frequency (HF) mirror which is oscillating at 4.65 kHz frequency at the range of  $\pm 3$  mrad. The reflected light then reaches the lenticular lens, which creates a Talbot pattern [22]. The light continues through the cylinder lens, reflects on the low frequency (LF) mirror and continues through the scan lens assembly. The combination of the cylinder lens and the scan lens focuses the light into a line. Due to the Talbot effect created by the lenticular lens the compressed line is not a continuous line, but a line of dots. The effects of light passing through the lenticular lens and the cylindrical lens are depicted in figure 1.3.

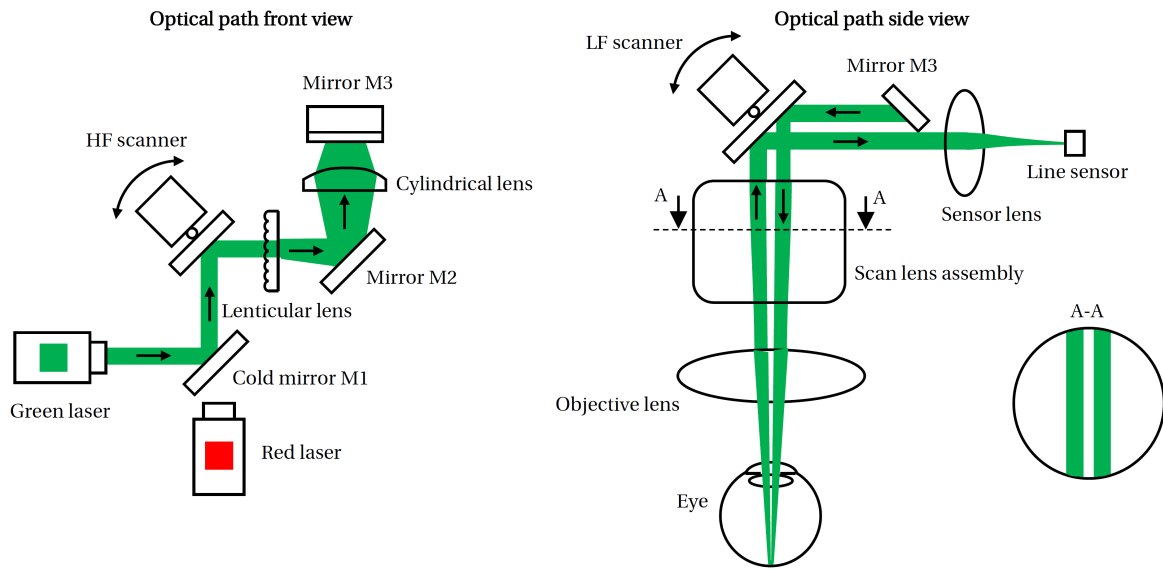


Figure 1.2: Schematic of main optical components of the EasyScan

The LF scanner is oscillating at a frequency of 9 Hz with a range of  $\pm 6.5^\circ$ . After exiting the scan lens assembly, the light passes through the objective lens and then is projected through the pupil of the eye on to the retina. The quasi-continuous line scatters on the retina and travels back to the LF scanner, which reflects the light towards the line sensor. The illumination is read out at 9.3 kHz, which is double the oscillation frequency of the HF scanner.

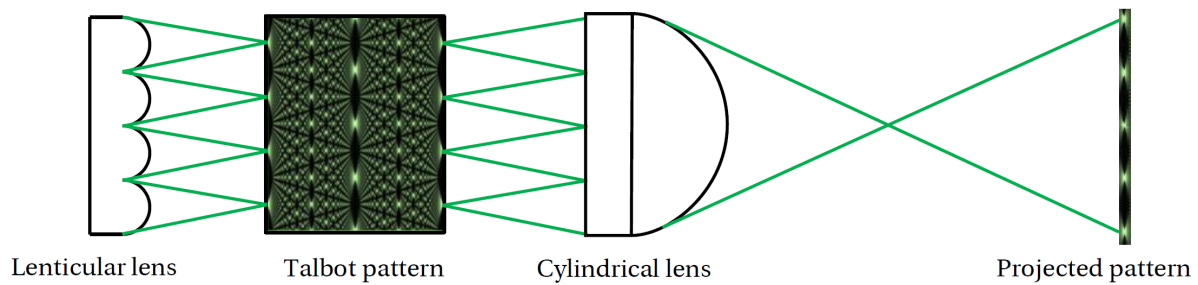


Figure 1.3: Light transmission from lenticular lens to the cylindrical lens and the projected Talbot Pattern.

The task of the LF scanner is to direct the quasi-continuous line vertically over the retina. The task of the HF scanner is to move the quasi-continuous line in the direction of the line, in order to achieve uniform illumination of the retina during the read out time of the line sensor. Figure 1.4 illustrates the scanned images of a flat test target when the HF mirror is both on and off. It is clearly visible that vertical lines are present when the HF scanner is off, therefore without the HF scanner the image intensity would not be uniform. The image uniformity evaluation is not based on quantitative measures, but on visual perception of the user. During the alignment procedure of the OPMOD, the operator regulates the amplitude of the HF scanner by manipulating a potentiometer which regulates the voltage of the scanner. The voltage of the scanner is increased until the high frequency vertical lines disappear. The disappearance of the vertical lines can happen at several



different potentiometer settings, however, of most interest is the setting of the lowest potentiometer values as it results in the smallest oscillation amplitude. The HF scanner is also a source of a high pitch "beep" tone, which increases with an increasing oscillation amplitude. This is an additional reason to keep the oscillation amplitude of the HF scanner low, as it reduces the noise.

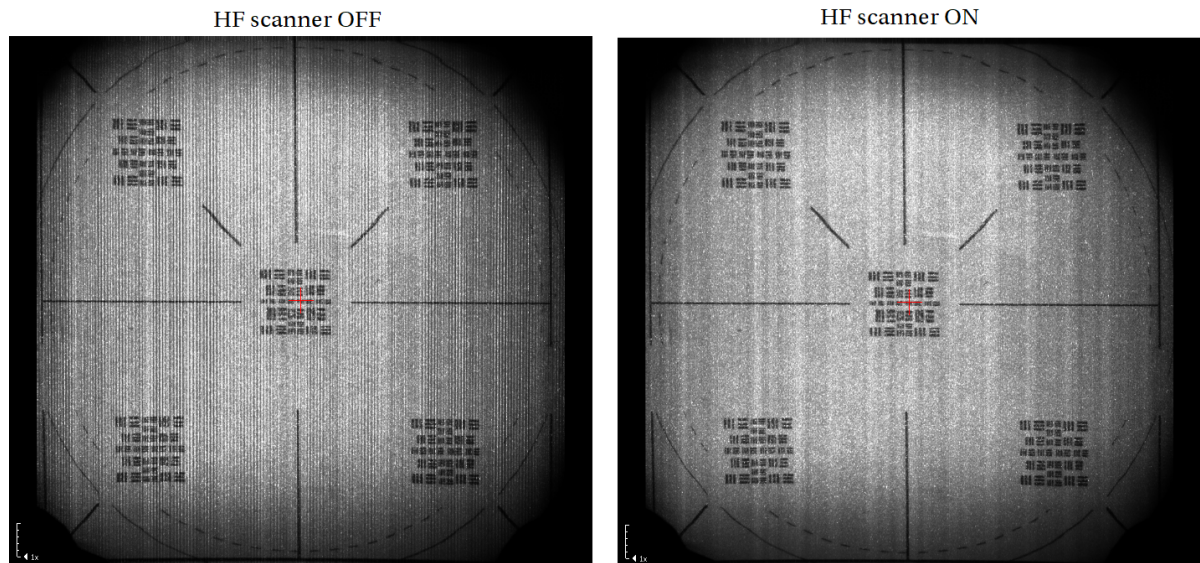


Figure 1.4: Image of flat test target used during the optical alignment procedure of the OPMOD. On the left is an image produced when the HF mirror off. On the right is an image produced when the HF mirror on. Image on the left has an unacceptable quality.

If the lenticular lens was not used in the optical system, then the cylindrical lens would generate a line for which there would be a correspondence between the position of the light entering and exiting the cylindrical lens, as explained by the EasyScan patent [10]. As a result, if a part of the incoming light beam was blocked, then this would lead to an area of low brightness in the line, which would end up as a dark line or curve in the final image that is created when an object is scanned. When an array of line generating ridges in close proximity is applied, the correspondence as mentioned is no longer present, as depicted in figure 1.5. This effect that the lenticular lens induces is critical when scanning eyes that have cataract, as then the local clouding of the lens does not significantly reduce the illumination of a specific area on the retina.

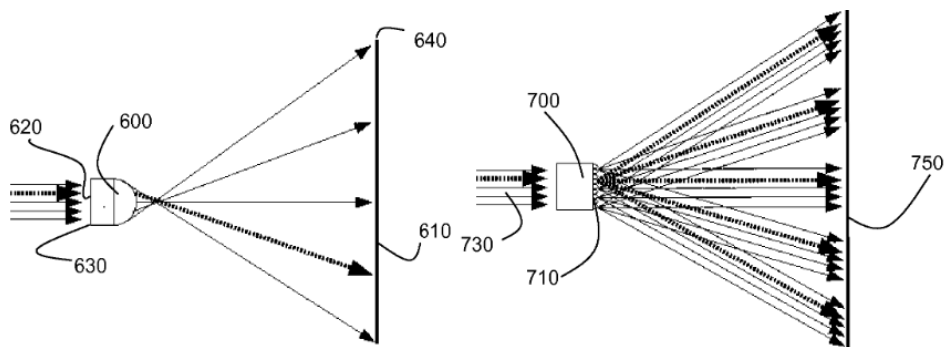


Figure 1.5: Spatial beam relation comparison between a convex lens and a lenticular lens. From patent *NL2005253C2* by Michiel Herman Mensink and Julien Coyne, 2010, World Intellectual Property Organization

## 1.2. Problem statement

The currently used LF and HF scanners will become obsolete in the foreseeable future. To ensure EasyScan's continuity in the market the scanners have to be replaced. To correctly approach the problem of scanner obsolescence the function of each scanner has to be defined:

- LF scanner - moves the quasi-continuous scan line vertically over the retina.

- HF scanner - makes the intensity of quasi-continuous line uniform during the readout time of the line sensor.

The LF scanner function is such that only a different scanning device can be used to fulfil its function. However, the function of the HF scanner is such that other techniques apart from directly moving the scan line could be used to make its intensity on the retina uniform. The proposed project for solving the issue of scanner obsolescence is discussed in section 1.10.

### 1.3. System requirements

Both the operational requirements for each scanner, and the general system level requirements are depicted in table 1.1. The requirements stated in the table are generalized, a deeper look into specific requirements is discussed in sections 1.4, 1.5, 1.6, 1.7, 1.8. Figure 1.6 illustrates the current scanners used in the EasyScan. These scanner mirrors were designed to be used for barcode scanners, however they are becoming obsolete, as suppliers are discontinuing their production. Both the LF and HF scanners have the same structure, but are tuned to work at different frequencies and with different input waveforms.

Table 1.1: Requirements for the EasyScan scanner redesign

Scanner	Operational requirements				
	Frequency [Hz]	Amplitude [mrad]	Scan motion	Mirror size [mm]	Available space [mm]
LF	9 Hz	$\pm 130,5$	Triangular or sawtooth	8 x 4 mm	24,5 x 26,1 x 45.9 mm
HF	4650 Hz	$\pm 3$	Any that makes the scan line uniform	7 x 6 mm	22 x 29,7 x 36 mm
System requirements					
Price	The total price for HF and LF scanners is 300 Euro/EasyScan				
Power	Desired: to be compatible with current electronics which is capable of 5 V, 40 mA for the HF scanner, and $\pm 2.5$ V and 250 mA for the LF scanner. Required: power may be altered if needed, but it has to result with changes to electronics which are feasible. Chapter 1.4 explains currently used electronics in more detail.				
Temperature	Operational: 15-30 °C. Transportation: less than 55 °C.				
Lifetime	50 minutes/day for 5 days/week for 5 years.				
Shock load	25 G's				

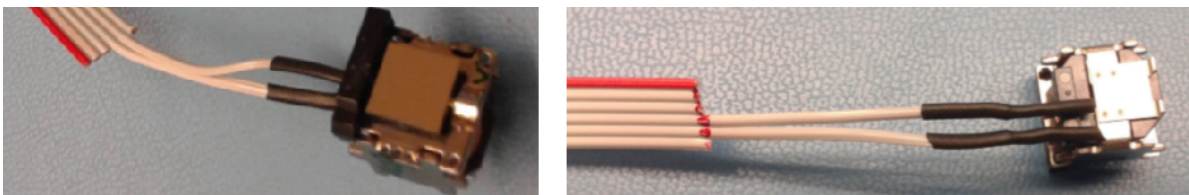


Figure 1.6: Scanners currently used in the EasyScan

A quantity that is useful for the design of the scanners is the distance which is traversed by the edge of the mirror during the forward scan - it is defined as the actuation stroke. Figure 1.7 shows the actuation stroke and clarifies how the mirrors of the scanners should be oriented with respect to the axis of rotation.

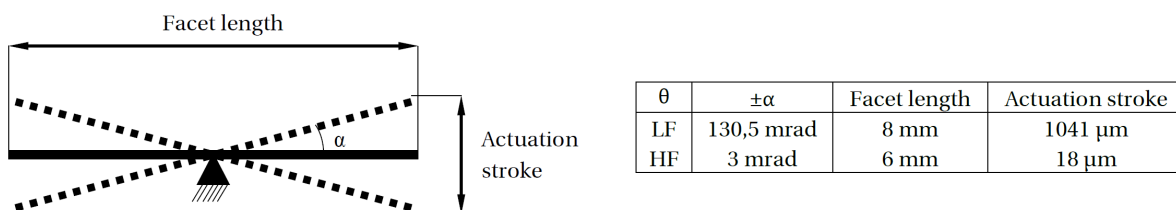


Figure 1.7: Schematic showcasing parameters important for design

## 1.4. Driving electronics

Both of the LF and HF scanners are operated in open-loop, and there are no sensors integrated to measure the rotation or velocity of the scanners. The HF scanner is driven by the microcontroller ATMEGA88PA-MU. The scanner is connected to the microcontroller as displayed in figure 1.8. The output pin of ATMEGA88PA-PU can be set either to 5 V or to ground (0 V). By periodically switching the output pins from ground to 5 V a square wave signal of 10 V P-P is created.

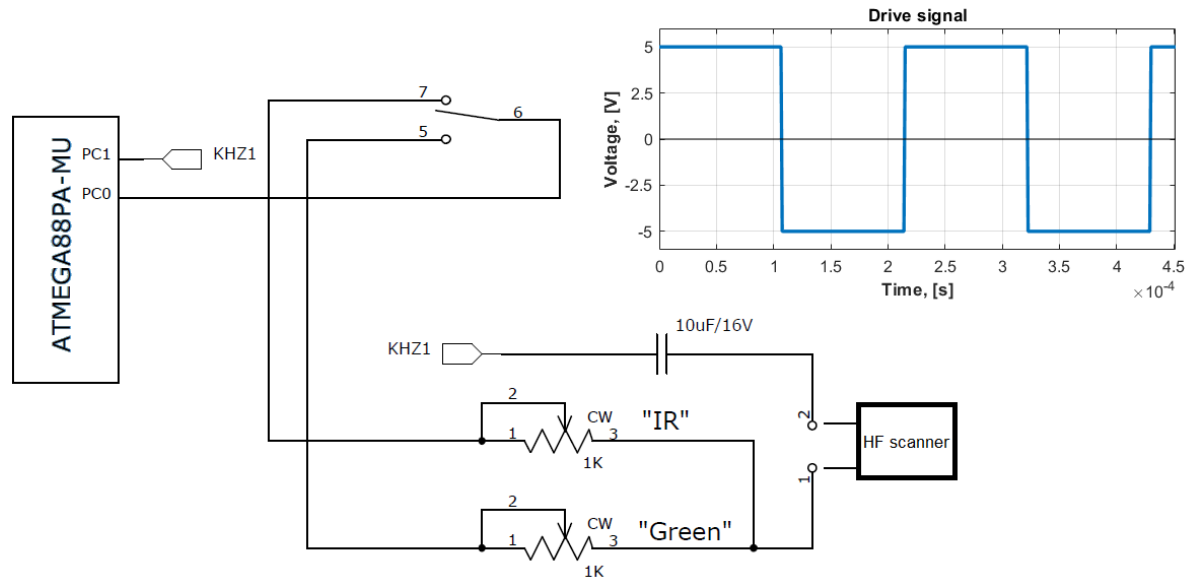


Figure 1.8: Driving electronics of the HF scanner

The LF scanner is driven by  $\pm 2.5\text{V}$  12 bit signal. The 5V 12 bit signal is created by the microcontroller ADuC841, which is then fed to an op-amp AD8532. The op-amp is set up in a voltage follower configuration and the input signal is referenced to 2.5 V. By referencing the input signal, the current running through the LF scanner the direction of the current can be controlled, allowing bi directional actuation. The schematic of the LF scanner electronics is displayed in figure 1.9

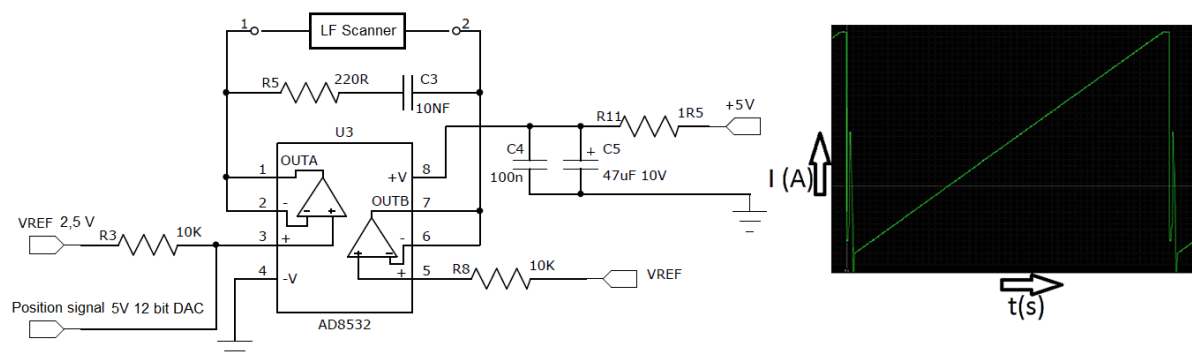


Figure 1.9: Driving electronics of the LF scanner

The EasyScan is powered by a 60 W 12 V AC-DC adapter. Ideally, the new scanners must be able to run from the available electronics. If additional electronics are required, they must be economically feasible and fit into the EasyScan. Free space for additional electronics is only 20 x 70 x 70 mm.

## 1.5. Mirror dimensions

The size requirements for mirrors, stated in table 1.1 are real mirror dimensions. For reference, the clear aperture requirement is 1 mm smaller than the real mirror dimensions. The mirror thickness does not have a

strict requirement, but as it will explained in chapter 3.2, the scanner needs to have as low inertia as possible, therefore, the thickness needs to be minimum. The supplier of the required mirrors is able to supply these mirrors at a 0.6 mm thickness, which is still stiff enough, not requiring specific handling tools.

## 1.6. Amplitude requirement

The amplitude requirement of the LF scanner is the total operating range that the scanner needs to operate. The actual scan angle during operation is  $\pm 113.2$  mrad. The additional  $\pm 17.3$  mrad of range is used for offsetting the scan angle. The offset is used to align the scanner during calibration.

The amplitude requirement of the HF scanner is derived from practical experiments because conflicting documentation on the HF scanner indicated different values. Evaluation of the required amplitude was set up during the production in order to measure values that are calibrated for commercial products. Only the amplitude values of four EasyScans were measured. The results are depicted in table 1.2.

OPMOD	$\pm$ Amplitude, [mrad]	Calibration setting
1	1,32	Red
	1,41	Green
	2,37	Max
2	0,67	Red
	0,87	Green
	2,65	Max
3	0,88	Red
	0,69	Green
	3,15	Max
4	0,87	Red
	0,38	Green
	2,02	Max

Table 1.2: HF scanner amplitude measurements

The results show that the calibrated amplitude values vary for each EasyScan and with each light source. The coefficients of variance of the data for the calibration of red, green and maximum amplitude are 29 %, 52 %, 19 % each. Therefore deriving the required amplitude values statistically would not be sound. An obvious observation is that the required amplitude should be larger or equal than the highest value calibrated for a specific wavelength, that has ever been recorded. The largest value measured was for the green light source image of the 1st measured OPMOD which is  $\pm 1.41$  mrad. The required amplitude is selected as 3 mrad which gives a margin of safety of 2.13 for the largest calibrated amplitude ever recorded and is only 5 % lower than the maximum amplitude value ever recorded for an in production HF scanner.

## 1.7. Available space

The available space for the HF and LF scanners is showcased in figure 1.10. The displayed dimensions are derived by removing the current scanners. To increase the available space, theoretically it is possible to remove additional material from the housing structure. For example, the housing structure on the right upper side of the LF scanner can be removed, because it does not serve any purpose. However, opportunities to increase space for the HF scanner are more limited, because the space HF scanner is in close proximity to the lenticular lens and the cold mirror M1.

Additionally, the HF scanner rotation and translation is aligned during the assembly procedure. The alignment directions are illustrated in figure 1.10. The LF scanner does not have alignment mechanisms and is glued into place during the optical alignment procedure.

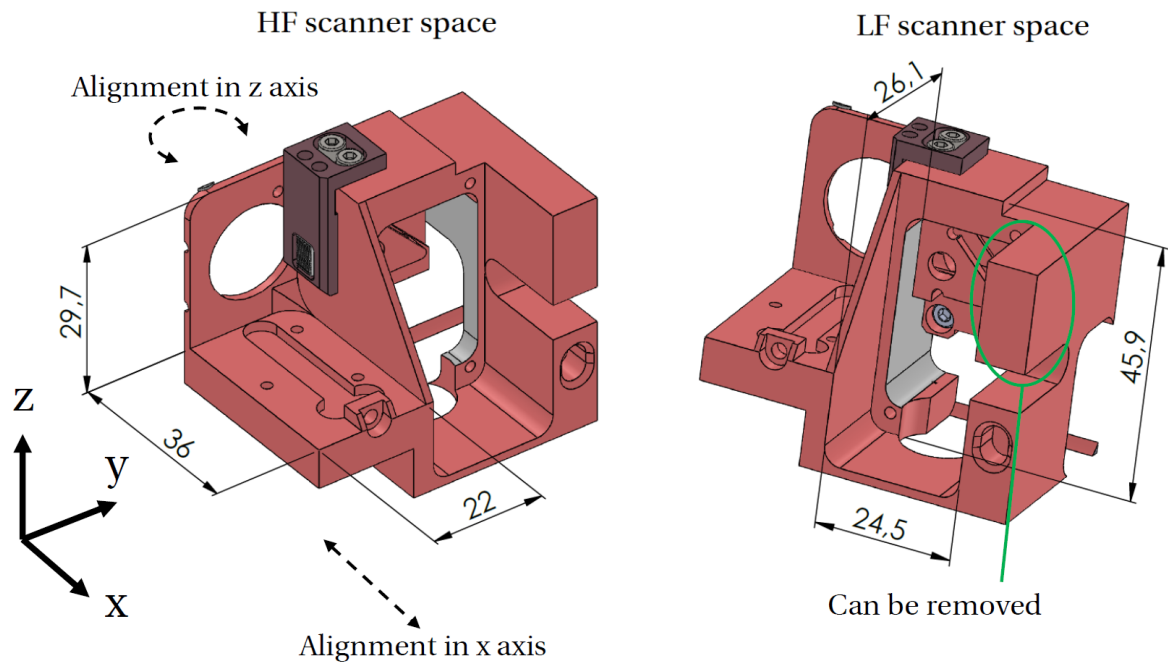


Figure 1.10: Available scanner space for the HF and LF scanner

### 1.8. LF scanner trajectory

The requirements state that the LF scan frequency is 9Hz with a total P-P amplitude of 226.4 mrad. This means that the total motion time for one cycle is  $t_t = 111.1$  ms. The scan motion currently utilized is sawtooth. The produced scan image by the EasyScan has a height of 1024 pixels. However, 64 pixels are redundant as their are used for the back scan. This means that currently  $t_f = 104.2$ ms are used for scanning the image with constant speed and only  $t_b = 6.9$ ms are used for returning to the initial position and reaching the constant scan speed. This results in a duty cycle of 93.8 % and a constant scan speed of  $\omega_s = 2.17$  rad/s. The theoretical LF scanner trajectory is visualised in figure 1.11.

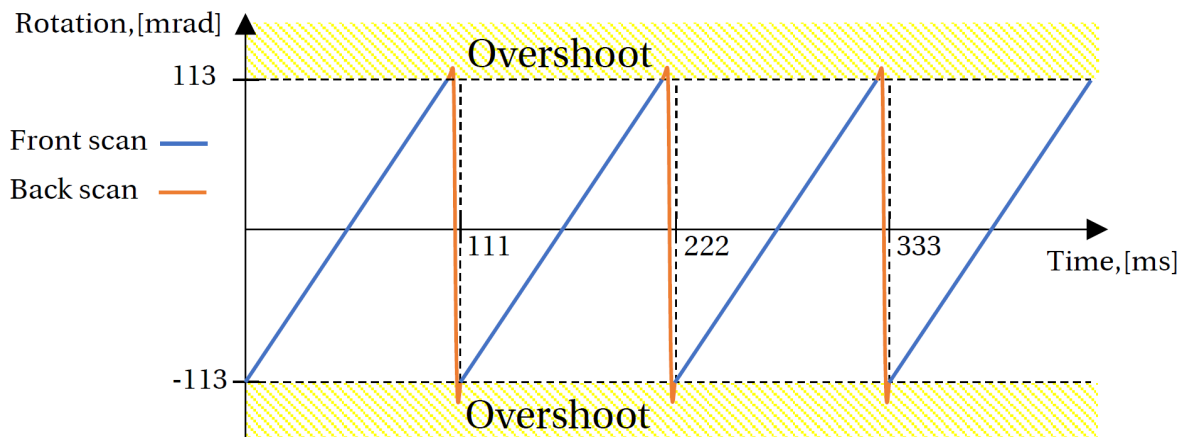


Figure 1.11: Motion trajectory of the LF scanner

### 1.9. Literature survey results

As stated in section 1.2 the HF and LF scanners have different functions; therefore, the approach for replacing each scanner is different. The conducted literature survey was focused in two areas: scanning technologies and intensity uniformity techniques. The results of both areas will be briefly discussed in the following sections.

### 1.9.1. Scanning technologies

Contemporary scanning technologies were evaluated with respect to the requirements of the HF and LF scanners. A concentrated summary of the scanning technologies is displayed in figure 1.12.



Property	Model	Requirement	Galvanometer	Resonant/ Electromagnetic	MEMS	Polygon	Piezo	Acousto optical	Electro optical	Risley prism
Frequency	LF	9 Hz	+	+	+	-	+	+	+	+
	HF	4650 Hz	-	+	+	+	+	+	+	-
Amplitude	LF	±113 mrad	+	+	+	-	-	-	-	+
	HF	±3 mrad	+	+	+	+	+	+	-	-
Aperture	LF	8 x 4 mm	+	+	-	+	+	+	-	+
	HF	6 x 7 mm	+	+	-	+	+	+	-	+
Waveform	LF		+	+	+	-	+	+	+	-
	HF		+	+	+	-	+	+	+	+
Price	HF+LF	300 Eur per Easyscan	-	±	-	-	-	-	-	-

Figure 1.12: Summary of contemporary scanning technologies with respect to the operational requirements of the HF and LF scanners

Almost all of contemporary scanning technologies have an unfeasible price when compared to the 300 Euro requirement for a single Easyscan. The only financially feasible technology is the resonant - electromagnetic type of scanners, the same type that is used currently in the EasyScan. However, the currently used scanners that originally were developed for barcode scanning applications, are being discontinued in production, therefore this specific model will be unobtainable. If the price requirement was relaxed, then galvanometer type of scanners would be the most feasible technology. Galvanometers are well suited for the scan parameters of LF scanner and usually have integrated feedback systems. However, at high frequency they can require an unfeasible amount of power and additional cooling. The piezo type scanners have a limited amplitude, therefore, are inherently only suitable for the HF scanner. Similarly to the galvanometer, at high frequency the piezo scanners can require large amounts of power and additional cooling. MEMS scanners are unfeasible due to smaller apertures than required for the HF and LF scanners. Some MEMS devices can have apertures the same size as required for the HF and LF scanners by bonding a mirror on the micro machined structure, however, then the operational frequencies and rotation amplitudes reduce below the required for the LF and HF scanners. Polygon type of scanners are not suitable as a replacement because of the small scan angle requirement with respect to what polygon scanners are suited for. The acousto-optical scanners have lower scan beam amplitude than required for the LF scanner, but fulfil the rest of the requirement, except price. The electro optical scanners cannot produce the required amplitude both for the LF and HF scanners. Risley prism scanners cannot operate at the frequency required for HF scanner. As a LF scanner, the Risley prism scanner is limited by the scan waveforms that it can produce, therefore making it unfeasible.

Commercial scanning technologies are too expensive, therefore, a custom scanner has to be designed. This is a challenging task, because custom solutions are usually more expensive than devices that are mass produced. The EasyScan sells between 200 and 400 EasyScan units per year, therefore, this amounts to small series production. To make a custom design feasible, all of the scanner components have to be cheap, and the design needs to be simple enough to have a short assembly time. A determinant whether it is feasible to design a custom scanner is the actuation method. While the guiding mechanism of the scanner may be the same, the actuation methods can differ. The literature study indicated that there are three potentially feasible actuation methods: voice coil, reluctance and piezo. General properties of these actuation methods are listed in table 1.3. All of the mentioned actuation methods can be used to design a HF scanner. A LF scanner can only be designed with the voice coil and reluctance actuation methods, as piezo has an actuation range several magnitudes smaller than required.

Piezo	Voice coil	Reluctance
<ul style="list-style-type: none"> <li>• Output is displacement</li> <li>• Stroke <math>\approx 1\mu\text{m}/1\text{mm}</math> of material</li> <li>• Can be difficult to drive at high frequency</li> <li>• COTS</li> </ul>	<ul style="list-style-type: none"> <li>• Linear force/current ratio</li> <li>• Output force is almost independent from position</li> <li>• Guiding for mover needs to be provided</li> <li>• COTS</li> </ul>	<ul style="list-style-type: none"> <li>• High force/current ratio</li> <li>• Output force dependant on position</li> <li>• Guiding for mover needs to be provided</li> <li>• No COTS. Magnet, coil, yoke are configured individually</li> </ul>

Table 1.3: General properties of piezo, voice coil, reluctance actuation methods

### 1.9.2. Intensity uniformity techniques

Intensity uniformity techniques discussed in the literature survey are summarized in figure 1.13. Linear diffrusers, spatial light modulation by use of a DOA and smaller pitch lenticular lenses indicated the most potential in reducing the HF scanner amplitude or making the scanner redundant.

Techniques	Rationale	Pitfalls	Implementation
Spatial light modulation	Structuring light by use of diffraction to achieve uniform intensity. Due to diffraction the illumination of the retina is not influenced by cataracts.	DMD, LCOS modulators expensive or unfeasible to implement. A DOE is limited to specific wavelengths and the outputted line is still made of dots.	Possible with a DOE
Linear diffuser	Structuring light by use of diffraction to achieve uniform intensity. Unlike spatial light modulation the diffuser surface is a pseudo-random, non-periodic structure.	Instead of a determined interference pattern a speckle pattern is created.	Possible
Wide band light source	Reducing the coherence of the light source to reduce intensity variation of the interference pattern.	Light sources either output not enough power, have too high beam divergence or are not available for a certain wavelength.	No
Smaller pitch lenticular lens	Making the interference pattern fine, thus requiring less amplitude of the HF scanner.	Some smaller pitch lenses have higher divergence which results in reduced illumination	Possible
Moving the lenticular lens	Gives the same effect as an oscillating HF scanner. Translating mechanism may be simpler than a rotating mechanism.	The required linear amplitude is higher than the linear amplitude that would be required to rotate the mirror to achieve the same amount of beam displacement.	No

Figure 1.13: Summary of intensity uniformity techniques discussed in the literature survey

## 1.10. Project proposal

The literature survey resulted in two conclusions:

- To achieve the set price requirement a custom scanner design has to be made by utilizing either piezo, voice coil or reluctance actuation methods.
- The amplitude of the HF scanner can be reduced or the scanner can be made redundant with intensity uniformity techniques.

Therefore, a project is proposed, which follows these steps:

1. The intensity uniformity techniques are tested out to see, whether the amplitude of the HF scanner can be reduced. Testing of the intensity uniformity techniques is done directly on the optical module of the EasyScan.
2. Based on results the requirements of the HF scanner amplitude are confirmed.
3. Selection of an optimal actuation and guiding method for the scanners.
4. Detailed scanner design.

5. Building a prototype and validating its performance. Performance is validated in two phases. During the first phase, the scanners amplitude at the operational frequency is measured. During the second phase, the scanners are tested directly on the OPMOD of the EasyScan.

The expected result of this project are designs of HF and LF scanners that fulfil the operational requirements of the current scanners, and are economically feasible.



# 2

## Intensity uniformity techniques

Optical components for each of the possible solution proposed in section 1.9.2 were acquired. The testing of each optical component is done by mounting it directly in the OPMOD and replacing the original lenticular lens. The performance of each element is evaluated by taking test target images as showcased in figure 1.4. The required amplitude is evaluated by taking the potentiometer setting value and comparing it to the setting of the original lenticular lens. Additionally, image intensity values are recorded and compared. The tested optical elements are showcased in figure 2.1.



Figure 2.1: Tested optical elements

### 2.1. Linear diffuser

Diffusers are optical components, which can spread incoming light into a specific spatial form. The shape and intensity of the output light distribution on the image plane is dependant upon the diffuser parameters, and the wavefront of the incoming light. Linear or otherwise called elliptical diffusers can shape the light in two direction in such a way, that the output light in the image plane can take the shape of a line. For example the linear diffuser ED1-L4100 of *Thorlabs* has a diffusion angle of  $0.4^\circ \times 100^\circ$  [9].

Linear diffuser is functionally similar to the lenticular lens, as it also creates many virtual point sources which, are necessary to have light enter the eye at different positions and angles, as explained in chapter 1.1. The linear diffuser would do the same function, but instead of a finite number of virtual point sources, it would create an arbitrarily infinite point source number. Therefore, the Talbot pattern phenomena would not take place. Due to the random surface fluctuations of the diffuser, a speckle pattern would form. Due to speckle, the scan line would not have uniform intensity and therefore, the HF scanner would still be needed. Whether a smaller amplitude of the HF scanner would be required is determined experimentally.

Another concern of using a linear diffuser would be, that it adds additional diffusion in the perpendicular direction to the line generated by the cylindrical lens. This diffusion is undesirable and could result in loss of light in the scanned imaged, because the light would not be focused enough.

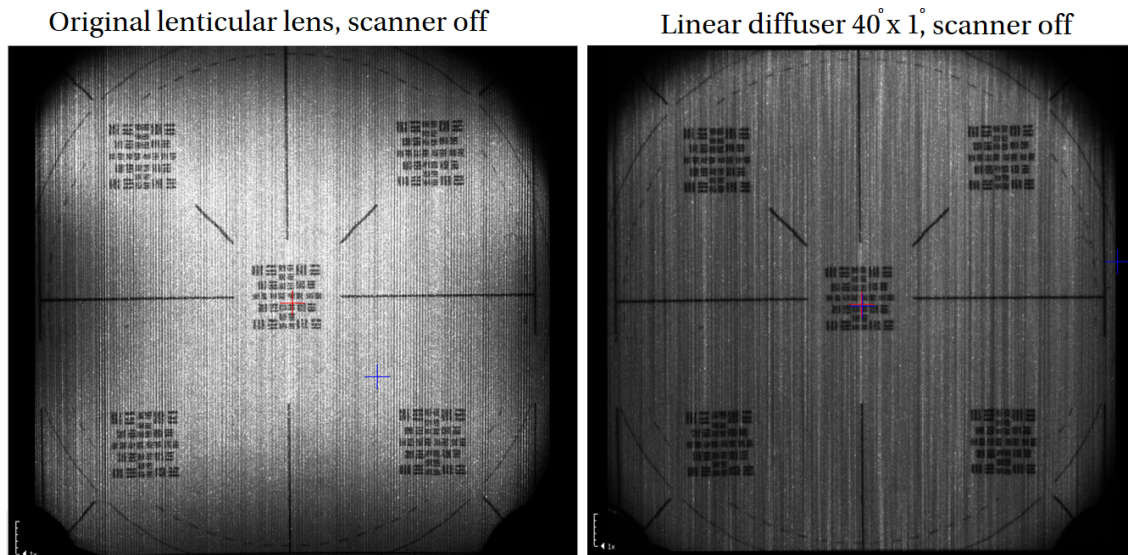


Figure 2.2: Scanned test image comparison between the lenticular lens and the linear diffuser.

### 2.1.1. Experiments

Experiments with linear diffusers of  $40^\circ \times 1^\circ$  and  $60^\circ \times 1^\circ$  divergence angles resulted in speckle patterns, which required approximately double the HF amplitude than with the lenticular lens to make the scan line, uniform. Additionally, due to the divergence in the perpendicular direction to the line the optical system was not able to focus the light well enough, which lead to about 80% decrease in light intensity. The difference in illumination can be clearly seen in figure 2.2. Linear diffusers that have smaller angle of divergence in the perpendicular to the line direction exist, however, the main objective of reducing the HF scanner amplitude would still not be achieved. This means, that a diffuser cannot be used instead of the lenticular lens.

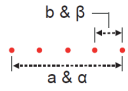
## 2.2. Diffractive optical elements

Diffractive optical elements are objects, that are capable of phase modulation of the incoming wavefront. The phase distribution is already fabricated on the optical element, which means, that a single element can produce a single pattern. Various DOE's are available in the market, however, of most interest are elements capable of producing a line. Such an element could be used instead of the lenticular lens, to create the effect of light coming in the eye at various angles of incidence, as depicted in figure 1.5.

### 2.2.1. Experiments

The DOE elements tested in the EasyScan are listed in figure 2.3. The technical data indicates, that the DOE's are limited to a wavelength range of about 100 nm. Exceeding the wavelength range, results in decreased efficiency of the DOE.

An image of the best quality was produced with the 383 model DOE and is depicted in figure 2.4. All of the DOE images produce low frequency vertical lines of high intensity, which is unacceptable. Interestingly, the scanned image produced with the DOE has a 17% higher image intensity than with the original lenticular lens, but this improvement in efficiency is not useful when the DOE cannot produce uniform intensity images.



DOE Item #	Description	Design Wavelength	Pattern Size @ 100 mm Distance, Values: mm			Pattern Angles (@ Design Wavelength)			Optimum Wavelength Range(s)
			a	b	d	$\alpha$	$\beta$	$\delta$	
DE-R 267	QC -Line – 30@532	532nm	53.8	--	--	30.1	--	--	● 470-560 nm
DE-R 283	QC - Line – 20@633	633nm	35.2	--	--	20.0	--	--	● 630-670 nm
DE-R 286	QC - Line – 30@660	660nm	54.6	--	--	30.5	--	--	● 600-700 nm
DE-R 369	QC - Line – 36@640	639nm	65.0	--	--	36.0	--	--	● 600-700 nm
DE-R 383	QC - Line – 51@840	840nm	95.0	--	--	50.6	--	--	● 790-880 nm

Figure 2.3: List of tested DOE models manufactured by *Holoeye*

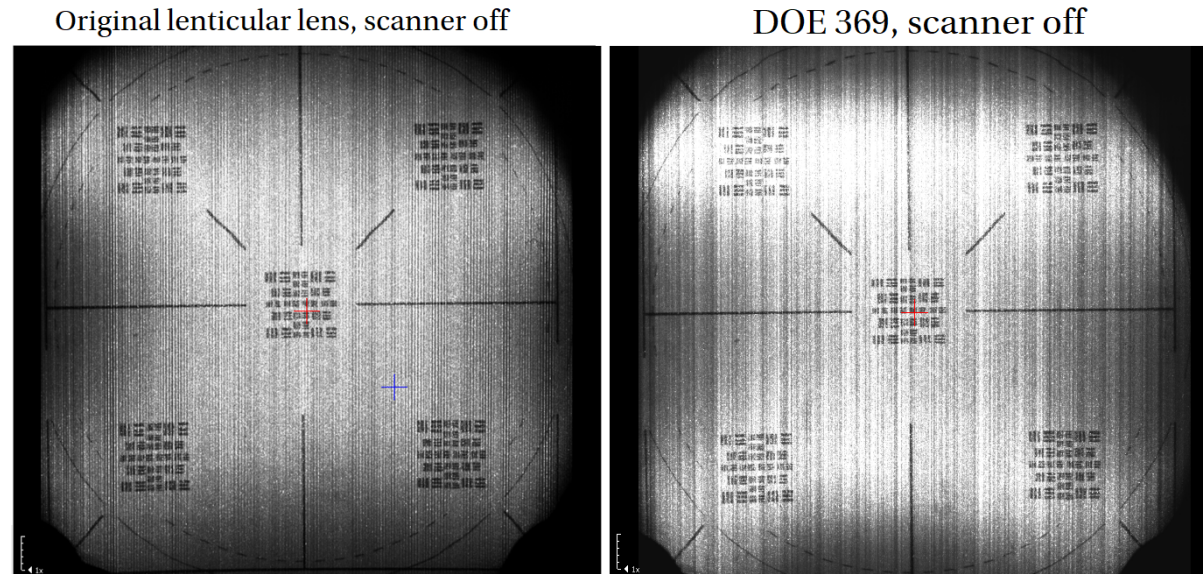


Figure 2.4: Scanned test image comparison between the lenticular lens and the DOE.

### 2.3. Lenticular lens

The currently used lenticular lens produces a Talbot pattern which is imaged onto the retina. The specific pattern imaged on the retina depends on the lenticular lens position in the system and the geometrical parameters of the lenticular lens. The distance at which the Talbot pattern repeats itself is calculated as:

$$z_T = \frac{2a^2}{\lambda} \quad (2.1)$$

where

$z_T$  = Talbot distance [m]

$a$  = period of the diffraction grating [m]

$\lambda$  = wavelength of the light incident on the grating [m]

Lenticular lens parameters					
Pitch [mm]	Radius [mm]	Divergence angle red beam [deg]	Divergence angle green beam [deg]	Talbot length red beam [mm]	Talbot length green beam [mm]
0.02	0.015	35.84	36.46	1.02	1.54
0.04	0.03	35.84	36.46	4.08	6.15
0.2	1.5	3.70	3.77	101.91	153.85
0.3*	0.5*	16.56	16.86	229.3	346.15

\*Currently used lens

Table 2.1: Lenticular lens parameters

Investigating available lenticular lens geometry leads to interesting results, which are depicted in table 2.1. The current lenticular lens has a pitch of 0.3 mm and generates a Talbot pattern with a length of 346.15 mm for the green light, which is relatively large when compared with a lens that has a 0.02 mm pitch and 1.54 mm Talbot length. With such short Talbot length an option arises to adjust the lens position during EasyScan alignment procedure for a more optimal pattern, as the Talbot length and the adjusting distance would be of the same order (viable position adjustment range is roughly 2 mm). Also with a smaller lens pitch, the initial number of "point sources" at the lenticular lens increases, for example, the number of spots at the lenticular lens would increase 15 times, if the lens that has a 0.02 mm pitch is used instead of the current one. With an increased number of spots on the line sensor the HF amplitude requirement could be reduced, or the HF

mirror would become redundant all together.

A drawback of a smaller pitch lenticular lenses is that they usually have a larger divergence angle. The current system is configured to accept the beam divergence angle of the current lens which is 20° smaller than the off the lens with pitch 0.02 mm,. This would mean that the beam of the finer lens would be cut off at the aperture in the system resulting in reduced illumination efficiency.

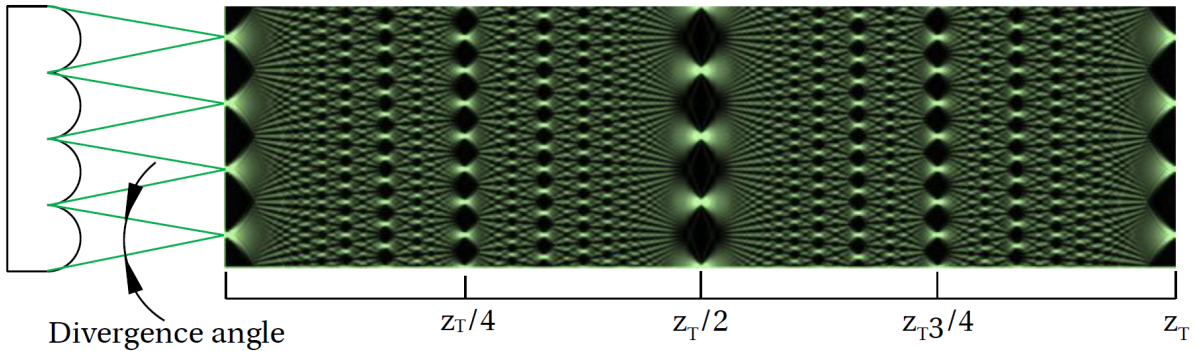
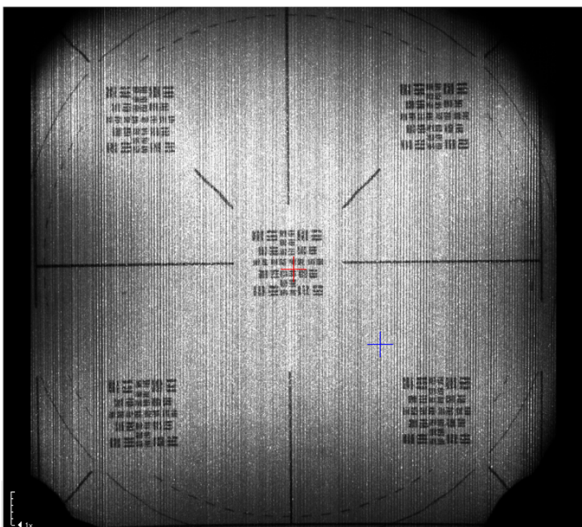


Figure 2.5: Left: Parameter table of lenticular lenses available from the current supplier. Right: Image of Talbot pattern with the half length and quarter length specified

### 2.3.1. Experiments

Experiments were conducted with lenticular lenses with pitches of: 0.02 mm, 0.04 mm, 0.2 mm. The results for lenses with pitches of 0.04 mm, 0.2 mm resulted in visually not improved images. The 0.02 mm pitch lens resulted in images visually very similar to the original, with respect to vertical stripe frequency. The compared images are showcased figure 2.6. The image with the fine pitch lens has worse illumination due to the increased divergence of the beam.

Original lenticular lens, scanner off



Finer lens, pitch 0,02 mm, scanner off

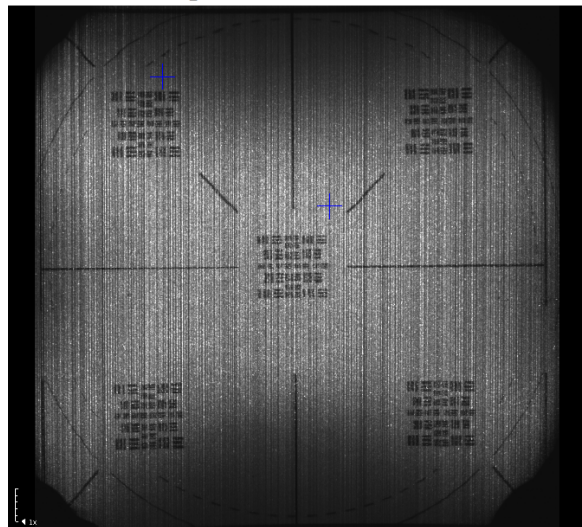


Figure 2.6: Scanned test image comparison between the original lenticular lens (pitch 0,3 mm) and the finest pitch lenticular lens (pitch 0,02 mm)

It is difficult to visually spot a difference between the scanned images, therefore, frequency analysis is used. The Fourier transform of each row of the image is calculated and then the results of all the rows is averaged. The frequency content of the images is displayed in figure 2.7. Due too different illumination of both images the intensity peaks of the original lens are higher, which makes the comparison difficult. However, it would seem that the two most notable intensity peaks of the fine lenticular lens are shifted to the higher frequency region, when compared to the peaks of the original lens. This would indicate, that the frequency

of the vertical lines is increased with the fine pitch lenticular lens. However, the scanning amplitude required to minimize the vertical lines did not decrease.

Moving the finest pitch lenticular to improve the projected line pattern did not yield any significant results. The lens was moved for a distance of 1 mm at a 0.05 mm increments. This range theoretically included all the Talbot pattern distributions for the particular lens, but no improvement in pattern was detected. As the projected Talbot pattern quality cannot be improved, this would conclude that a finer pitch lenticular lens would not reduce the requirements for the HF scanner amplitude and therefore, should not be implemented.

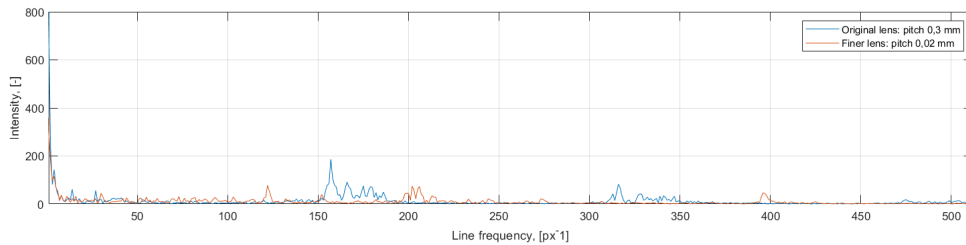


Figure 2.7: Frequency content of a test image scanned with the original lenticular lens (pitch 0,3 mm) and with the finest pith lenticular lens (pith 0,02 mm)

## 2.4. Conclusion on optical solutions

The summarized results of intensity uniformity techniques are displayed in table 2.2. The results indicate that all of the optical lenses did not manage to even achieve the same amount of scanner amplitude that is currently achieved with the original lenticular lens. Most of the recorded amplitude values are two times larger then the original scanner. Additionally, some of the optical elements induce image intensity loss. This is especially noticeable for the diffusers with intensity drop of around 8-9 times. Since the amplitude is not reduced with each of the optical elements, the image intensity losses do not matter, as the lenses are not a feasible solution.

Because all of the proposed methods of improving the optical system to reduce requirements for the HF scanner failed, the scanners need to be designed with the operational requirements stated in chapter 1.3.

Optical element	Potentiometer setting for green	Image intensity mean pixel value
Original lent. lens	Green 33 %	1869
Diffuser 40°x1°	Green 66 %	203
Diffuser 60°x1°	Green 66 %	220
Lent. lens 0.02 mm	Green 66 %	1192
Lent. lens 0.04 mm	Green 66 %	1162
Lent. lens 0.2 mm	Green 83 %	2072
DOE 267	Image quality unacceptable	1522
DOE 283	Image quality unacceptable	2214
DOE 286	Image quality unacceptable	1435
DOE 369	Image quality unacceptable	1730
DOE 383	Image quality unacceptable	2198

Table 2.2: Calibrated amplitude and image intensity of the tested optical elements

# 3

## System level scanner design

### 3.1. System level design outline

The function of both the HF and LF scanners is to rotate the mirror to change the direction of the reflected beam. Therefore, two main focus areas of design are identified:

- Actuating the mirror, so that it moves with a desired trajectory.
- Guiding of the mirror to create a rotational motion.

Both of the areas are different in their design methodologies and physics that are involved in the respective phenomena, but both must be synergized to create an optimal design. As a first step, an overview of both areas is conducted, in order to identify design options. Then, a final concept for the scanner is chosen.

### 3.2. Desired mechanical properties of the scanner

To simplify the design process, some basic design parameters must be defined. A configuration of a rotational 1 DOF mechanism is illustrated in figure 3.1. The maximum static and dynamic rotation under static and dynamic (sinusoidal) loads are defined as:

$$\theta_{st} = \frac{T}{(2\pi f_0)^2 I_{sc}} \quad \theta_{dyn} = \frac{T}{4\pi^2 I_{sc} \sqrt{(4f f_0 \zeta)^2 + (f_0^2 - f^2)^2}} \quad (3.1)$$

where

$\theta_{st}$  = flexure rotation under a static load [m]

$\theta_{dyn}$  = maximum flexure rotation under a dynamic sinusoidal load [m]

$T$  = torque [Nm]

$I_{sc}$  = scanner moment of inertia [ $\text{kg} \cdot \text{m}^2$ ]

$f_0$  = natural frequency of the scanner [Hz]

$f$  = frequency of the exiting torque [Hz]

$\zeta$  = damping ratio [-]

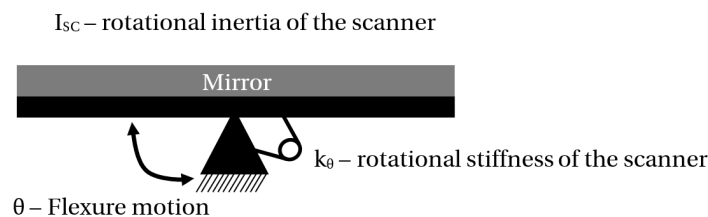


Figure 3.1: Sketch of a 1 DOF scanner configuration

Equations 3.1 indicate that the displacement of the scanner is proportional to the actuating torque  $T$ , but inversely proportional to inertia  $I_{sc}$  and natural frequency  $f_0$  of the scanner. For the HF scanner the natural frequency is set by requirements, which means, that in order to achieve a high displacement the ratio of torque to inertia must be maximized. For the LF scanner the same principle applies, but an additional parameter of the natural frequency  $f_0$  can be manipulated to achieve maximum displacement. In both cases it is desired to keep the inertia of the scanner as low as possible.

### 3.3. Actuation methods

Three potentially feasible actuation methods were identified by the literature survey: piezo, voice coil and reluctance. The choice of actuation method greatly influences the design of the mechanism, therefore, these technologies are examined and compared in the following sections. The actuators motor constant, inertia of the mover and electrical response of the actuators are compared. For voice coils the motor constant is defined as[15]:

$$k_p = \frac{F}{\sqrt{P}} \quad (3.2)$$

where

$k_p$  = motor constant [N/ $\sqrt{W}$ ]

$F$  = actuator output force [N]

$P$  = actuator dissipated power [W]

The same expression will be used to evaluate the motor constant of the piezo and reluctance actuators. For coil devices that are driven by a coil, an important factor is the electrical time constant, which is determined as:

$$\tau = \frac{L}{R_{coil}} \quad (3.3)$$

where

$\tau$  = electrical time constant [s]

$L$  = inductance [H]

$R_{coil}$  = coil resistance [ $\Omega$ ]

#### 3.3.1. Piezo

COTS piezo actuators usually exhibit a maximum displacement of 1  $\mu\text{m}$  per 1 mm of piezo material. Therefore, piezo actuators are incompatible with the LF scanner as it requires a range of 1041  $\mu\text{m}$ , when no mechanical amplification is applied. Piezo actuator range is also problematic for the HF scanner, as without mechanical amplification the range required is 18  $\mu\text{m}$ , which would result in a piezo stack that is already at the limit of available space.

The next important parameter in design is price. For piezos a very rough estimation is 10 Eur/1  $\mu\text{m}$  of stroke. This means, that it is important to use a short stroke piezo to keep the price low. This price estimate would imply, that for a 18  $\mu\text{m}$  stroke piezo actuator the price would already be unfeasible. In order to reduce the stroke of the piezo, a mechanical amplification mechanism is required.

Additionally, the driving current and power can be relatively high when operating a piezo at high frequency. Current and power for a piezo are calculated as [20]:

$$I_{max} = \pi \cdot U_p \cdot f \cdot C \quad P_{ave} = U_p^2 \cdot f \cdot C \quad P_{max} = \pi \cdot U_p^2 \cdot f \cdot C \quad (3.4)$$

where

$I_{max}$  = maximum sinusoidal drive current [A]

$P_{max}$  = maximum power [W]

$P_{ave}$  = average power [W]

$U_p$  = peak to peak drive voltage [V]

$f$  = operating frequency [Hz]

$C$  = piezo actuator electrical capacitance [F]

Usually the driving voltage  $U_p$  for piezos is 120 V. The operating frequency  $f$  is set by requirements, therefore, the driving current is mainly determined by capacitance, which depends on the maximum travel range and cross section of the piezo. Figure 3.2 displays parameters of geometry, stroke and capacitance for COTS piezo actuators of *Physik Instrumente (PI)*.

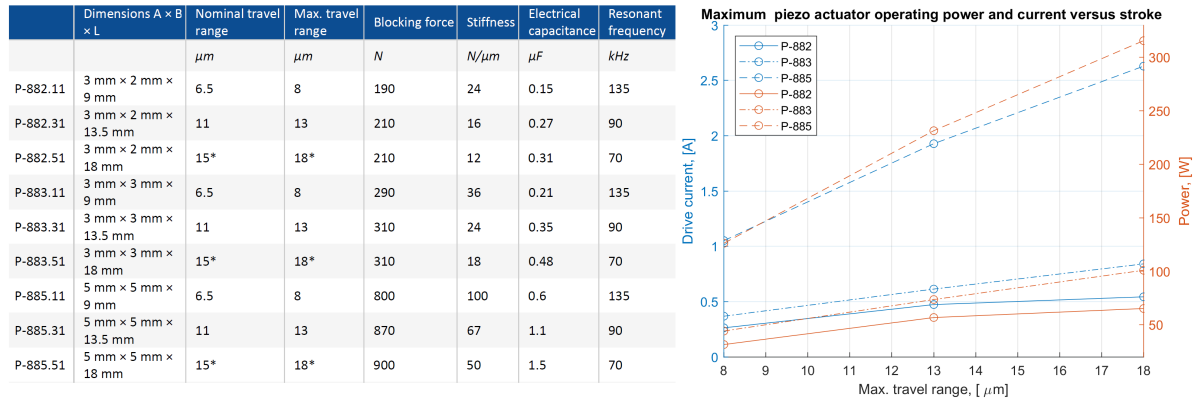


Figure 3.2: Left: Table with parameters of piezo actuators from *Physik Instrumente*. Right: Corresponding maximum piezo actuator operating current and power at the operational frequency of 4650 Hz.

Piezo actuators exhibit relatively high driving current and power at high frequency. For example the P-882.11 with the 8  $\mu\text{m}$  stroke requires a maximum current of 0.26 A and a peak power of 31.5 W. The electronics that drive the EasyScan HF scanner are only capable of maximum current of 40 mA with a  $\pm 5$  V voltage, which would amount to only 0.2 W at borderline conditions. The high power requirement also entails that there is thermal heating of the piezo. Appendix figure B.1 showcases the maximum operating frequency and maximum power consumption for piezo actuators of *Physik Instrumente*. The model P-882.11 is limited to an operating frequency of 200 Hz and power of 0.8 W when there is no measures for cooling of the actuator. In order to operate the piezo P-882.11 at the required frequency, additional measures for cooling would have to be taken, which complicates the design.

The high input energy requirement, combined with the relatively high price per  $\mu\text{m}$  of travel results in a problematic design. To make the piezo a feasible actuator, the stroke must be reduced to a minimum. The COTS piezo actuator with the shortest stroke available in the market is the PL022[19] which has a 2  $\mu\text{m}$  travel range and electrical capacitance of 25 nF. It requires only 43.8 mA of current and 5.25 W of power to drive at full stroke. This piezo actuator would require a mechanism with a mechanical advantage factor of at least 9 to reach the specified stroke of the HF scanner. Due to the small available space, such a configuration is not feasible.

The last option of implementing the piezo actuator would be use it as an inertial force generator to excite a desired oscillatory mode of the scanner. This configuration would result in the lowest amount of input energy due to efficient resonant operation. Figure 3.3 illustrates the configuration of scanning mechanism exited into a resonant mode by a piezo actuator.

For such a configuration it is important to determine what kind of inertial force the piezo would be able to generate. The generated force is calculated by:

$$F_{in} = 2m_c d_{st} (\pi f)^2 = 2\rho V_c d_{st} (\pi f)^2 \quad (3.5)$$

where

$F_{in}$  = maximum force generated by an oscillating counter mass [N]

$m_c$  = mass of the counterweight [kg]

$d_{st}$  = peak to peak travel range [m]

$\rho$  = material density [ $\text{kg}/\text{m}^3$ ]

$V_c$  = volume of the counter mass [ $\text{m}^3$ ]

$f$  = operating frequency [Hz]



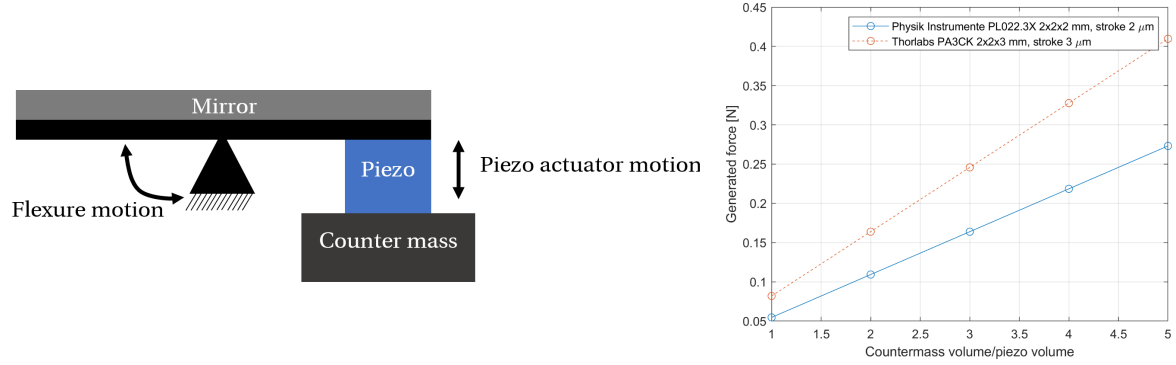


Figure 3.3: Left: flexure actuated by a piezo into a resonant mode. Right: Figure of maximum inertial force generated by the piezo

Since the frequency of the oscillation is set by operational requirements, the generated force is dependant upon the stroke of the piezo and the mass of the counter mass. To evaluate the force that can be generated by such a configuration, the volume of the counter mass is selected as a multiple of the volume of the corresponding piezo actuator. The material for the counter mass is selected as steel with density of  $\rho = 8000 \text{ kg/m}^3$ , as it a commonly used material with a relatively high density. The generated force values are displayed in the right side of figure 3.3 and are in the sub newton range. They will be used when comparing the different actuation methods.

### 3.3.2. Voice coil

Voice coils are devices, which utilize the Lorenz force for actuation. The Lorenz force is defined as:

$$F_L = l_w \mathbf{I} \times \mathbf{B} \quad (3.6)$$

where:

$F_L$  = Lorenz force [N]

$l_w$  = wire length [m]

$B$  = magnetic field density [T]

Voice coil actuators have the advantage, that the force output is almost independent from position and is linear with current. They also are available as COTS components, however, small versions are not as abundant. For example, the smallest available voice coil of *Akribis*[24] is showcased in figure 3.4. The voice coil has a stroke of 6.4 mm, therefore, is suitable for both the LF and HF cases. The price of this coil is 83 Eur/unit, which would take approximately half of the budget for a single scanner. The dimensions of the coil are of the same order of magnitude as the available space for both scanners, therefore, implementation of this exemplary coil would be problematic.

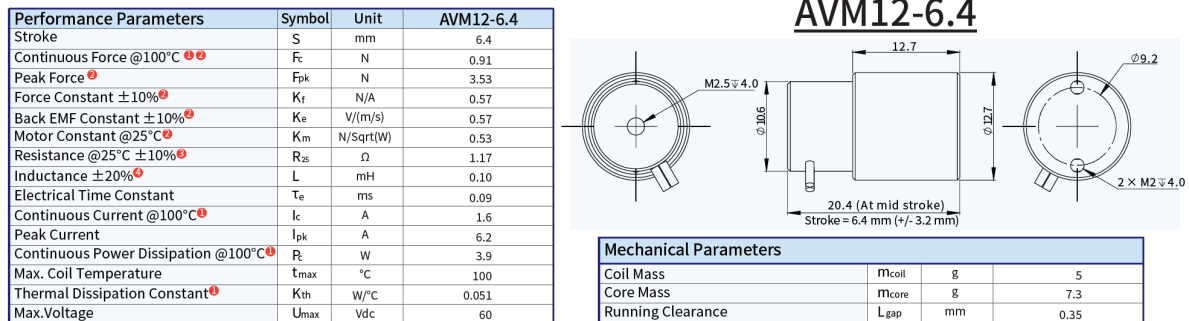


Figure 3.4: The smallest COTS voice coil of *Akribis* [24]

To compare voice coil performance with piezo and reluctance actuators an arbitrary configuration has to

be selected. Due to the fact that the voice coil and the reluctance actuator utilize similar physical phenomena to create force, their configurations have to be similar to fairly evaluate their performance. For this reason, a comparable magnetic circuit configuration will be used for both actuators. The configuration of the voice coil with its respective magnetic circuit is displayed in figure 3.5. Several assumptions are made to simplify the model:

- The gap between the outer surface of the mover and the yoke has the magnetic permeability of vacuum. The expression of the reluctance of this gap is simplified by assuming that the cross sectional area of the gap is constant and equal to  $2\pi d_c h_c$ .
- The gap between the inner surface of the mover and the yoke is considered 0.
- The magnetic permeability of the magnet is equal to that of vacuum, which is almost true for neodymium magnets [17].
- The yoke has a high magnetic permeability, therefore, the reluctance of the yoke is disregarded.

With such assumptions, by using the methodology explained in Appendix A, the magnetic flux density in the gap is calculated as:

$$B_v = \frac{B_m A_m l_m}{A_m t + \pi d_c h_c l_m} \quad (3.7)$$

where:

$B_m$  = remnant magnetic flux density of the magnet [T]

$A_m$  = magnet cross section [m<sup>2</sup>]

$l_m$  = magnet length [m]

$d_c$  = coil outer diameter [m]

$h_c$  = coil height [m]

$t$  = gap of magnetic permeability same as vacuum [m]

Combining equations 3.6 and 3.7 yields the output force of the voice coil actuator as:

$$F_v = \frac{\pi d_c N I B_m A_m l_m}{A_m t + \pi d_c h_c l_m} \quad (3.8)$$

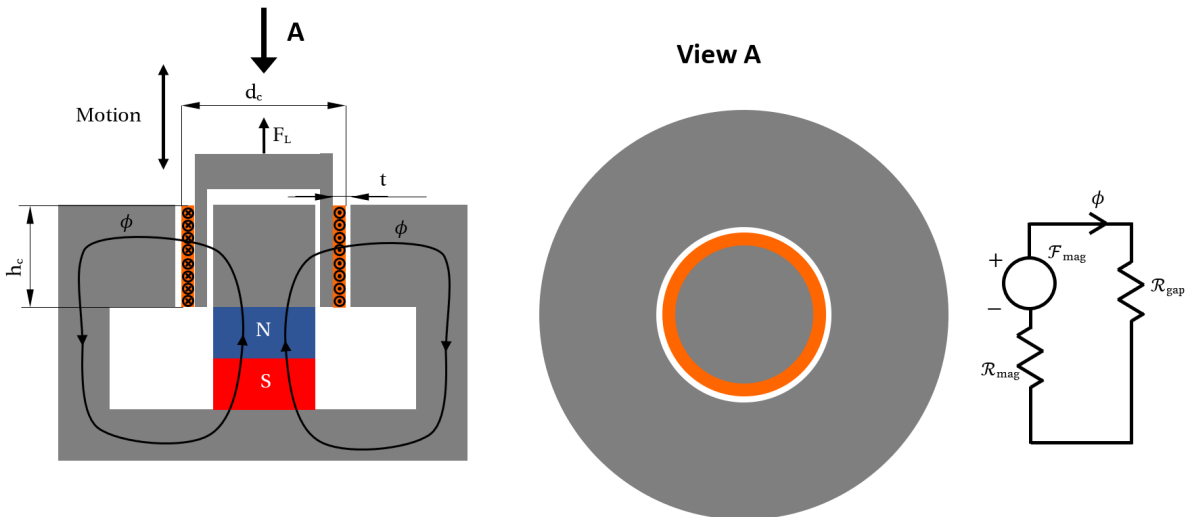


Figure 3.5: Left: Voice coil configuration - cross-section view. Center: Voice coil configuration - top view. Right: Magnetic circuit of the voice coil configuration.

### 3.3.3. Reluctance

Reluctance actuators are devices, which similarly to a voice coil also produce an output force due to electromagnetic phenomena. Unlike a voice coil actuator, the magnetic circuit does not maintain a constant reluctance during operation, hence the name reluctance actuator. Because of this, the output force of a reluctance actuator is position dependant. However, it will be demonstrated, that the output force is significantly higher than that of a voice coil actuator.

To have a fair comparison with the voice coil actuator, a magnetic circuit is used, which utilizes the same size magnet, amount of copper coil, air gap and corresponding surfaces size as the voice coil configuration. With such conditions, the reluctance actuator magnetic circuit produces the same amount of magnetic flux in air gap and the same magnetic flux density, as the voice coil magnetic circuit. It must be clarified, that this is true when the mover of the reluctance actuator is at the neutral position ( $x = 0$ ) and when no current is running through the coils of the reluctance actuator, as indicated by equation 3.9.

$$B_1(x = 0, I = 0) = B_2(x = 0, I = 0) = \frac{B_m A_m l_m}{A_m t + \pi d_c h_c l_m} \quad (3.9)$$

When the current is running through the coils, additional magnetic flux is added into the magnetic circuit. The magnetic flux of the coils reduces the magnetic flux on one side of the mover and increases on the other side. The difference creates a force unbalance acting on the mover and a net force. The output force of a reluctance actuator is calculated by methods explained in appendix A:

$$F_{rel}(x = 0) = \frac{B_1^2}{2A_c \mu_0} - \frac{B_2^2}{2A_c \mu_0} = \frac{B_1^2 - B_2^2}{2A_c \mu_0} \quad (3.10)$$

$$B_1(x = 0) = \frac{N A_m l_m t I \mu_0 \left( \frac{2B_r}{N I \mu_0} + \frac{1}{l_m} + \frac{\pi d h}{A_m t} \right)}{2t(A_m t + \pi d_c h l_m)} \quad (3.11)$$

$$B_2(x = 0) = \frac{N A_m l_m t I \mu_0 \left( \frac{2B_r}{N I \mu_0} - \frac{1}{l_m} - \frac{\pi d h}{A_m t} \right)}{2t(A_m t + \pi d_c h l_m)} \quad (3.12)$$

$$F_{rel}(x = 0) = \frac{\pi d_c h_c N I B_m A_m l_m}{2A_m t^2 + 2\pi d_c h_c l_m t} = \frac{h_c}{2t} \left( \frac{\pi d_c N I B_m A_m l_m}{A_m t + \pi d_c h_c l_m} \right) = \frac{h_c}{2t} F_v \quad (3.13)$$

Equation 3.13 indicates that the ratio of reluctance to voice coil output force depends on the ratio of air gap height  $h_c$  to thickness  $t$ . Usually the height of the gap is significantly higher than the thickness to reduce reluctance of the air gap and minimize fringing. Therefore, in general, the output force of the reluctance actuator is higher than that of the voice coil.

### 3.3.4. Comparison

The first comparison criteria is the motor constant. For the voice coil the motor constant simplifies to:

$$P = I^2 R = J^2 A_w^2 \rho_c \frac{l_w}{A_w} = J^2 V_c \rho_l \quad F_{voic} = B l I \quad k_{pvoic} = \frac{B l_w I}{\sqrt{J^2 V_c \rho_c}} = B \sqrt{\frac{V_c}{\rho_c}} \quad (3.14)$$

where

$J$  = current density [A/m<sup>2</sup>]

$V_c$  = coil volume [m<sup>3</sup>]

$\rho_c$  = coil wire electrical resistivity [ $\Omega$ m]  $l_w$  = wire length [m]

$A_w$  = wire cross-section [m<sup>2</sup>]

Expressing the current flowing through the coil by current density  $J$  and wire cross section  $A_w$  allows to find the expression for the motor constant via three parameters: magnetic field density  $B$ , coil volume  $V_c$  and wire resistivity  $\rho_c$ . Inserting equation 3.7 into equation 3.14 yields the final expression for the voice motor constant  $k_p$ :

$$k_{pvoic} = \frac{B_m A_m l_m}{A_m t + \pi d_c h_c l_m} \sqrt{\frac{V_c}{\rho_c}} \quad (3.15)$$

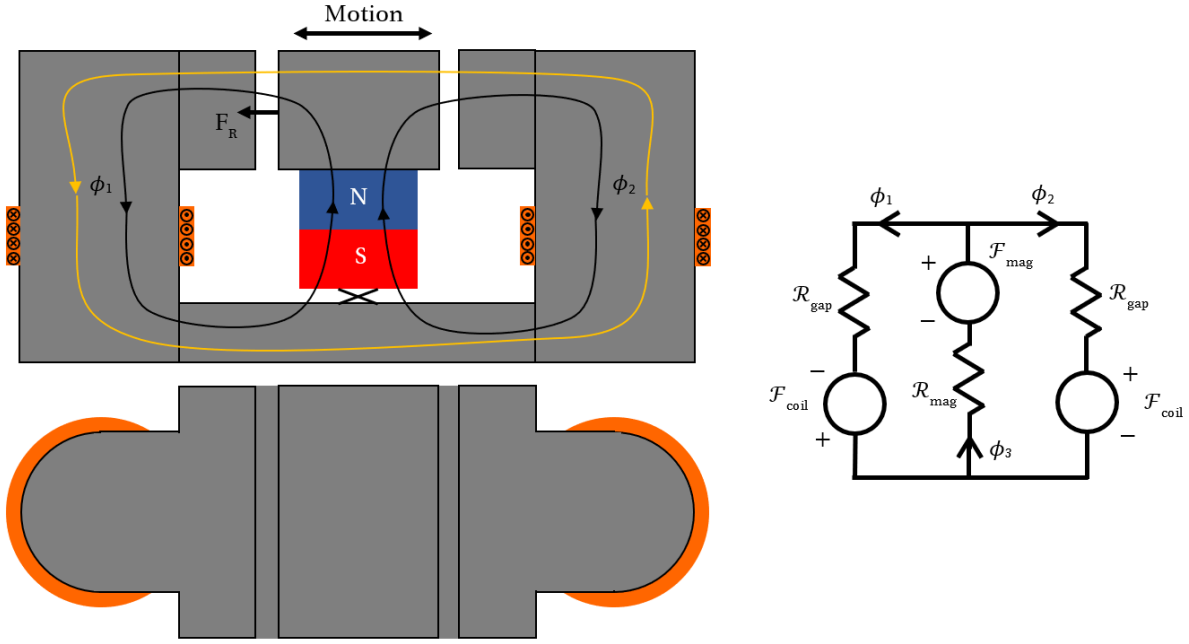


Figure 3.6: Left: Reluctance actuator configuration. Right: Magnetic circuit of reluctance actuator.

For the reluctance actuator the motor constant is expressed as:

$$k_{Prel} = \frac{h_c}{2t} \left( \frac{\pi d_c N I B_m A_m l_m}{A_m t + \pi d_c h_c l_m} \right) \frac{1}{J \sqrt{V_c \rho_c}} = \frac{h_c}{2t} \left( \frac{B_m A_m l_m}{A_m t + \pi d_c h_c l_m} \right) \sqrt{\frac{V_c}{\rho_c}} \quad (3.16)$$

For the inertial piezo actuator the motor constant is expressed as:

$$k_{Piezo} = \frac{2\rho V_c d_{st} (\pi f)^2}{U_p^2 f C} = \frac{2\rho V_c d_{st} \pi^2 f}{U_p^2 C} \quad (3.17)$$

Numerical values have to be assigned to all the parameters, that amount to the expressions of motor constants, for them to be evaluated and compared.

For the piezo actuator, the only parameters that need to be selected are the volume of the counter mass and the piezo actuator model. Other parameters are determined by operational requirements. The smallest  $2\ \mu\text{m}$  stroke piezo model is selected. The volume of the counter mass is assumed to be three times larger than that of the piezo actuator, which is reasonable, considering the dimensions of the mirror that needs to be moved.

The voice coil and reluctance actuator magnetic circuit configurations are defined to have the same amount of magnetic flux density, therefore, the parameters that are needed to determine the motor constant are assumed to be the same in both cases. As indicated by equation 3.2, the motor constant increases linearly with magnetic flux density. The magnetic flux density in ferromagnetic yokes is limited by the saturation flux of the used material. High quality ferromagnetic materials have saturation flux of about 2 T [5], however, they are more complicated to acquire when dealing with small series production. Lower magnetic quality, but widely obtainable material, such as AISI430 has a flux density of 1.4 T [31]. The parameters of the magnetic circuit, required to achieve this flux density, are determined to be:

$B_m$	$l_m$	$t$	$d_c$	$h_c$	$\rho_I$	$A_m$	$J$
1.3 T	3 mm	0.5 mm	9 mm	1.5 mm	$1.68 \times 10^{-8} \Omega\text{m}$	$(d_c - t)^2 \pi / 4$	$1 \times 10^7 \text{ A/m}^2$

Table 3.1: Magnetic circuit parameters for comparison of actuators

With such parameters, the size of the voice coil and reluctance actuator are such, that they fulfil the size

requirement of the HF scanner. The calculated output force for each of the actuator and their corresponding motor constants along with additional relevant operational parameters are displayed in figure 3.7.

The calculated values indicate that the output force of all actuator configurations are of the same order of magnitude, however, the motor constant of the piezo actuator is several orders of magnitude lower than that of the voice coil or reluctance actuator. This makes the piezo actuator highly inefficient. In addition, the inherent design of the resonant piezo actuator has a flaw, that during operation the piezo experiences equal compressive and tensional loads. This can be problematic, as the load bearing capacity in tension is 2 MPa, while in compression is 30 MPa. Also the output force of a resonant piezo actuator is linear with the mass of the counterweight, which means that increasing the mass would become detrimental to the performance, due to increased inertia of the system. One area where the piezo is better than voice coil or reluctance actuators is its size. Piezo is the smallest actuator as it does not require the yoke structure, which in itself takes up space.

Voice coil and reluctance actuators show similar performance parameters, however, the latter edges out in force generation capability. To make a significant distinction between the performance of these two actuators, other parameters need to be examined. One of them is the mass of the mover. For the voice coil, the mover can be either the coil assembly or the yoke assembly. When the mover is the coil assembly, the wire connections introduce parasitic forces. When the mover is the yoke assembly, the mass increases significantly, but then the mover is only mechanically coupled to the actuated object. For the reluctance actuator the mover can be configured to be a small part of ferromagnetic material or even the magnet itself, but what is most important, it that the mover is not the coil. Therefore, the reluctance actuator can have a significantly lower mover mass than that of the voice coil.

The electrical response time for both actuators is determined by the inductance of the coils, and here the voice coil has the edge, as they tend to have a smaller amount of coils, because the coil volume influences the required air gap size and thus, the reluctance. The reluctance actuator does not have this restriction, therefore, it can have a much larger number of coils than the voice coil resulting in a larger time constant, but improved force output.

Properties	Piezo	Voice coil	Reluctance
Output force [N]	0,169	0,306	0,452
Motor constant [N $\sqrt{W}$ ]	0,071 (Inefficient)	1,553 (Efficient)	2,466 (Efficient)
Inertia	Problematic relation with output force	Can be high	Can be low
Electrical response	Very fast	Fast	Can be slow
COTS	Yes	Yes	No
HF/LF compatible	HF	HF/LF	HF/LF
Footprint	Smallest should fit	Borderline acceptable	Borderline acceptable
Particularities	Tension load limit only 2 MPa	Output force position independent (almost)	Output position dependent

Figure 3.7: Computed output force and motor constant for the selected actuator configurations with additional relevant parameter

The resonant piezo actuator configuration is the most compact of all considered actuators, however, the low efficiency and an inherently limited force output make it a very unappealing choice. Therefore, the choice between voice coil and reluctance actuators must be made. Even though the reluctance actuator may lack advantage in electrical response when compared to the voice coil, the high force output to power ratio, and low mover inertia make it the best choice, when considering that the designed device must fit into a very small space. The required motion displacements are relatively small and the power used needs to be feasible. For these reasons the reluctance actuator is chosen as the actuation method for both the LF and HF scanners.

### 3.4. Guiding mechanisms

The guiding of the scanner must be such, that a 1 DOF rotational motion is achieved, while having sufficient support stiffness in the constrained DOF. The required angles of rotation are  $\pm 3$  mrad and  $\pm 130.5$  mrad for the HF and LF scanner respectively. Due to the limited space allocated for each scanner, the guiding mechanism

must be compact. Additionally, the guiding mechanism must be easy to manufacture in order to fit into the low budget requirement.

### 3.4.1. Bearings

Rotational bearings have been around for centuries and are the backbone of technology. Many various types of bearings exist: ball bearings, bushings, fluid bearing, magnetic bearings and others. They have high support stiffness and are of capable continuous rotation angles. However, they all suffer from having backlash and friction, which may inhibit their performance in high precision devices. While air bearings and magnetic bears suffer much less from friction, there are always some of these phenomena at play. Therefore, in a mechanism which utilizes bearings, it is conventional to use feedback to track the position of the mechanism, in order to compensate for the mentioned phenomena.

Rotational bearings may not be an optimal solution as the guiding mechanism for the scanner mirrors, because the rotation angle requirements are very small ( $\pm 130$  mrad). Also the current system does not support position tracking of the scanners, as it is operated in open loop. Therefore, additional resources would have to be used to incorporate sensors and feedback electronics into a space and budget that is already limited.

### 3.4.2. Flexures

Flexure mechanisms utilize elastic deformation to guide the mover. Therefore when the flexure operates within the elastic regime, it is not experiencing friction or play, which is highly desirable in a precision mechanism. The drawback to flexures is that they have a limited range, with a rough maximum value of a few dozen degrees. Also, the support stiffness of the constrained DOF can be decreasing with the flexure rotation angle. Fortunately, the requirement of scan angle falls into the suitable range for flexure guiding mechanisms.

Unlike bearings, flexure mechanisms are more often custom designed for mechanisms, than found as a COTS product. A good general approach to discovering possible flexure design is to utilize the FACT [29] methodology. One rotational DOF system is described by a freedom space and a constraint space as showcased in figure 3.8. The constrain space consists of at least two intersecting planes whose intersection generates the axis of rotation.

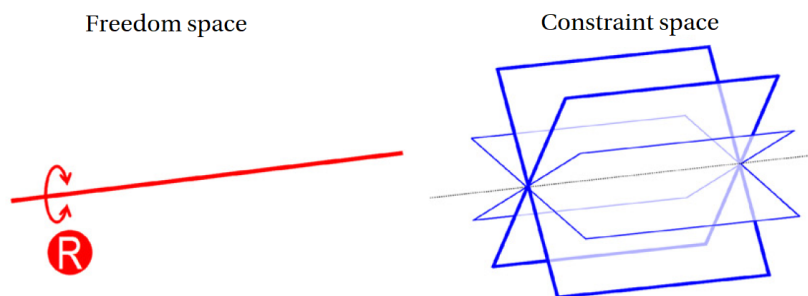


Figure 3.8: Freedom and constraint spaces for a 1 DOF rotational flexure described by FACT methodology [29]

An example of such a flexure would be a torsion beam with an X shaped cross section illustrated in the left side of figure 3.9. The torsion beam is compliant in rotation, but stiff in other DOF. At first glance it may look like a very simple design, however, manufacturing such a beam in dimensions of a few millimetres may prove challenging and expensive. Additional surfaces also need to be manufactured on which a flat mirror can be mounted.

A more manufacturable torsion beam that still is stiff in the constrained degrees of freedom is the U shape torsion beam, showcased in the centre of figure 3.9. This beam could be made from a flat sheet of metal and bent to form the required curvature. However, due to small dimensions of the beam the bending may be complicated to do and require special tooling.

The most easily manufacturable is the flat torsion beam, showcased in the right side of figure 3.9. However, it must be noted that due to the requirement of at least two flat intersecting constraint planes defined by the FACT methodology, this torsion beam becomes unconstrained. This can be counteracted by realizing that the beam still has some stiffness in the unconstrained degrees of freedom. Therefore, the geometry of the beam may be optimized so that the stiffness of the unconstrained DOF is sufficient. The flat torsion beam

can be cut out from sheet metal with conventional methods like water jet, laser, electrochemical etching, wire EDM and even stamped with a die.

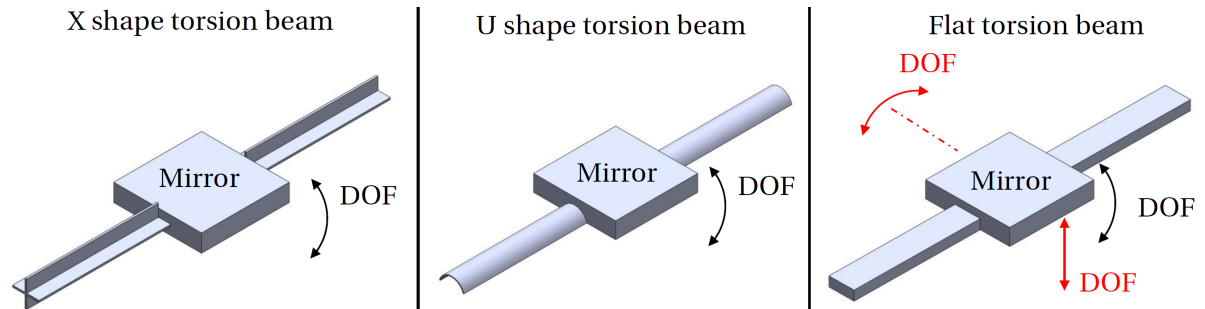


Figure 3.9: Torsion beam concepts

Another version of a one DOF rotational guiding mechanism is the cross flexure. Several configurations of the cross flexure are showcased in figure 3.10. As per the FACT methodology, the rotation axis of these flexures is located at the intersection of the leaf flexures. However, due to the construction of the flexure the point of rotation can be closer or farther from the rotating body. In a scanning application it is desired to have the axis of rotation as close as possible to the mirror in order to not have a lateral displacement of the beam on the mirror. The double symmetric cross spring pivot deals with this issue the best, as the axis of rotation is the closest to the mover of all showcased cross flexure configurations. The cross flexure can be designed to be assembled from sheet metal or manufactured as a monolith. Assembly is not favourable in this project because the dimensions of the flexure would be only of a few millimetres, making it tedious and time consuming. Manufacturing the cross flexure from a monolith could be done by a water jet cutter or by a wire EDM. However, depending on the geometry, fine features may be problematic for a water jet. EDM does not have problems with fine features, as it can reach accuracies of a few micrometers, however is a relatively expensive machining process.

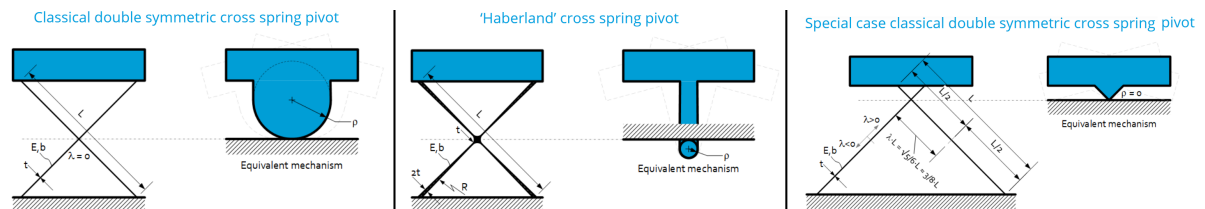


Figure 3.10: Cross flexure designs by JPE B.V. [7]

Very similar to the cross flexure is the notch flexure illustrated in figure 3.11. The flexure is usually manufactured by drilling/milling holes and sawing slots. It is limited to a range of  $1^\circ$  and is more often used to add an additional DOF, than for a dynamic application. [34].

A very sophisticated rotational mechanism is the butterfly flexure, showcased in figure 3.11. It is capable of achieving a maximum rotation of  $15^\circ$ , while keeping its centre of rotation stably positioned within micrometer accuracy [30]. It consists of 4 pairs of leaf flexures, therefore, is able to achieve such a high rotation angle. The butterfly hinge is manufactured from a monolith by wire EDM. While it is an impressive mechanism in general it consists of many features, therefore, miniaturising such a mechanism may prove to be very complicated. Also, due to the many features in the butterfly hinge, the axis of rotation is a distance equal to half height of the hinge away from the mover. Additionally, it has a relatively large footprint, which is undesired where the space is already limited

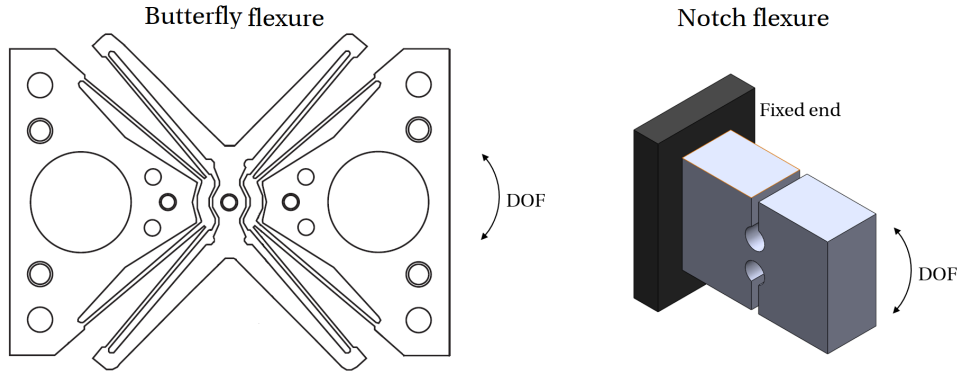


Figure 3.11: Left: Butterfly flexure[30]. Right: Notch flexure.

All the relevant properties of the discussed flexures are summarized in table 3.2. The especially restricting requirements on available space and price of the scanner, limit the flexure design possibilities. To minimize the foot print of the guiding mechanism, the torsion beam type flexures must be selected. Due to the very complex manufacturing and integration of the X shaped torsion beam it will not be a financially feasible solution. Then only options left are the U shaped and flat torsion beam models. The bending of the U shaped beam may prove to be complicated to arrange for such tiny flexures at this low manufacturing volume. Therefore, the risk of having a poorly constrained flexure must be taken by choosing the flat torsion beam.

Flexure model	Manufacturability	Foot print	Support stiffness
X shaped torsion beam	Very complex	Small	High
U shaped torsion beam	Complex	Small	Medium
Flat torsion beam	Simple	Small	2 DOF unconstrained
Cross flexure	Complex	Big	High
Notched flexure	Simple	Medium	High
Butterfly flexure	Very complex	Big	High

Table 3.2: Rotational DOF flexure comparison

### 3.5. Scanner concept feasibility

With the guiding mechanism and actuation method selected, the next challenge is to combine these elements together to form a cohesive device. This is done in the following sections of chapter 4. In most of the situations a damping coefficient of 5 % will be assumed, which is a typical value for metal structures with joints [8].

A preliminary evaluation of what could be achieved with this type of scanner can be made by approximating some values. For example, even though the inertia of the scanner is not yet determined, the moment of inertia of the HF mirror can already be estimated by using formulas from appendix D. The rotational inertia of the HF mirror around the axis of rotation going through the centre of mass is  $I_{mirror} = 0.26 \text{ kgm}^2$ . An assumption can be made, that the total scanner inertia would be ten times higher than the inertia of the mirror  $10I_{mirror} \approx I_{HF}$ . The actuating force that was estimated in figure 3.7 can be assumed to be acting on the edge facet of the mirror (figure 1.7). If the resonance frequency of the HF scanner would be the same as operational, the resultant amplitude achieved, calculated by equation 3.1 would be  $\theta_{dyn} = \pm 6.1 \text{ mrad}$ . The estimate is the same order as the requirement, therefore, is a good sign that the real device should have potential of achieving the requirements.



# 4

## Detailed scanner design

### 4.1. Detailed design outline

The selected actuator type is the reluctance force actuator. It has the property of negative magnetic stiffness. Therefore the output of the actuator is influenced by the rotation of the scanner, which influences the required mechanical stiffness of the guiding mechanism. Depending on how the reluctance actuator is implemented, the inertia of the scanner can vary drastically, which is especially important in order to determine the required stiffness of the HF scanner. For these reasons the magnetic actuator must be designed first, then the mechanical design can follow. The general design plan is outlined as:

- Determine the magnetic circuit configuration in order to find the configuration, which has the most torque/current ratio.
- Determine the parameters of the magnetic circuit: gap sizes, magnet, coil.
- With the parameters of the actuator known, determine the required stiffness of the flexures.
- Determine the geometry of the flexures.
- Create a final assembly for the actuators.

### 4.2. Magnetic design

#### 4.2.1. Magnetic circuit selection

To achieve a high torque to inertia ratio, the magnetic circuit needs to be configured optimally. Several magnetic circuits and their significant features are described in table 4.2. The output force of each configuration is calculated by the method explained in appendix A. Scanner rotation for each configuration is considered  $x=0$  rad, and therefore, rotation is not considered a variable in this comparison.

Even though the scanner is a rotational mechanism, in this comparison, force is evaluated instead of torque. The reason for this is that geometry affects the achievable torque. To have a more fundamental comparison geometry is not considered apart from circuit parameters, such as air gap size, magnet size. The air gap cross sections are considered to be equal to that of the magnet cross section, and yoke reluctance is disregarded. The expression of the output force for each of the configuration is significantly different, so that it is difficult to make a comparison between circuits without assigning numeric values to variables, therefore, numeric values are assumed and are listed in table 4.1.

$B_m$	$l_m$	$A_m$	$g_c$	$I_c$	$x$	$g_0$	$N$
1.35 T	2 mm	4 mm <sup>2</sup>	0.2 mm	0.25 A	0 rad	1 mm	600

Table 4.1: Magnetic circuit numeric values assumed for comparison of different circuits

Almost all of the configurations are similar in the manner, that the flux of the gaps is considered to be perpendicular to the cross-section of the gap. Where this condition is applicable, the gap dimensions for all of the configurations are considered the same.

The only exception is configuration 4, where the flux crossing the magnets end faces is assumed to be two directional and is separated into two components: normal and tangential. The normal components of the flux are represented as  $\phi_5$  and  $\phi_6$ , the tangential components are represented as  $\phi_2$  and  $\phi_3$ . When a tangential component of the flux is also present on an object, the force acting on that surface has a different expression than described in equation A.16. Equation A.17 takes into account normal and tangential magnetic fields. Flux air gaps  $\mathcal{R}_{LU}$  and  $\mathcal{R}_{RU}$  are considered to have the same reluctance values as other configurations. The reluctances  $\mathcal{R}_{LL}$  and  $\mathcal{R}_{RL}$ , through which the tangential part of the flux passes, are assumed to be twice the magnet reluctance each. This assumption is an approximate guess, as the only way to predict the reluctance of these gaps is by doing FEA of the magnetic circuit. Figure 4.1 illustrates the assumed magnetic flux and force directions. A detailed list of all the reluctance, MMF and force expressions of each circuit configuration is listed in appendix C.

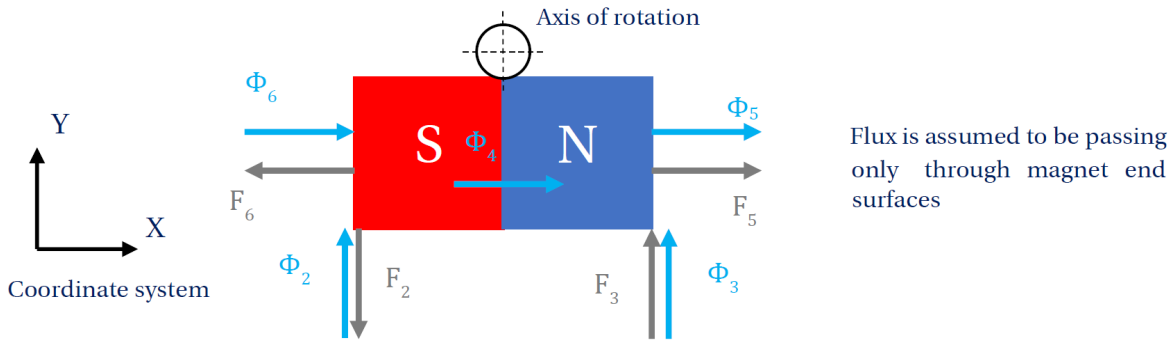


Figure 4.1: Assumed flux and force direction for the configuration 4 magnetic circuit

As indicated by table 4.2, all of the magnetic circuit configurations are able to achieve forces of the same order of magnitude, therefore, other parameters that describe their performance need to be examined. Force loop-wise the best configuration would be 3, as the total force that it outputs cancels each other and only a net torque is present, which would be an ideal situation. However, such a configuration is rather complicated, due to the need of having the yoke both below and above the mover. Also separate yoke pieces need to be mounted on the flexure which increases the inertia. Due to the small space requirement, it would be very difficult to implement such a configuration without having lots of flux losses, due to there being an inner and an outer yoke. Therefore, this configuration is not chosen.

When comparing configurations 1 and 2, it becomes clear that more magnets do not mean better performance, because the reluctance of the magnet is almost the same as vacuum. Therefore, configuration 2 can be disregarded.

Configuration 5 has the problem that it utilizes only half of the available space with respect to the oscillating mirror. Cramping the magnetic yoke in a such a small space would result in high fringing flux losses. The output force could be increased by making the design symmetrical with the same type of magnet yoke on the left side of the flexure, but that would still not solve the problem of the yoke cramped into a very small space. This is especially true, when considering the HF mirror, which has a size requirement of 7 x 6 mm. Therefore, this configuration is not chosen.

Configurations 1 and 4 show similar force output performance, however, configuration 4 is simpler, as it only requires a single coil. Also, in configuration 4 the mover is the magnet, which would result in a low inertia. Additionally, the yoke can be positioned from the bottom and from the sides of the magnet which would utilize the available space better and reduce fringing. However, many of the assumptions about flux direction and reluctance values for configuration 4 are not sound and are based on an approximate guess, therefore, configurations 1 and 4 need to be simulated with FEA to check, what is the actual performance of these configurations.

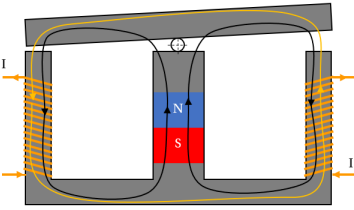
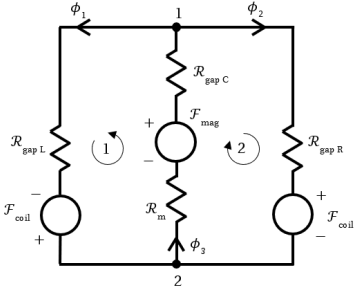
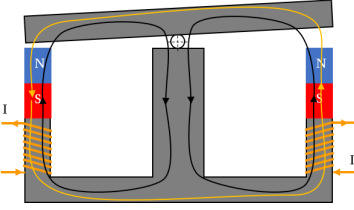
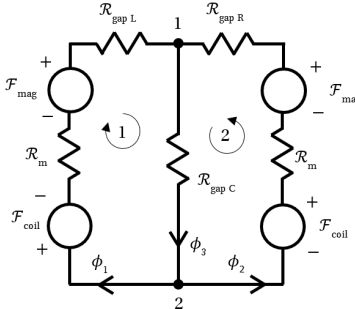
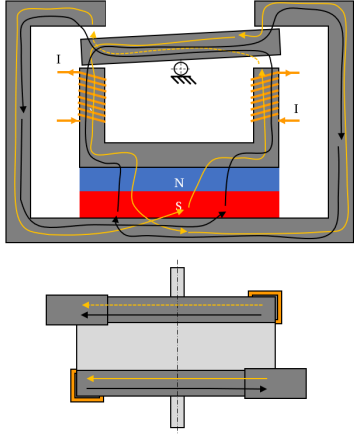
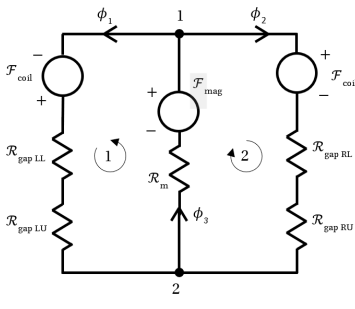
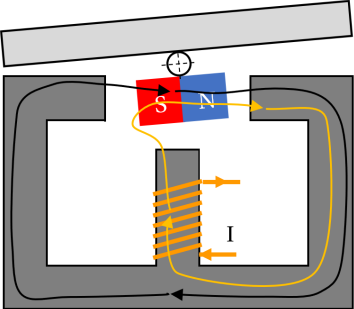
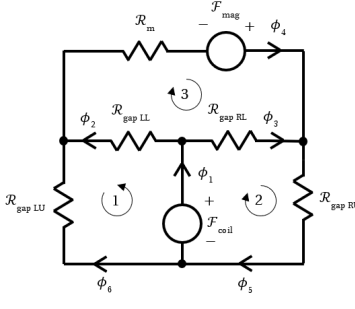
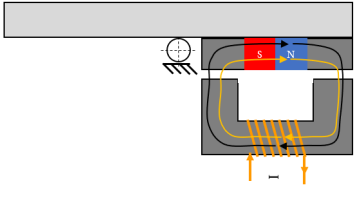
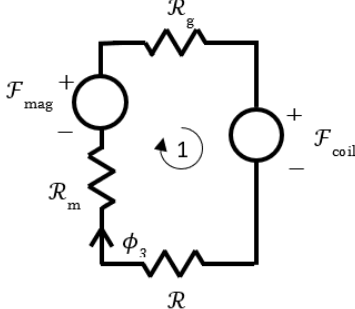
	Configuration	Schematic	Output force significant characteristics
1			$F = 0.3\text{ N}$ Bi-directional actuation Net vertical force
2			$F = 0.159\text{ N}$ Bi-directional actuation Net vertical force
3			$F = 0.27\text{ N}$ Bi-directional actuation Net zero force, only torque
4			$F = 0.288\text{ N}$ Bi-directional actuation Net vertical force Lowest inertia design
5			$F_{act} = 0.238\text{ N}$ One directional actuation Net vertical force Net force at no current $I = 0$

Table 4.2: Magnetic circuit configuration

### 4.2.2. Magnetic circuit FEA comparison

The FEA multi physics package *COMSOL* is used to validate the magnetic circuit configurations. Each of the configurations is modelled in three dimension. To save computation time, each of the model is sliced in half and a symmetry condition of magnetic insulation is used. The magnetic insulation condition states, that the magnetic field is tangential to the symmetry plane. Because the model is symmetric, the force on the mover in the X direction is equal to zero. For the same reason, torques around the Z and Y axes are also equal to zero. The magnetic forces are computed on each mover of the respective configuration, by computing the Maxwell stress tensor. The X axis passes through the centre of the torsion beam's cross section. The torque on the mover is calculated with respect to this axis. The *COMSOL* model is showcased figure 4.2. The Maxwell stress tensor is sensitive to mesh size, therefore, a fine mesh is used for the surface of the mover.

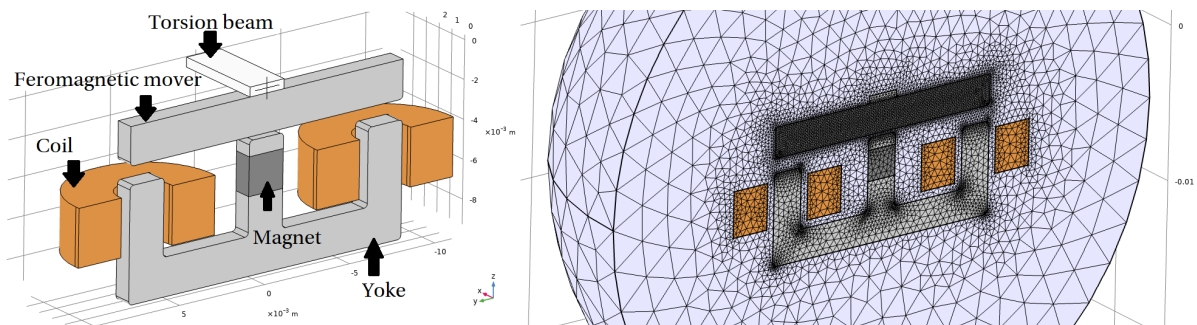


Figure 4.2: COMSOL model of magnetic circuit configuration 1.

Same numerical values are assumed for the remnant flux density of the magnet, gap size, magnet size, current, winding number, as also assumed in section 4.2.1. The geometry of the coils is selected arbitrarily. The combined volume of the two coils of configuration 1 is equal to the volume of the single coil of configuration 4. However, the geometry of the coil does not influence the computed magnetic field in the yoke significantly, as long the yoke is located inside of the coil. In *COMSOL* it is sufficient to input the current running through the coil and the winding number of the coil, irrespective of what is the coil geometry. Therefore, by modelling two coils with 300 windings for the first actuator configuration and a single coil with 600 windings for the configuration 4, the total magneto motive force generated by the coils is equal in both configurations. This makes the comparison of both configurations fair. Iron is selected as the material for the yoke with relative permeability of  $\mu_{IR} = 4000$ , however, this is only a preliminary choice for simulation purposes. A deeper discussion on ferromagnetic material selection can be found in section 4.2.3. The computed magnetic field plots of configurations 1 and 4 are displayed in figure 4.3. In table 4.3 the output forces and torques are listed for each of the configuration.

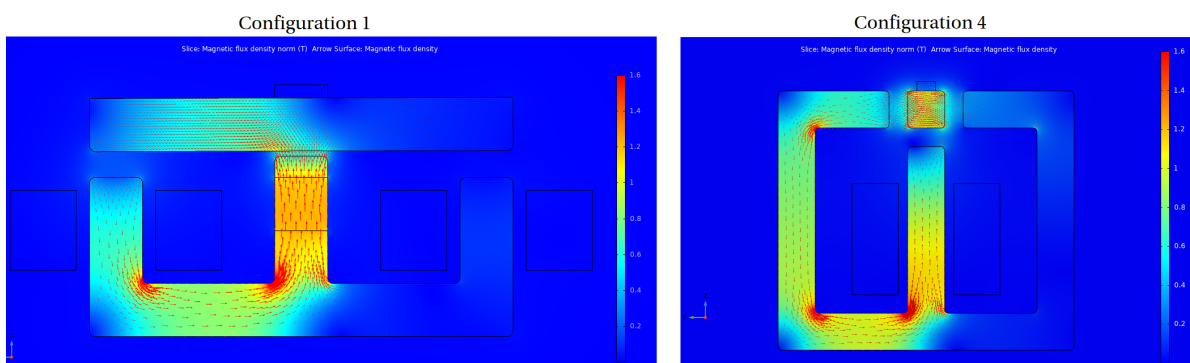


Figure 4.3: Magnetic field density distributions of circuit configurations 1 and 4

The results show that the output torque of both configurations is the same order of magnitude. The torque of configuration 1 is higher only by 6.5%. The output force in the Y axis of configuration 4 is a magnitude higher than configuration 1, which is to be expected, as the flux in the gap between magnet and the yoke of configuration 4 is directed in the Y axis. The forces in the Z direction exhibit similar, but opposite situation, which is also explained by the flux direction in the air gap of configuration 1. What is important to note, is that

the mover of the configuration 1 experiences mainly vertical pulling forces, because flux in the air gaps has primarily a vertical direction. If the gaps were to be reduced to increase the magnetic flux and consequently the torque, it would mostly result in increased vertical force. For configuration 4 the air gaps are directed in both the vertical and in the horizontal direction. Therefore, decreasing the gap sizes in this configuration would result in increased vertical and horizontal forces, which makes this configuration more balanced and not overloaded in a single direction.

Configuration	Output torque [Nm]		Output force Y axis [N]		Output force Z axis [N]	
	t = 0.5 mm	t = 1 mm	t = 0.5 mm	t = 1 mm	t = 0.5 mm	t = 1 mm
1	$-1.429 \times 10^{-3}$	$-4.901 \times 10^{-4}$	0.0199	0.0135	-1.092	-0.729
1+	$1.546 \times 10^{-4}$	$4.232 \times 10^{-5}$	0.1226	0.0331	-0.1248	-0.0501
4	$8.579 \times 10^{-4}$	$4.600 \times 10^{-4}$	0.384	0.176	-0.0633	-0.0218

Table 4.3: Computed output forces and torques of circuit configurations 1, 1+ and 4 with respect to the air gap size  $t$

Another important factor of the design is inertia of the mover. As it was discussed in chapter 3.2, it is important to have the inertia of the mover as low as possible to be able to achieve a high amplitude with a given torque. To increase the output torque in configuration 1, the air gaps have to be positioned as far as possible from the axis of rotation to a maximum moment arm. In order to increase the lever arm, the length of the mover also has to be increased, which negatively impacts the inertia. Additionally, an increasing lever arm at some point would start to negatively impact the performance, as inertia is proportional to the square of the distance to the axis of rotation, whereas, the torque has a linear relationship with the distance. The modelled configuration 1 has a mover length of 16 mm, which is practically the longest mover that could fit in the available space of the HF scanner. This means, that there are no more opportunities to increase the moment lever arm for this configuration. Another drawback of having a long lever arm is that it increases the gap size between the yoke as the mover requires clearance. While this is not significant for the HF scanner due to the small rotation angle, it is significant for the LF scanner. The currently modelled configuration already requires a clearance of:  $\sin(130.5 \text{ mrad}) \cdot 8 \text{ mm} = 1.04 \text{ mm}$ . With a gap size of 1 mm, the actuator is already at the clearance limit which means that increasing actuator efficiency by decreasing the gap size is not possible. When configuration 1 is compared to configuration 4 with respect to inertia, it is clear that configuration 4 has an advantage, as the mover is positioned very closely to the axis of rotation, but achieves almost the same amount of torque, as configuration 1, while having an inertia that is 260 times lower.

A slight adjustment of the yoke layout in configuration 1 can improve on the mentioned drawbacks. Making the mover size equal as the mover in configuration 4 and mimicking the yoke layout results in a more balanced force distribution, and inertia same as configuration 4. These improvements do not change the magnetic circuit. This configuration is named as configuration 1+ and is displayed in figure 4.4.

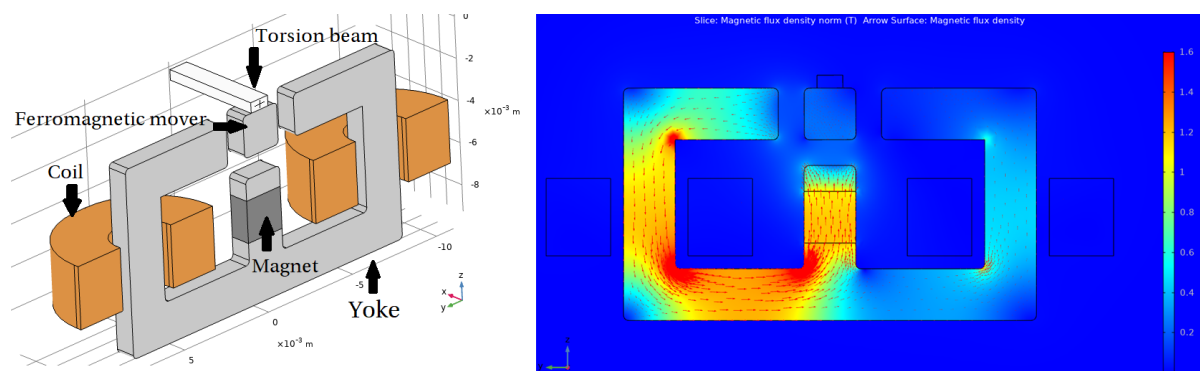


Figure 4.4: Configuration 1+ based model and computed magnetic field

Even though the configuration 1+ has an improved design, when compared to configuration 1, the output torque is significantly lower than that of configuration 4. As a final effort in trying to compare the different configurations, the gap sizes were reduced from 1 mm to 0.5 mm. The idea behind this reduction is that the gap size influences each of the configuration differently. The computed values were listed in table 4.3. For

configuration 1 and 1+, the torque output increased almost three times, whereas, for configuration 4, only doubled. With a reduced gap size, the torque output for configuration 1 became larger than configuration 4, however configuration 1 would not be feasible with such a small gap size for the LF scanner, due to the required clearance. However, configuration 1 still suffers from having a large inertia. Because configuration 1+ is not capable of delivering significantly larger output torque than configuration 4, it is concluded, that configuration 4 is the most optimal and is used for the design of the scanners.

Because the analytical model of configuration 4 is not sound, as values for reluctance are approximate guesses, it is more accurate to determine the actuator parameters only from FEA. Therefore, in the rest of this thesis, FEA will be used to determine the optimal magnetic circuit parameters.

### 4.2.3. Magnetic material general properties

Magnetic materials are usually separated into two groups: magnetically hard and soft. Magnetically hard materials retain a high magnetisation after they have been magnetised, and the opposite is true for soft materials. The material property that determines the materials resistance to being demagnetized is called magnetic coercivity  $H_c$  [6]. In a ferromagnetic material, the coercivity is the value of the applied magnetic field  $H$  required to make the magnetic flux density in the material zero, after the material was driven to saturation. Ferromagnetic yokes need have low coercivity, while permanent magnets need high coercivity.

Another important magnetic property is magnetic permeability  $\mu$ , which is usually expressed with respect to magnetic permeability of vacuum  $\mu_0$  by use of relative magnetic permeability  $\mu_r$ :

$$\mu = \mu_0 \mu_r \quad (4.1)$$

It is important to note, that the magnetic permeability of a material is dependant upon the magnetic field  $H$  that is acting upon the material. When the material is fully magnetised, it reaches the saturation flux density  $B_s$  and then the permeability of magnetised materials becomes equal to that of vacuum  $\mu_0$ . It is desired for a good quality soft magnetic material to have high magnetic permeability and high saturation flux density  $B_s$ .

### 4.2.4. Magnetically soft materials

Table 4.4 showcases common magnetically soft materials:

Material	Max. relative permeability $\mu_r$ [-]	Saturation flux density $B_s$ [T]	Coercivity $H_c$ [A/m]
Mu-metal	60000 - 240000 [16]	0.75	80
Armco Pure Iron	2500 - 19000 [5]	2.1	200
AISI 420	450 [31]	1.4	820
AISI 430	950 - 1830 [31]	1.5	380
AISI 430FR	600 - 1100 [1]	1.5	270
IMRE	960 [31]	1.6	200
UGIPERM 12FM	2000	1.6	200
	3000	1.7	125

Table 4.4: Magnetically soft materials

Data indicates that materials Armco Pure Iron and UGIPER 12FM have the best magnetic properties available. Unfortunately, the mentioned materials are complicated to obtain and optimize for small series manufacturing. Therefore, a material that is widely available in the required form (sheet metal, round bar), but still performs well, must be chosen. One such material is AISI430, as it is widely available worldwide and relatively cheap. To ensure that optimal operation is still maintained with a lower quality material, AISI430 steel is compared with Armco Pure Iron by computing the configuration 4 magnetic circuit in COMSOL with the respective material and checking the difference in output torque. The lowest magnetic permeability value of AISI430, and highest magnetic permeability value of ARMCO Pure Iron are taken to see what would be the maximum difference in performance. The computation showed that output torque of ARMCO Pure Iron is only 17.5% higher than with AISI430. It is decided, that such magnitude difference of output torque is not significant enough to sacrifice manufacturability, therefore, AISI430 will be used as the yoke material. The difference in magnetic field density can be observed in figure 4.5.

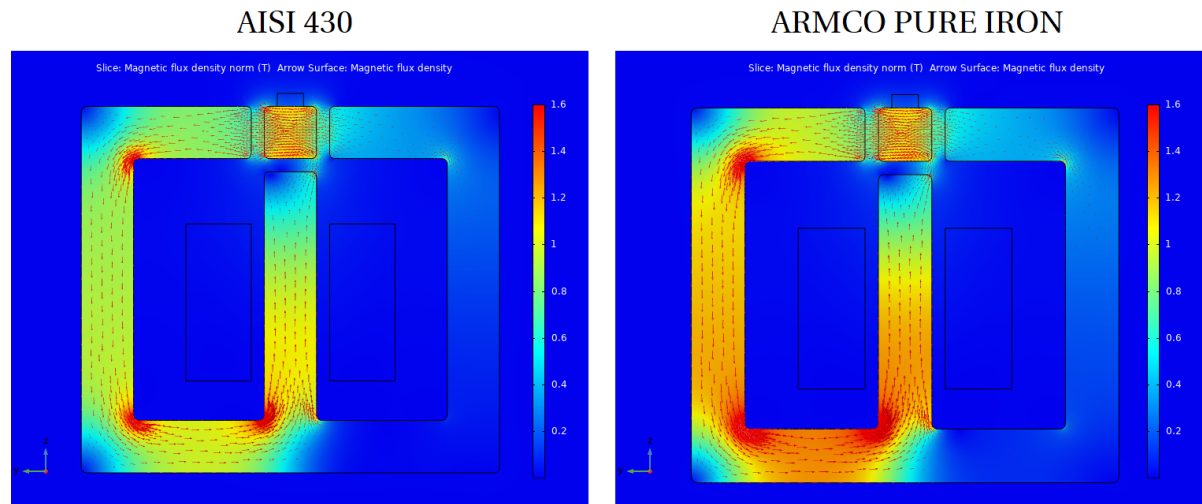


Figure 4.5: Comparison of magnetic flux density of circuit configuration 4 with yoke material AISI430 and ARMCO, when the air gap size is  $t = 0.5$  mm and the magnet is a 2 mm cube.

#### 4.2.5. Magnet selection

Magnet selection is firstly limited to COTS components, because at low volume production a custom magnet design would not be sustainable. Several magnet materials are available such as neodymium, ferrite, samarium, alnico. As a COTS component, the most popular material is neodymium, which has the highest energy density, can be manufactured in various different shapes and is reasonably priced. The main supplier of neodymium magnets in Europe is *Supermagnete*. The shape and dimensions of the magnet determine the magnet's MMF and reluctance. It is important to realise that the magnet has a magnetic permeability same as vacuum therefore a bigger magnet might not always result in better performance. The dimensions of the magnet also determine the total inertia of the scanner, therefore, the ratio of the actuators torque with respect to inertia needs to be kept as high as possible, as explained in chapter 3.2. A critical physical property of a magnet is maximum operating temperature. For neodymium magnets this temperature is relatively low when compared to alnico or samarium magnets. Table 4.5 showcases common neodymium magnet grades and their magnetic properties.

Neodymium grade	Remnant magnetic flux density [T]	Coercive field strength [kA/m]	Max operational temperature[°C]
N45	1,32-1,37	10,8-12,5	≤80
N48	1,37-1,42	10.8-12.5	≤80
N50	1,40-1,46	10.8-12.5	≤80
N52	1,42-1,47	10,8-12,5	≤65
44H	1.32-1.36	10.8-13	≤120

Table 4.5: Magnetic properties of common neodymium grades

It is important to note, that the maximum temperatures in table 4.5 are for "ideal" shape magnets. Very flat or thin magnets can already experience demagnetization effects at lower temperatures. This temperature is usually stated for each separate magnet model, however, it only is true when the magnet is not part of a magnetic circuit. This can be best understood by investigating the B-H curve of the neodymium grades, which are depicted in figure 4.6.

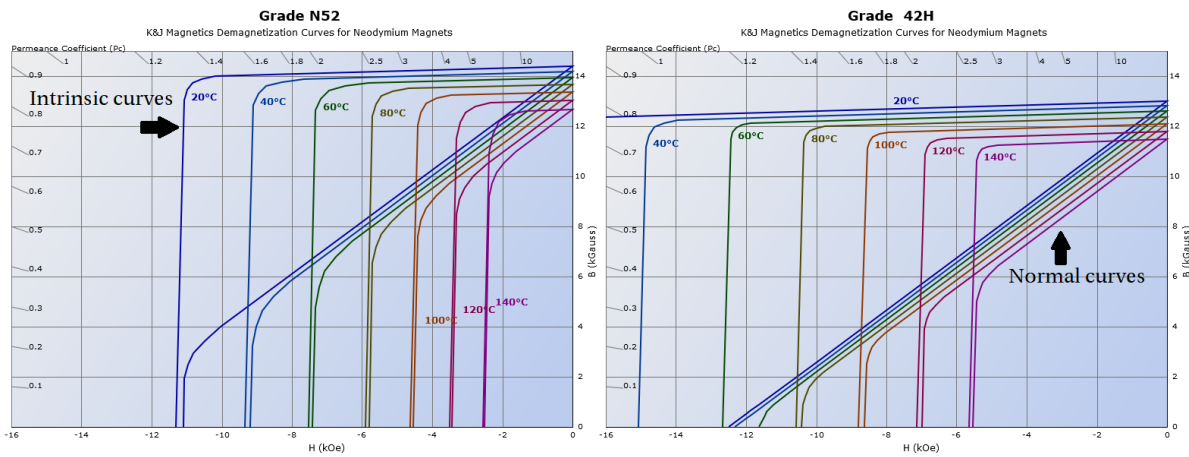


Figure 4.6: Demagnetisation curves of neodymium grades N52 and 42H [3]

The normal B-H curves showcase, that the point at which the material starts to irreversibly demagnetize depends not only on temperature, but on the demagnetizing field acting on the magnet. There are two periods when the scanner can experience significant temperatures: during transportation and during curing of the glue, which bonds the magnet to the flexure. During transportation the temperatures are expected to be below 55 °C. Similar temperatures can be reached during curing of high performance adhesives, as increased temperatures are used to reduce the curing time from a few days to a few hours. To be able to sustain such temperatures without demagnetization the grade H neodymium magnets must be used. When the grade of the magnet is determined, the commercially available magnet range narrows down significantly. Because it is desired to have the same magnetic circuit with the same components for both LF and HF scanners, the magnet size has to be such, that it would be suitable for both actuators. Therefore, a critical dimension limiting the magnet size is scanner mirror width. The width of the mirrors for HF and LF mirrors are 7 mm and 4 mm, therefore, the value of 7 mm is taken as the maximum value for magnet length. Table 4.6 depicts H grade magnets which are of relevant size:

Magnet model	Dimensions [mm]
Q-05-2.5-1.5-HN	5 x 2.5 x 1.5
Q-05-2.5-02-HN	5 x 2.5 x 2
Q-05-05-01-HN	5 x 5 x 1
Q-06-04-02-HN	6 x 4 x 2
Q-06-05-02-HN	6 x 5 x 2

Table 4.6: Available 44H grade magnets of relevant dimensions of *Supermagnete*

It is important to have a high ratio of torque to inertia, as explained in section 3.2. Therefore, this ratio is the main criteria when selecting a specific magnet. However, from a magnetic circuit design point of view, the output torque is also dependant on air gap size, therefore, the torque-inertia ratio needs to be evaluated with respect to the gap size. The inertia of the magnet is estimated by assuming flexure thickness of 0.5 mm. The torque of each magnet is evaluated at different air gap sizes, and then the torque to inertia ratio is estimated. The magnetic circuit parameters are assumed the same, as in section 4.2.1. The computed results are illustrated in figure 4.7.

The plot shows that the smallest available magnets have the largest torque/inertia ratio. At a small air gap size, the ratio becomes almost equal for magnets 1.5x2x5 and 2x2.5x5, but with a larger air gap the ratio of the later magnet becomes slightly higher. Because the ratio is relatively similar of both magnets, it is more favourable to choose the bigger magnet, as with a larger inertia it is easier to design the flexure, because the required stiffness will also be higher, making the dimensions of the flexure larger and more easily manufacturable. Therefore, magnet 2x2.5x5 is selected and is used for both scanner configurations.



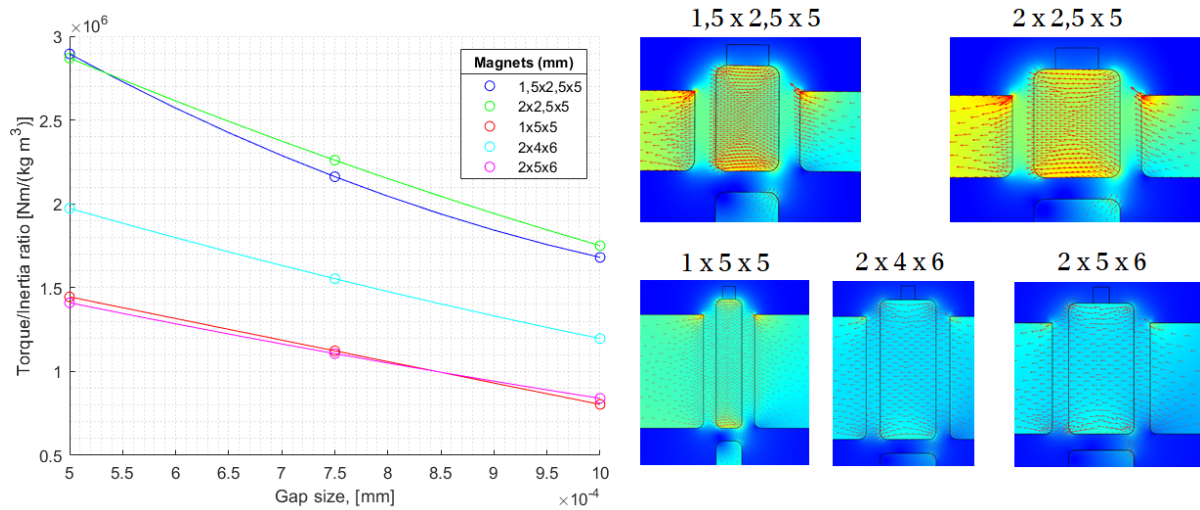


Figure 4.7: 44H grade magnet torque/inertia ratio comparison with respect to the air gap size

With the magnets selected, the only variable that needs to be known in order to determine the rotational inertia of the scanner, is the flexure thickness. For further study, it is necessary to have approximate values for inertia. Therefore, the HF and LF scanner inertia with respect to flexure thickness is estimated and displayed in figure 4.8. The estimation is based on inertia formulation of appendix D. The inertia of the torsion beam is disregarded, as it is in close proximity to the axis of rotation and therefore does not significantly contribute to the total inertia of the scanner. The considered geometry for the estimation of inertia is showcased in the right side of figure 4.8.

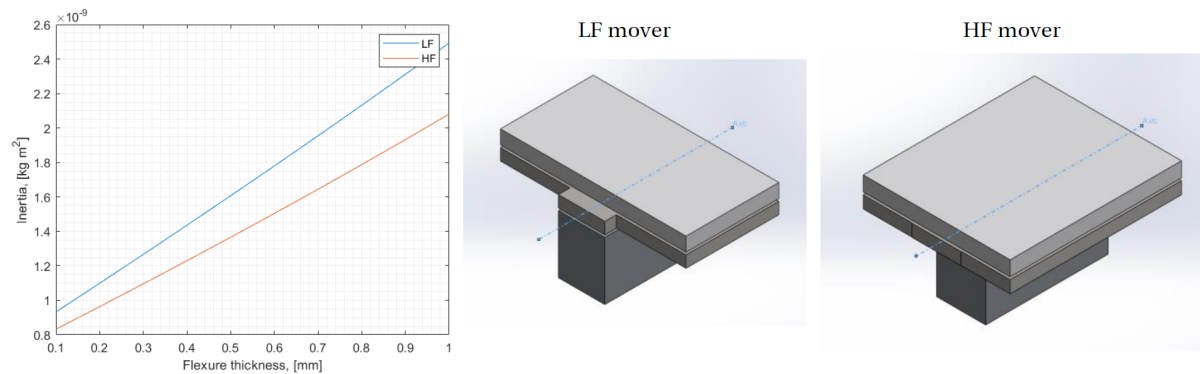


Figure 4.8: HF and LF scanner mover inertia with respect to flexure thickness

#### 4.2.6. Side air gaps and cross section sizing

It can be observed from figure 4.7, that a smaller air gap can lead to better performance, due to an increased output torque. The main limitation on how small the side air gap can be, is the required clearance. Clearance is determined by the maximum rotation angle, the height of the magnet, and the thickness of the flexure. Because the thickness of the flexure is still unknown, it is assumed that it is equal to 0.5 mm. The required clearance for each of the configurations is showcased in figure 4.9.

Scanner	HF	LF
Clearance	8,25 $\mu\text{m}$	358 $\mu\text{m}$

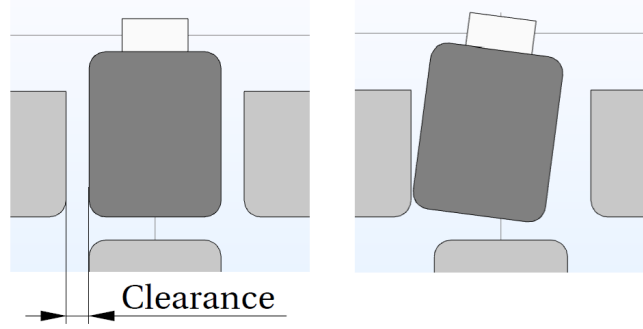


Figure 4.9: Magnet clearance values for HF and LF scanner

Another important factor that can limit performance, is thin air gap damping or otherwise known as squeeze film damping. It is very important for the HF scanner to have a high resonance quality factor, therefore, not accounting for squeeze film damping may limit scanner performance. A simple method of calculating the damping of a torsional mover is described by equations [35]:

$$G_{m,n} = \frac{\pi^6 (mn)^2}{760R_0} \left( m^2 \frac{w}{l} + n^2 \frac{l}{w} \right) \quad C_{m,n} = \frac{\pi^4 (mn)^2}{64k_0} \quad R_0 = \frac{l^2 w^2 \eta}{Q_{pr} h^3} \quad (4.2)$$

$$k_0 = \frac{l w P_A}{h} \quad Z_t = \sum_{m=2,4,\dots,n=1,3,\dots}^{\infty,\infty} \frac{1}{G_{m,n} + j\omega C_{m,n}} \quad c_d = \text{Re}(Z_t) \quad (4.3)$$

where:

$Z_t$  = mechanical impedance [Nm · rad/s]

$c_d$  = damping [Nm · rad/s]

$h$  = the gap height [m]

$l$  = rotating body length [m]

$w$  = rotating body width [m]

$\omega$  = oscillation frequency [rad/s]

$\eta$  = dynamic viscosity [Pa · s]

$P_A$  = static pressure (ambient) [Pa]

$Q_{pr}$  = relative flow rate coefficient [-]

There are two sources of potentially high damping in the scanner: gap between the mirror and the yoke and the gap between the flexure and the yoke. Both of the damping sources are visualized on the left side of figure 4.10. Both of these sources need to be evaluated, however, it is difficult to do so accurately, as the analytical expression is suited for a simple configuration, as showcased on the left side of figure 4.10. The damping source 1 dimension  $w_1$  is selected to be same as of the HF mirror width  $w_1 = 7\text{mm}$  (figure 1.7). The  $l_1$  dimension is not selected to be the same as the HF scanner length due to the magnet taking up space, thus, reducing the surface of damping source 1. Therefore, the  $l_1$  dimension is reduced to  $l_1 = 4\text{mm}$ . The damping source 2 dimension  $w_2$  is selected to be same as the magnet width  $w_2 = 5\text{mm}$ . Because the surfaces of damping source 2 are not on the same plane, it is difficult to select an appropriate dimension  $l_2$ . However, due to the symmetry of both surfaces with respect to the axis of rotation, a fair assumption would be  $l_2 = 5\text{mm}$ , which is double the magnet size. To evaluate the effect of the damping by means of damping ratio, values of inertia and stiffness of the scanner need to be assumed. Flexure thickness is assumed to be 0.5 mm, therefore,  $I_{HF} = 1.35 \times 10^{-9} \text{kg} \cdot \text{m}^2$ . Flexure stiffness is assumed to be  $k_{HF} = 1.15 \text{Nm/rad}$ , so that the resultant resonance frequency is 4650 Hz. Actuator torque values at different gap sizes were estimated in section 4.2.5. Since the torque was estimated assuming an input current of 0.25 A, the torque is reduced proportionally to correlate to a 40 mA input, which can be provided by the electronics. With such assumptions the required damping ratio can be estimated from equation 3.1. The damping values are computed by varying the air gap size and are displayed in figure 4.11.

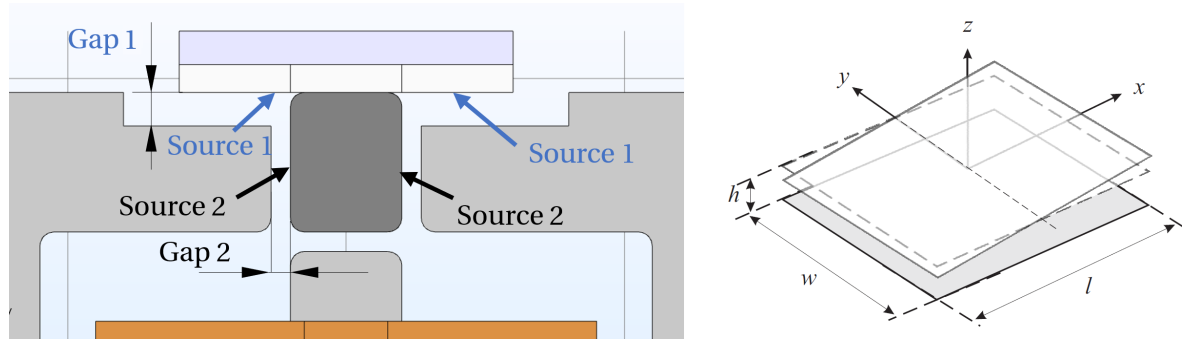


Figure 4.10: Left: Scanner yoke geometry with visualised sources of damping. Right: Topology of a torsional squeeze-film damper[35]

At a gap size of 0.5 mm the summed damping ratio becomes higher than the required ratio. However, there is quite some uncertainty in the estimated values of the resultant configuration due to the difference between the actual geometry and the analytical model. A more accurate estimation could be reached by using FEM analysis or by conducting practical experiments. Due to limited project time, an approach of manufacturing several models with different gap sizes is chosen. To limit the amount of variables, the gap 1 of damping source 1 is chosen to be  $g_1 = 0.6\text{mm}$ . Gap 1 does not influence the magnetic performance and at this gap size figure 4.11 shows, that the summed damping could not reach the required ratio value. Also at  $g_1 = 0.6\text{mm}$  there is enough clearance for both the LF and HF scanner mirrors. Gap 2 is selected to be tested at values of:  $g_2 = 0.5\text{mm}; 0.75\text{mm}, 1\text{mm}$ . However, optimizing the design for each gap size is a very demanding task. Therefore, the gap size  $g_2 = 0.75\text{mm}$  is selected as the middle value for which other parameters of the design will be based upon.

Additionally, the cross section size of the yoke is selected to be equal to the magnet cross section, in order to avoid saturation of the yoke. The final check, on whether the yoke is not saturated, is conducted in section 4.7.

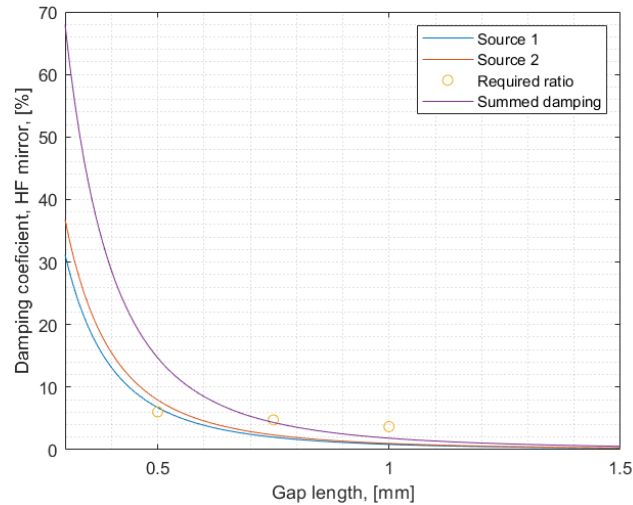


Figure 4.11: Damping ratio of both damping sources evaluated for the HF scanner versus the gap distance

#### 4.2.7. Coil yoke gap sizing

It is uncertain, how much influence the air gap between the yoke of coil has on the damping, because the motion of the magnet surface centre is tangent to the surface itself. Therefore the damping phenomena in this air gap is not equivalent to the situation described in figure 4.10. Therefore, there could be an opportunity to decrease the gap size to improve performance of the scanner. Figure 4.12 showcases the change in torque and force values with respect to the different yoke air gap size values. It can be seen, that the maximum output torque is quite sensitive to the position of the yoke. In addition, the vertical pulling force acting on the magnet increases with decreasing gap size. Depending on how stiff the flexure is, the vertical load acting on

the magnet can cause the flexure to be tensioned and thus, influences its performance. Due to uncertainty of the effect of damping and the vertical force, it is decided to build a prototype in which the coil air gap can be varied to investigate the performance practically. However, similarly as in section 4.2.6 it would be difficult to make an optimal design for various yoke gap positions. To stay conservative, it is selected to design for coil gap size of  $g_c = 0.75$  mm.

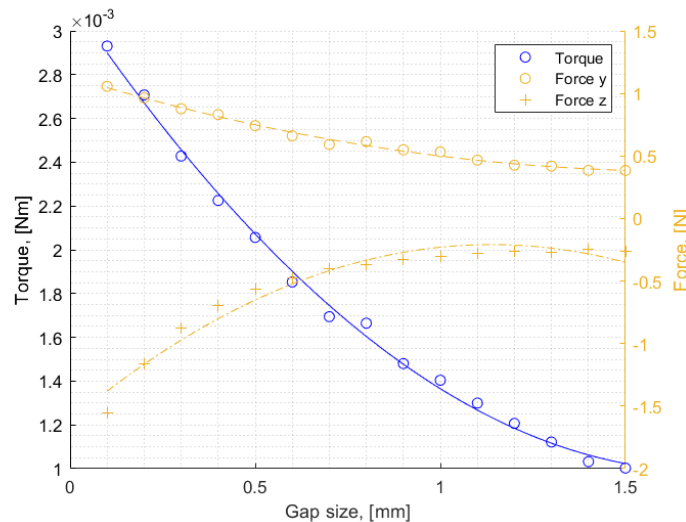


Figure 4.12: Computed torques and forces acting on the scanner with a side gap of 1 mm and a current of 250 mA

#### 4.2.8. Coil design

To keep the cost of HF and LF scanners low, it is desired to have the same coil for both actuators. The coils must have a high magneto motive force to be able to actuate the magnet. The magneto motive force is determined by the current running through the coil and the winding number. The maximum current running through the coil is limited by two factors: the maximum current that the driving electronics can generate and the maximum current density that the wire is able to withstand without experiencing significant thermal heating. Various sources indicate different current density values, at which, no thermal issues occur [12] [28]. The maximum allowable current density in a wire depends on how the wire is packaged, whether it is wounded in a coil or hanging in the air. Usually, values between  $1\text{A}/\text{mm}^2$  and  $10\text{A}/\text{mm}^2$  are regarded as the limits below which, no thermal heating problems occur. Because maximum currents generated by the EasyScan electronics are known (section 1.3), the limiting wire diameters can be determined based on available wire gauges:

AWG	Diameter, [mm]	Cross section, [ $\text{mm}^2$ ]	Current density at 40 mA [ $\text{A}/\text{mm}^2$ ]	Current density at 250 mA [ $\text{A}/\text{mm}^2$ ]
32	0,20	0,032	1,25	7,80
33	0,18	0,025	1,57	9,82
34	0,16	0,020	1,99	12,43
35	0,14	0,016	2,49	15,57
36	0,13	0,013	3,16	19,74

Table 4.7: Current density of various wire gauges

34 gauge wire is selected, even though it exceeds the current density limit of  $10\text{A}/\text{mm}^2$  at 250 mA of current. It will be demonstrated in section 4.3, that the scanner actually does not reach this current value. Next, the winding number needs to be determined. The winding number influences the inductance of the scanner and is proportional to the square of the winding number. The influence of inductance is slightly different for the HF and LF scanner due to the electronics used. As figure 1.8 indicates, the HF scanner is connected to a capacitor. Because the scanner itself is a resistor and an inductor, the series circuit combination of these three elements creates a resonance circuit. The resonance peak can be adjusted by modifying the capacitance

without changing the inductance, therefore, the impedance at the operating frequency can be optimized. As a result, inductance is not a significant factor for the HF scanner.

For the LF scanner the combination of the coil resistance and inductance create a low pas filter. Therefore, if the inductance becomes significantly large, the coil will not be able to produce rapid changes of the current, which are required in an open loop system. Because the magneto motive force increases the output torque of the scanner and inductance reduces the dynamic response, the challenge of design becomes to maximize the winding number, without having a significant negative effect on the dynamic response.

The winding number is also limited by the available space in the scanner. Therefore, it takes a few iterations before the dimensions of the coil can be determined. With a few tries, it seems that a maximum number of windings, that can still fit to the required space is 500. With the winding number selected, the dynamic electrical behaviour of the coil can be investigated. According to Faraday's law, a voltage, proportional to the rate of change of the magnetic field, is induced in a coil [25]:

$$U = -N \frac{d\phi}{dt} = -\frac{d\lambda(x, I)}{dt} \quad (4.4)$$

where

$x$  = rotation angle [rad]

$I$  = current [A]

$U$  = induced voltage [s]

$\lambda$  = flux linkage [Wb turns]

$t$  = time [s]

$\phi$  = magnetic flux running through the coil [Wb]

$N$  = coil winding number [-]

Because the flux linkage depends on the current and on the position of the mover, the induced voltage is expressed as:

$$U = -\left(\frac{\partial \lambda}{\partial I} \frac{dI}{dt} + \frac{\partial \lambda}{\partial x} \frac{dx}{dt}\right) \quad (4.5)$$

The term  $\frac{\partial \lambda}{\partial I}$  represents the inductance, whereas the term  $\frac{dI}{dt}$  represents the rate of change of the current. The term  $\frac{\partial \lambda}{\partial x}$  represent the EMF coefficient, whereas the term  $\frac{dx}{dt}$  represents the angular velocity. The values of the flux linkage at different rotation and current settings can be computed from the FEA model. The flux linkage distribution visually seems linear, as showcased in figure 4.13.

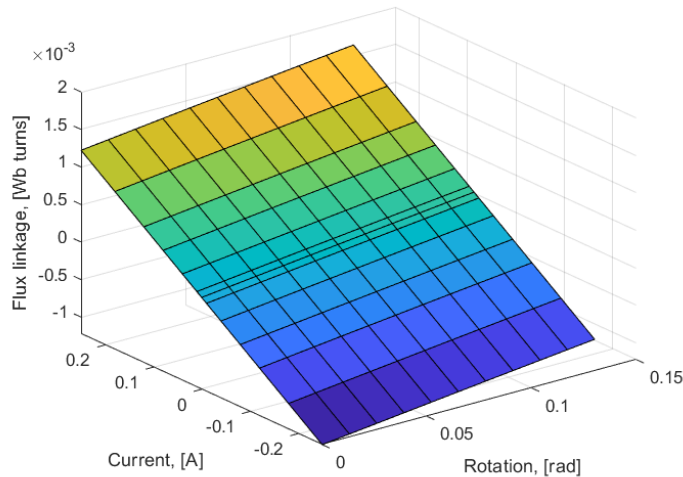


Figure 4.13: Flux linkage distribution with respect to excitation current and to mover rotation.

Therefore, a surface can be easily fitted through the selected data. A second order polynomial fit was used and the computed coefficients are displayed in table 4.8.

Polynomial	$\lambda(x, I) = p_{00} + p_{10}x + p_{01}I + p_{20}x^2 + p_{11}xI + p_{02}I^2$					
Coefficients	$p_{00}$ $-3.716 \times 10^{-7}$	$p_{10}$ $3.365 \times 10^{-3}$	$p_{01}$ $4.89 \times 10^{-3}$	$p_{20}$ $-9.198 \times 10^{-4}$	$p_{11}$ $-3.716 \times 10^{-7}$	$p_{02}$ $-2.609 \times 10^{-7}$

Table 4.8: Polynomial fit values for the flux linkage distribution

Taking the partial derivative  $\frac{\partial \lambda}{\partial i}$  yields:

$$L = \frac{\partial \lambda}{\partial i} = p_{01} + p_{11}x + 2p_{02}I \approx 4.89 \times 10^{-3} \text{ mH} \quad (4.6)$$

Terms  $p_{11}$  and  $p_{02}$  do not contribute significantly to the inductance, which means that the inductance of the coil is independent of the current  $I$  and rotation  $x$ . Taking the partial derivative  $\frac{\partial \lambda}{\partial x}$  yields:

$$k_{\omega} = \frac{\partial \lambda}{\partial x} = p_{10} + p_{11}I + 2p_{20}x \approx p_{10} + 2p_{20}x \quad (4.7)$$

Because, the contribution of  $p_{11}$  is insignificant, the angular velocity coefficient is only dependant upon the position of the mover. With the inductance of the coil and the EMF coefficient of the device known, it is possible to model the electrical dynamics of the actuator. Modelling of the LF and HF scanner dynamics is conducted in sections 4.3 and 4.4.

In addition, an important parameter of a coil is the time constant, which is described by equation 3.3. The time constant of the designed coil is  $\tau_{coil} = 0.45$ ms. This is the time required for the output to reach 63.2 % of the input, when a step signal was applied. After a time period equal to 5 time constants, the output achieves 99.3 % of the input value, and in some literature is assumed as the value at which the output reached a steady state. The  $5\tau$  time parameter can help characterise the system response frequency. For the designed coil, the frequency at which the coil can still output the full input signal is  $f_{5\tau} = 444.9$  Hz. This characteristic is important for the LF scanner, where fast changes in voltage may be required. The LF scanner dynamics are discussed in section 4.3. The designed coil parameters are listed in table 4.9.

Wire diameter $d_w$	0.15 mm
Winding number $N$	500
Inductance $L$	4.9 mH
Resistance $R$	10.9 $\Omega$
EMF constant $k_{\omega}$	$3.365 - x \cdot 1.940$ mV s/rad
Electrical time constant $\tau$	0.45 ms

Table 4.9: Current density of various wire gauges

#### 4.2.9. Torque constant and magnetic stiffness

Because, characteristics of the air gap sizes, the coil, and the magnet are known, the torque output of the scanner can be determined. This is done by computing the output torque at different rotation and input current settings. The rotation is varied between values of 0 and 130mrad. The excitation current is varied from  $-250$  mA to  $250$  mA. The computed torque plot is displayed in figure 4.14:

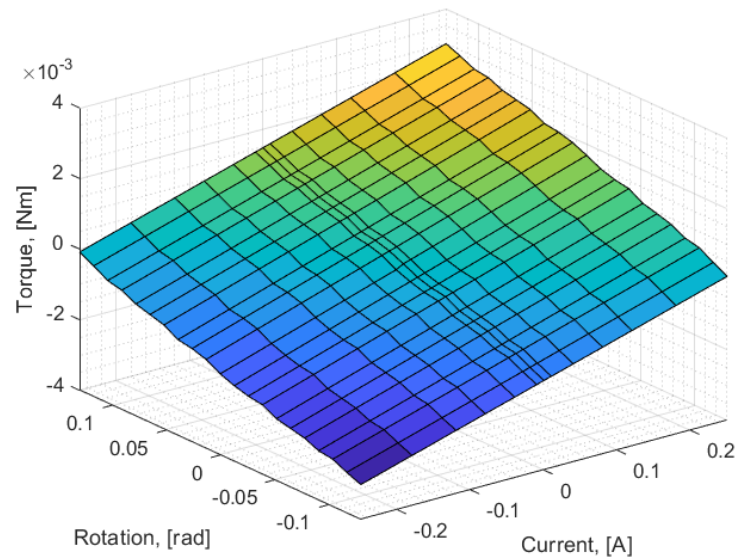


Figure 4.14: Actuator torque distribution with respect to actuation current and rotation angle

At first glance, the torque distribution seems relatively flat. However, upon closer inspection it can be seen that the distribution is slightly curved. Furthermore, fluctuations can be noticed between neighbouring torque values. This is because the Maxwell stress tensor is very sensitive to mesh size, which leads to computation errors. A finer mesh would be required to minimize the errors and make the plot smooth. However, with the showcased accuracy it already took 13 hours to compute the torque values. Therefore, it was decided that the resultant accuracy is sufficient.

The computed distribution can be approximated by a polynomial, to develop a mathematical expression of the output torque, which can then be used to model the dynamics of the actuator. Due to the maximum and minimum torque values residing on the plot locations, which are curved in the opposite directions, it was decided to use a third order polynomial, to approximate the actuator torque. The computed polynomial coefficients are displayed in figure 4.10.

Polynomial	$T(x, I) = p_{00} + p_{10}I + p_{01}x + p_{20}I^2 + p_{11}xI + p_{02}x^2 + p_{30}I^3 + p_{21}I^2x + p_{12}Ix^2 + p_{03}x^3$				
Coefficients	$p_{00}$	$p_{10}$	$p_{01}$	$p_{20}$	$p_{11}$
	$-1.1 \times 10^{-6}$	$6.679 \times 10^{-3}$	$1.039 \times 10^{-2}$	$-3.155 \times 10^{-6}$	$-2.803 \times 10^{-18}$
	$p_{02}$	$p_{30}$	$p_{21}$	$p_{12}$	$p_{03}$
	$1.041 \times 10^{-4}$	$-1.357 \times 10^{-4}$	$-1.538 \times 10^{-5}$	$-2.996 \times 10^{-2}$	$3.743 \times 10^{-2}$

Table 4.10: Polynomial approximation of the actuation torque with respect to rotation and current

Taking the partial derivative of the torque distribution with respect to current  $\frac{\partial T(x, I)}{\partial I}$ , yields the actuator constant. Taking the partial derivative of the torque distribution with respect to rotation  $\frac{\partial T(x, I)}{\partial x}$ , yields the magnetic stiffness of the actuator. Actuator constant and magnetic stiffness distributions are displayed in figure 4.15.

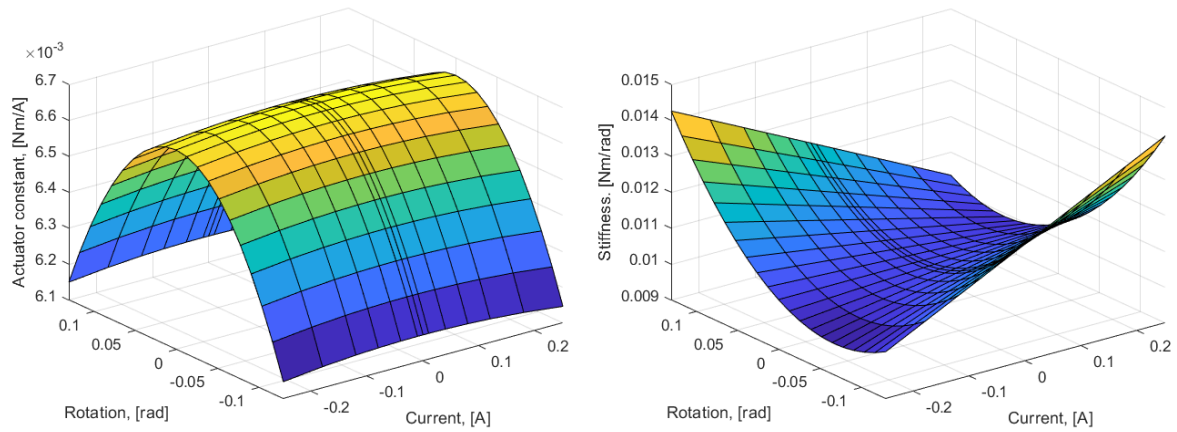


Figure 4.15: Left: Actuator constant distribution with respect to current and rotation. Right: Negative magnetic stiffness distribution with respect to current and rotation.

Both distributions are non linear with respect to current and rotation. The actuator constant can be considered linear with respect to current, as it varies only by 0.1 %. However, with respect to rotation the actuator constant varies up to 8.6 %.

The magnetic stiffness is non linear with respect to rotation and current. The stiffness values vary up to 37.2 % at the boundaries of the computed variable field. With the magnetic stiffness and actuator constant determined, the required mechanical stiffness of each scanner can be determined.

#### 4.2.10. Magnetic forces

The magnetic forces acting on the magnet are illustrated in figure 4.16. Similarly to section 4.2.9, fluctuations can be noticed between neighbouring data points, which is a result of the Maxwell stress tensor sensitivity to mesh size. However, due to high computational costs it was decided that the accuracy of the data is sufficient.

The lateral (Y axis) magnetic force plot resembles the magnetic torque distribution, because the lateral force is the main contributor to the total torque acting on the scanner. Additionally, the vertical force (Z axis) plot illustrates that there is almost no vertical force change at a rotation of 0 mrad, when the input current is varied from 0 mA to 250 mA, as the change in force is only 0.03 %. Therefore, the force in the Z direction can be considered static during the operation of the HF scanner because it rotates only by 3 mrad.

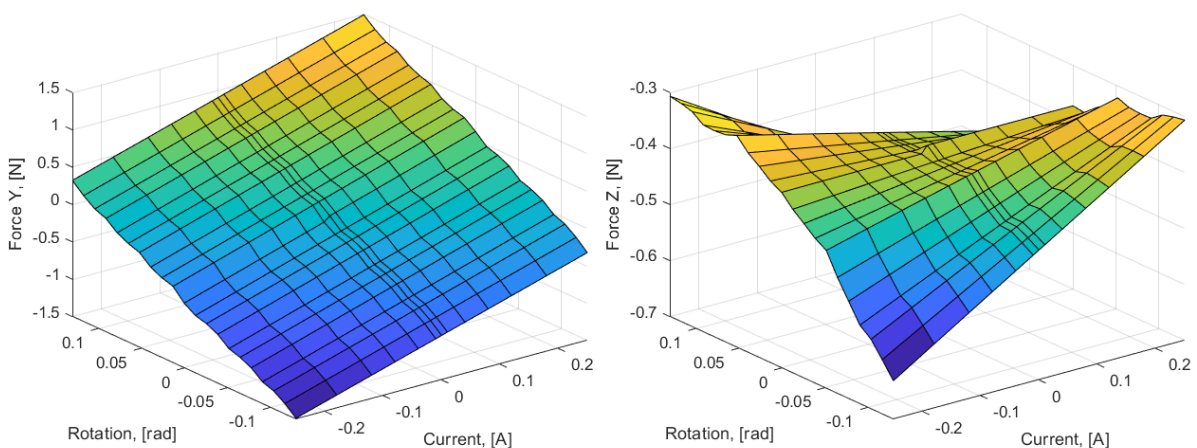


Figure 4.16: Distribution of the magnetic forces acting on the magnet

### 4.3. LF flexure stiffness and scanner dynamics

In section 1.8 it was discussed that the currently used scan motion for the LF scanner is sawtooth. Theoretically, the scan motion could also be triangular, which requires less torque to actuate, as the image is scanned



both on the front and the back stroke of the scanner. However, scanning systems are not always capable to execute equivalent front and back scans. To take the worst case scenario into account, the scan motion of sawtooth is considered as the target scan motion for the LF scanner.

A preliminary estimation of the scan profile which has two distinct angular acceleration  $\alpha$  phases is considered:

- Constant scan speed during front scan.
- Rapid deceleration and acceleration to return towards start position during back scan. The trajectory of this part is derived from a 5th order polynomial. The 5th order trajectory is selected because it has a smooth acceleration profile. A smooth acceleration is important to have, as it will result in a smooth input voltage, therefore, the induced voltage from the coil will be reduced. In addition, due to the smooth motion, smaller vibrations will be excited in the system.

The resultant scan motion is displayed in figure 4.17. The scan motion considered has a P-P rotation angle of 226.4 rad, but is offset to reach the angle of 130.5 rad. This is done in order to assess the maximum setting required, to actuate the scanner towards the amplitude limit, where the most amount of torque is needed.

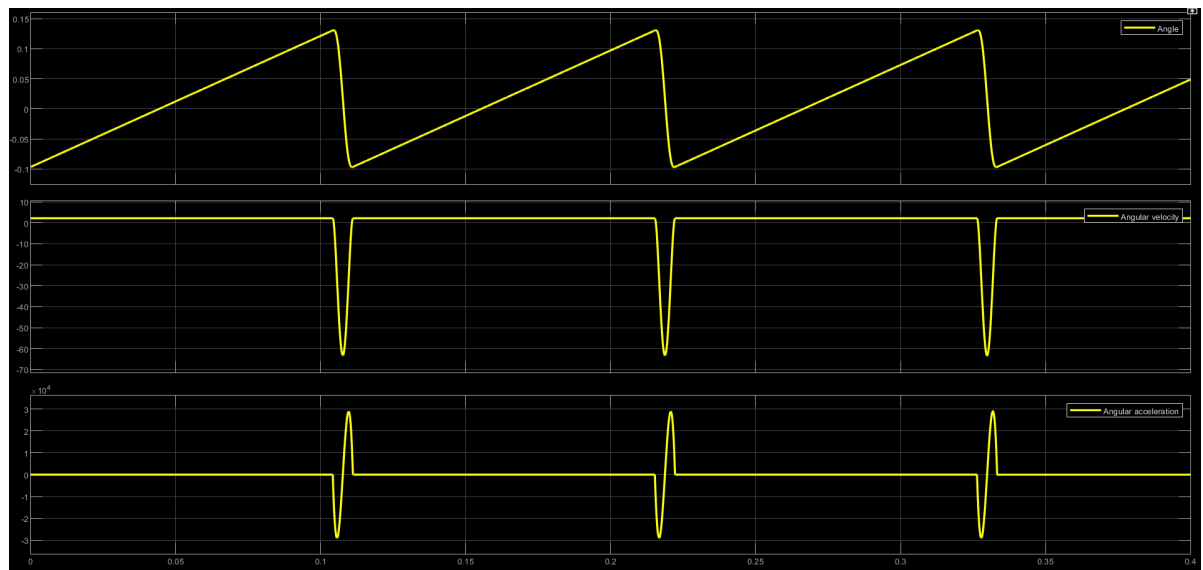


Figure 4.17: Desired LF scanner trajectory, velocity and acceleration plots

If the LF scanner had zero stiffness, then the applied torque  $T_I$  would have the same distribution as the angular acceleration showcased in figure 4.17. Because the scanner is mounted on a flexure, it will not have zero stiffness and additional torque will be needed to offset the spring and damping forces in order to achieve the desired trajectory. As an initial evaluation, no magnetic stiffness is assumed to be acting on the scanner. Then the required torque is:

$$I\ddot{\theta} + b\dot{\theta} + k_{LF}\theta = T = T_I + T_k + T_c \quad T_k = k_{LF}\theta \quad T_c = b\dot{\theta} \quad (4.8)$$

where

$T_I$  = actuator torque if the LF scanner had zero stiffness [Nm]

$T_k$  = actuator torque required to offset the spring force [Nm]

$T_c$  = actuator torque required to offset the damper force [Nm]

$b$  = damping coefficient [Nms/rad]

$k_{LF}$  = LF flexure stiffness [Nm/rad]

$\ddot{\theta}$  = angular acceleration [rad/s<sup>2</sup>]

$\dot{\theta}$  = angular velocity [rad/s]

$\theta$  = rotation angle [rad]

Because the desired rotation angle and angular velocity at each time instance is known, the required torque  $T_k$  and  $T_c$  can be determined. Assuming the LF scanner inertia of  $I_{LF} = 1 \times 10^{-9}$  kgm<sup>2</sup>, spring stiffness

of  $k_{LF} = 1.42 \times 10^{-2}$  Nm/rad (which is the maximum magnetic stiffness), a damping ratio of  $\zeta = 5\%$ , results in a resonance frequency of 600 Hz of the flexure. The required torque is depicted in figure 4.18. Because the scanner inertia is relatively small, almost all of the torque is used for offsetting the spring torque, the torque plot in figure 4.18 and the angular position in figure 4.17 have the same form.

However, due to the physical phenomena of the reluctance actuator, there is also a negative magnetic stiffness present. The electrical dynamics of the coil also play a role, because as there is an induced voltage due to the change of current and to the motion of the magnetic mover, as described in equation 4.5. Therefore, all of these factors need to be taken into account, in order to determine optimal flexure stiffness  $k_{LF}$  and the required torque. Moreover, it is even more important to know the required input signal of the electronics to determine whether they are capable of driving the load.

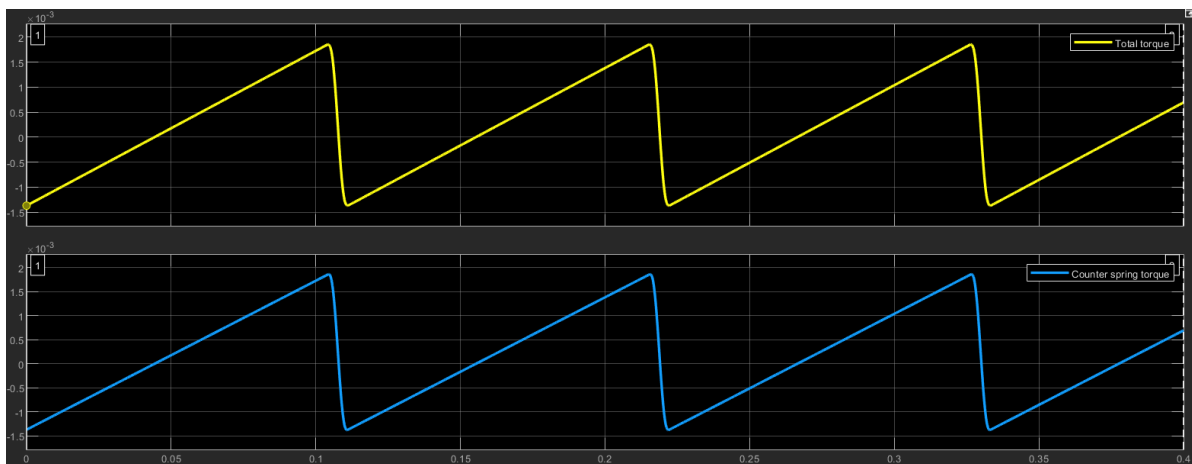


Figure 4.18: Torque required to actuate the LF scanner in sawtooth motion. The total torque and spring torque are showcased separately

Due to the non-linear behaviour of the magnetic stiffness and the output torque, it is difficult to estimate scanner behaviour. Linearising the behaviour may not be optimal, as the magnetic stiffness varies up to 37.2% in the working range of the scanner. To simplify the design process, *Simscape* is used to model the system. The LF scanner, modelled as a 1 DOF system, is displayed in figure 4.19.

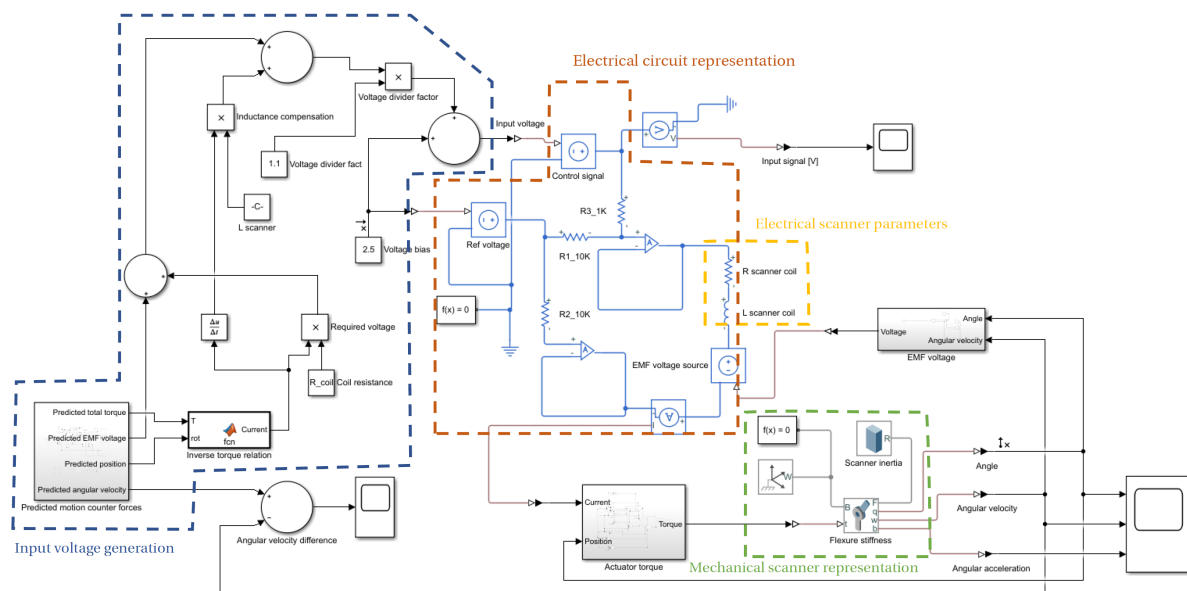


Figure 4.19: LF scanner modelled with *Simscape*

The electric and mechanical behaviour of the LF scanner is modelled. The electric circuitry is based on currently used EasyScan electronics, illustrated in 1.9. The input voltage is feed to the electric circuit, where

a current is generated. The current is then feed to the "Actuator torque" block, which is the polynomial form of the torque function  $T(x, I)$ , which was defined in section 4.2.9. Based on the scanner's position  $x$  and the input current  $I$ , the actuator outputs an according torque. The "EMF voltage" block outputs an induced voltage in the coil, based on scanner speed and position, as described by equations 4.13 and 4.7. The induced voltage, due to the change of current in the electric circuit, is inherently modelled in the "L scanner coil" block, which only requires to specify the inductance of the coil. The "Predicted motion" block estimates the required torque based on flexure stiffness  $k_{LF}$ , inertia  $I_{LF}$ , damping ratio  $\zeta$ , and the desired trajectory. The predicted current is feed to the "Inverse torque relation" block, which calculates the current, based on torque and position. The "Inverse torque relation" block takes the torque function  $T(x, I)$  and solves for the current  $I$ . Because the desired velocity at any point in time of the scanner is known, an additional voltage can be generated to counter the voltage induced due to the motion of the scanner. The current at any point in time is also predicted, therefore, an additional input voltage can be generated, to offset the voltage induced by the coil due to induction.

The electric parameters of coil resistance  $R$ , inductance  $L$ , EMF constant  $k_{\omega}$ , have already been determined in section 4.2.8, thus, the performance of the scanner can be evaluated. Similarly as before, values of  $k_{LF} = 1.42 \times 10^{-2} \text{ Nm/rad}$ ,  $\zeta = 5\%$ ,  $I_{LF} = 1 \times 10^{-9} \text{ kgm}^2$  are assumed. The resultant input voltage plot is showcased in figure 4.20.

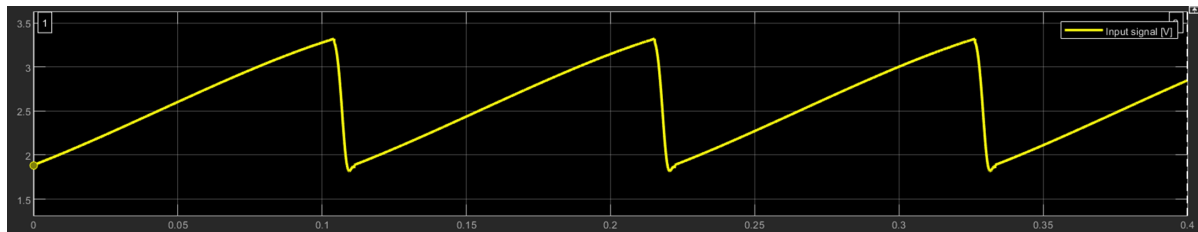


Figure 4.20: Voltage input of the LF scanner when  $I_{LF} = 1 \times 10^{-9} \text{ kgm}^2$ ,  $\zeta = 5\%$ ,  $k_{LF} = 1.42 \times 10^{-2} \text{ Nm/rad}$ ,  $R = 10.9 \Omega$

The plot shows that the a maximum voltage of 3.3 V is needed, which is below the 5 V limit of the currently used electronics. However, the stiffness of the flexure in this configuration is equal to that of the maximum magnetic stiffness. As a result, the scanner becomes marginally stable at the edges of the scan amplitude. To increase reliability of the scanner, the stiffness of the flexure must be increased. Therefore, it is selected, that the stiffness of the flexure must be 20 % higher, which results in a stiffness of  $k_{LF} = 1.70 \times 10^{-2} \text{ Nm/rad}$ . The required voltage to to reach the maximum amplitude is displayed in figure 4.21. The maximum voltage increases to 4.07 V, which is feasible by the electronics.

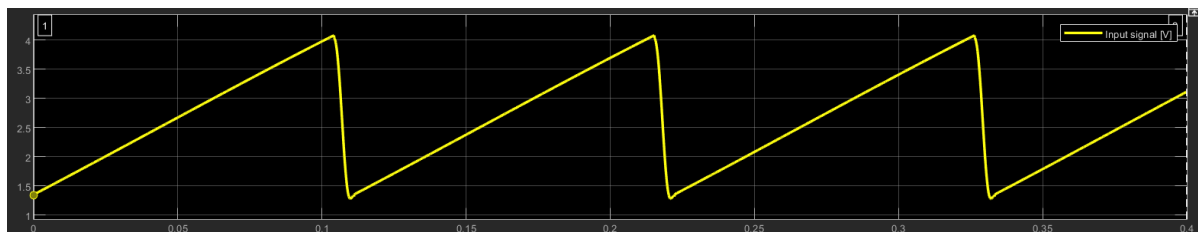


Figure 4.21: Voltage input of the LF scanner when  $I_{LF} = 1 \times 10^{-9} \text{ kgm}^2$ ,  $\zeta = 5\%$ ,  $k_{LF} = 1.70 \times 10^{-2} \text{ Nm/rad}$ ,  $R = 10.9 \Omega$

The scan profile of the system, with flexure stiffness  $k_{LF} = 1.70 \times 10^{-2} \text{ Nm/rad}$ , is showcased in figure 4.22. The LF scanner is actuated from the neutral position, therefore, vibrations are excited. However, they die out on the first scan and the mover reaches it's steady state response. It is clear that the resultant trajectory is the same as the desired trajectory, illustrated in figure 4.17. However, a closer inspection is needed to see the differences. The way to do that is to compare the velocity profile of the predicted trajectory with the actual trajectory. This is done, by subtracting the actual scanner velocity profile from the predicted profile and is illustrated in figure 4.22.

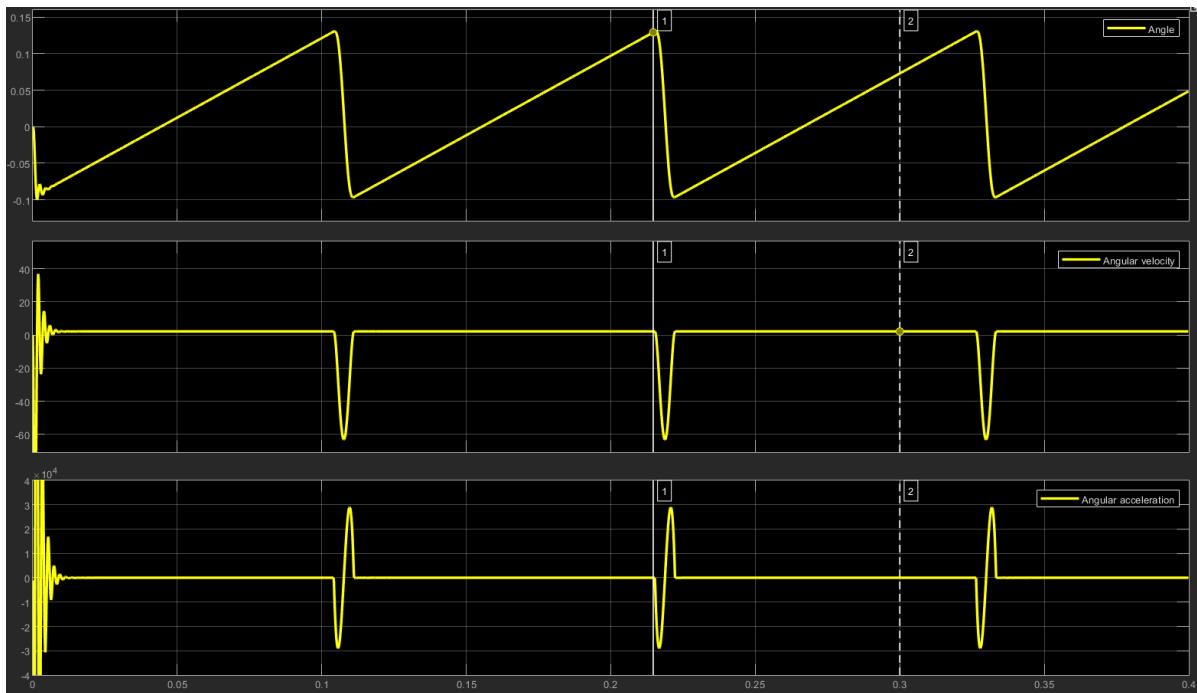


Figure 4.22: Angular position, velocity and acceleration of the LF scanner actuated from a stationary position when  $I_{LF} = 1 \times 10^{-9} \text{ kgm}^2$ ,  $\zeta = 5\%$ ,  $k_{LF} = 1.70 \times 10^{-2} \text{ Nm/rad}$ ,  $R = 10.9 \Omega$

The results show that there is a difference in velocity profiles, which are most noticeable during the back scan trajectory portion. However, the differences in velocity in the back scan portion of the trajectory are not as important as differences in the front scan. When the mover is at the start position of the front scan, there is still a difference in velocity, that is 3 orders of magnitude smaller than the required velocity. Therefore, it can be considered that the scanner is able to achieve the required trajectory.

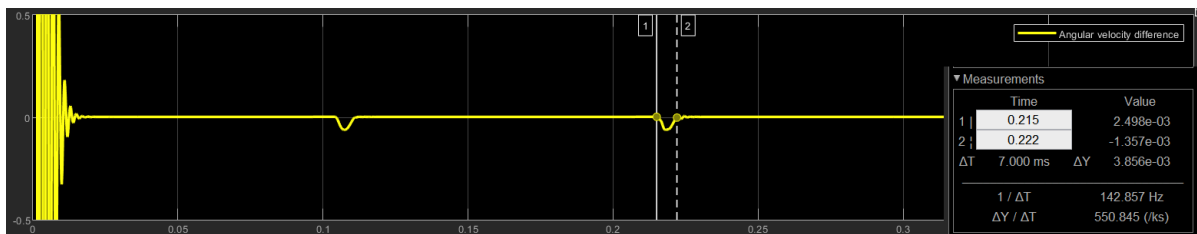


Figure 4.23: Plot of the resultant LF scanner angular velocity vs predicted velocity when  $I_{LF} = 1 \times 10^{-9} \text{ kgm}^2$ ,  $\zeta = 5\%$ ,  $k_{LF} = 1.70 \times 10^{-2} \text{ Nm/rad}$ ,  $R = 10.9 \Omega$

The required current to drive the LF scanner is displayed in figure 4.24. The maximum current reaches the value of 129.9 mA, which equates to  $6.49 \text{ A/mm}^2$  of current density. However, of interest is the RMS current, which is measured to be 69.5 mA, equating to  $3.49 \text{ A/mm}^2$  of current density. This is below the  $10 \text{ A/mm}^2$  limit mentioned in section 4.2.8. As a result, the LF scanner should not experience thermal issues.

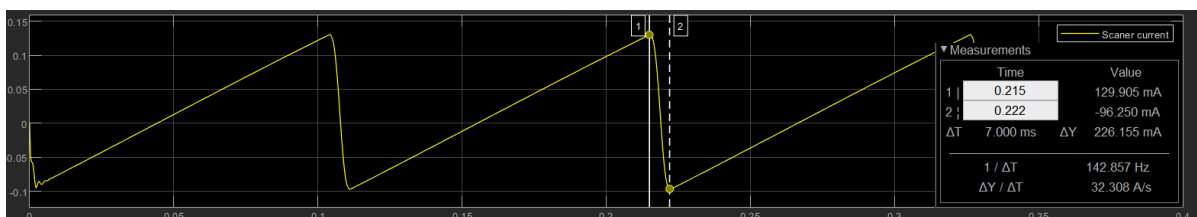


Figure 4.24: LF scanner current when  $I_{LF} = 1 \times 10^{-9} \text{ kgm}^2$ ,  $\zeta = 5\%$ ,  $k_{LF} = 1.70 \times 10^{-2} \text{ Nm/rad}$ ,  $R = 10.9 \Omega$

Finally, it is important to note that the derivation of the required current and voltage are rooted, by knowing the actual values of inertia, stiffness, damping and the magnetic properties of the system. In reality, the mentioned parameters will not be equal to the theoretical ones. Therefore, the problem of predicting the real input shape will occur. This problem can be solved similarly in the way that the current EasyScan software solves it, by generating different input signal shapes until an input signal that makes the scan speed constant is found.

However, the signal shape may not be equal to estimated in figure 4.22 and fast changes, such as displayed in figure 1.9, may be required. If the changes are faster than the five time constant frequency of  $f_{5\tau} = 444.9$  Hz, then the coil will not be able to follow the signal. In that case, some redesign will have to be done to decrease the coil time constant. A simple way to do that would be to add a series resistance to the coil. This will increase the total resistance and reduce the time constant, but due to the increased total resistance, a larger input voltage will be needed to generate the required current. A second option would be to decrease the winding number of the coil, to decrease the inductance. In order to still generate the same amount of MMF, the driving current would have to be increased, resulting in increased requirements for the driving electronics.

#### 4.4. HF flexure stiffness and scanner dynamics

The required flexure stiffness of the HF scanner depends on the magnetic stiffness. The magnetic stiffness varies only by 0.2% in the operational range of the rotation angle and current. Therefore, the magnetic stiffness can be considered to be linear for the HF scanner, with a stiffness value of  $k_{mag} = 1.039 \times 10^{-2}$  Nm/rad. Because the HF scanner needs to operate at its resonance frequency, the derivation of the required flexure stiffness is simple. Considering the scanner a single degree of freedom system, the equation of motion is described as:

$$I\ddot{\theta} + b\dot{\theta} + (k_{HF} - k_{mag})\theta = I\ddot{\theta} + b\dot{\theta} + k_{tot}\theta = T(t) \quad (4.9)$$

where:

$\theta$  = scanner rotation [rad]

$b$  = angular damping [Nm · s/rad]

$k_{HF}$  = flexure stiffness [Nm/rad]

$k_{mag}$  = magnetic stiffness [Nm/rad]

$k_{tot}$  = total stiffness [Nm/rad]

$T_t$  = actuation torque [Nm]

The relation between the total flexure stiffness and the resonance frequency is:

$$k_{tot} = \omega_{HF}^2 I_{HF} \sqrt{1 - \zeta^2} \quad (4.10)$$

The inertia term  $I_{HF}$  is dependant upon the flexure thickness, as showcased in figure 4.8. Assuming the flexure thickness as 0.5 mm and a 5% damping coefficient the resultant total flexure stiffness is  $k_{tot} = 1.152$  Nm/rad. Adding the magnetic stiffness  $k_{mag}$ , the real flexure stiffness equals to  $k_{HF} = 1.162$  Nm/rad, which is only 0.8% different from the total stiffness  $k_{tot}$ . The resonance frequency is proportional to the square root of the stiffness, therefore the required flexure resonance frequency would increase only by 0.4% to 4670 Hz. The stiffness  $k_{HF} = 1.162$  Nm/rad and resonance frequency  $f_{flex} = 4670$  Hz are assumed as the designed targets for the HF flexure.

The total system is modelled in *Simscape*, to determine the electrical and mechanical behaviour of the system. In this model the inertia of the scanner is assumed to be  $I_{HF} = 1.09 \times 10^{-9}$  kgm<sup>2</sup>, which is the value when the flexure thickness is 0.3 mm. The *Simscape* model is displayed in figure 4.25.

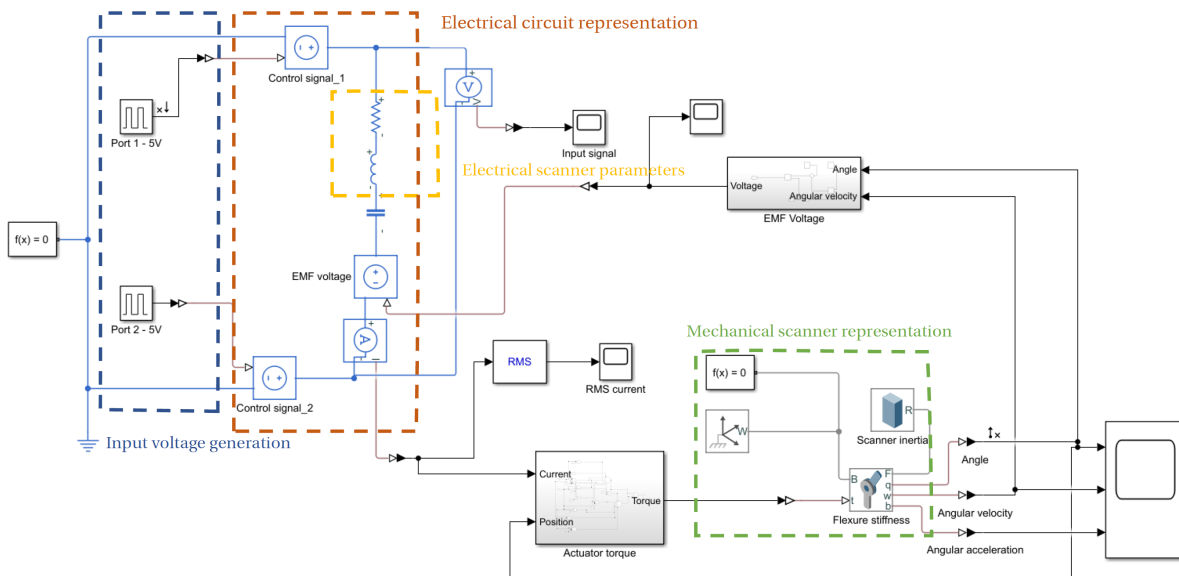


Figure 4.25: Simscape model of the HF scanner

The driving electronics supply a 10 V P-P signal. The resultant scanner rotation angle is illustrated in figure 4.26. The plot shows that the scanner achieves a max rotation of 3.17 mrad, which would mean that the scanner achieves the required amplitude. However, it is important to note, that the stiffness of the flexure is set to a value, so that the resonance frequency of the flexure would be 4670 Hz. It is likely that the real resonance frequency of the flexure will not exactly equal to the required value, therefore, the maximum rotation of the scanner may not be the same.

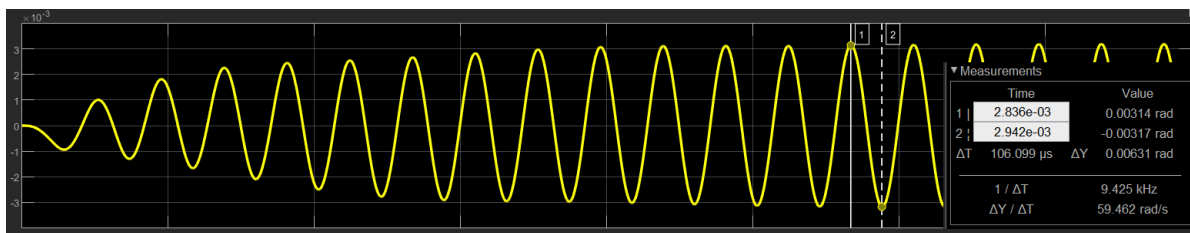


Figure 4.26: The rotation angle of the HF scanner when  $I_{HF} = 1.09 \times 10^{-9} \text{ kgm}^2$ ,  $\zeta = 5\%$ ,  $f_{HF} = 4670 \text{ Hz}$ ,  $R = 10.9 \Omega$

The current driving the load is showcased in figure 4.27. The maximum current is 55 mA which is larger than the maximum current supplied by the electronics. However, the RMS current is only 32 mA, therefore, the currently used electronics will be able to drive the load.

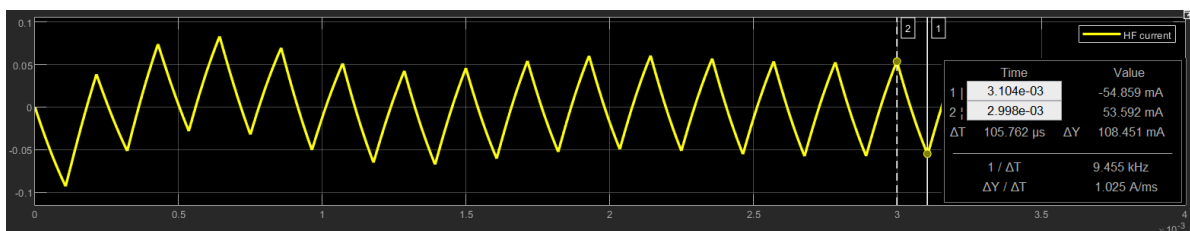


Figure 4.27: Current of the HF scanner when  $I_{HF} = 1.09 \times 10^{-9} \text{ kgm}^2$ ,  $\zeta = 5\%$ ,  $f_{HF} = 4670 \text{ Hz}$ ,  $R = 10.9 \Omega$

An interesting thing to note is that EMF voltage generated due to the motion of the HF scanner has a maximum value of 0.3 V. The plot of the generated EMF voltage is depicted in figure 4.28.

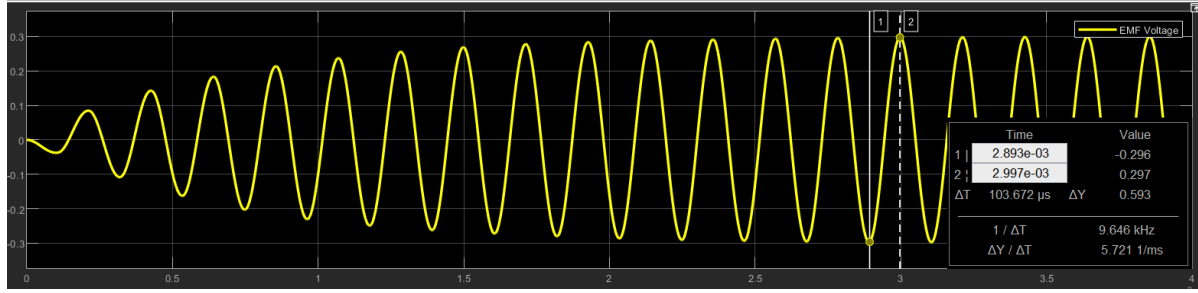


Figure 4.28: Generated EMF voltage of the HF scanner when  $I_{HF} = 1.09 \times 10^{-9} \text{ kgm}^2$ ,  $\zeta = 5\%$ ,  $f_{HF} = 4670 \text{ Hz}$ ,  $R = 10.9 \Omega$

Finally, because the HF scanner dynamics can be linearised, the bode plot of the system can be generated to gain more insight of the system. The bode plot of the scanner is showcased in figure 4.29. The plot shows two peaks. The peak at 720 Hz corresponds to the resonance frequency of the RLC circuit. The second peak at 4670 Hz corresponds to the resonance frequency of the HF scanner. The resonance frequency of the RLC circuit can be manipulated by changing the capacitance. Therefore, if additional magnitude was required, the RLC and the flexure frequencies could be matched. However, that would result with increased current running through the coil, which the electronics have to be able to supply.

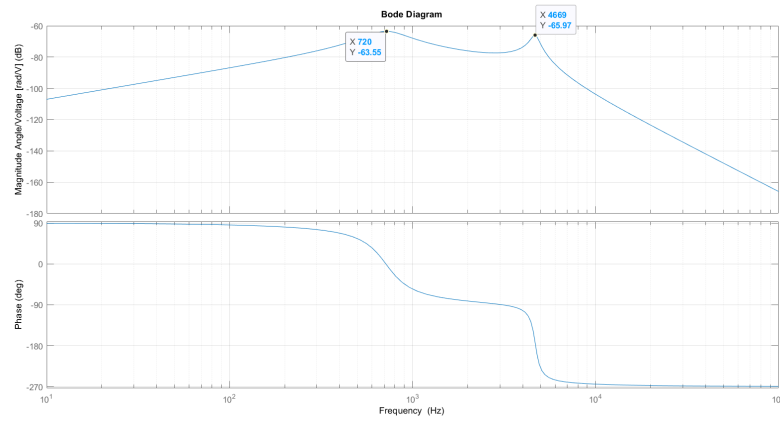


Figure 4.29: Bode plot of the HF scanner, when the input is the voltage, and the output is the rotation angle.

## 4.5. Mechanical design

### 4.5.1. Flexure material selection

The main desired mechanical property for the material is high yield stress, which ensures that deformations can be sustained for many operation cycles. Materials for the flexure of the scanner are fairly limited. This is because the expected thickness of the sheet metal used is between 0.05 mm to 1 mm. Due to such thickness, there are only two materials that are relatively affordable and easily obtainable: stainless steel AISI301 and titanium grade 5. The relevant material properties are displayed in table 4.11. During the design process both materials are taken into consideration as a design variable to see which material is the most suitable for a specific flexure.

Material	Yield stress [MPa]	Young modulus [GPa]	Shear modulus [GPa]	Density [kg/m <sup>3</sup> ]	Available thickness [mm]
AISI301	965	193	75	7780	0.025; 0.04; 0.10; 0.15; 0.20; 0.25; 0.30; 0.40; 0.45 0.50 0.60; 0.70; 0.80; 0.90; 1.00
Titanium grade 5	828	114	44	4420	0.15; 0.20; 0.25; 0.30; 0.40

Table 4.11: Most suitable available flexure materials

### 4.5.2. Machinability considerations

A good design of the flexure cannot be achieved without taking into account machinability factors. Because the flexure can be made out of sheet metal there are several methods on how to manufacture it: laser cutting, water jet, photochemical etching, stamping. Stamping is not suitable due to low yearly manufacturing volume. Laser cutting induces thermal stress on the cutting edge, which can lead to premature failure and drift in flexure stiffness. Photochemical etching is an appealing approach because it has a high accuracy, does not induce stress and is even capable of fabricating 3D features. A water jet does not have the drawback of inducing thermal stress on the cutting edge as a laser, therefore, it is a highly appealing option.

From the mentioned technologies, photochemical etching and water jet cutting seem like the most advantageous. At first glance, it may seem that photochemical etching would offer higher accuracy. However, a quote from a photochemical etching supplier for a preliminary titanium flexure design stated that they can offer only  $\pm 0.050$  mm position tolerance. A microjet cutter can offer the same tolerance without initial photo tooling costs [14]. Therefore, microjet water cutting was selected as the flexure manufacturing technology.

An important point to keep in mind when designing a flexure cut from sheet metal is to keep the dimension of the torsion beam as large and as possible. Design where the width is much smaller than the length of the torsion beam are not optimal because the manufacturing tolerance of  $\pm 0.050$  mm is the same both dimension, therefore, dimensions that are close to the manufacturing tolerance will lead to a spread in flexure stiffness values.

However, at the end of the project after practical tests were already done, the photochemical etching suppliers were contacted again to inquire about the price of stainless steel flexures. As it turned out, stainless steel flexures can be manufactured more cheaply and accurately than flexures made with a micro water jet. The tolerance for a photochemically etched flexure is equal to  $\pm 10\%$  of flexure thickness.

### 4.5.3. Flat torsion beam kinematics

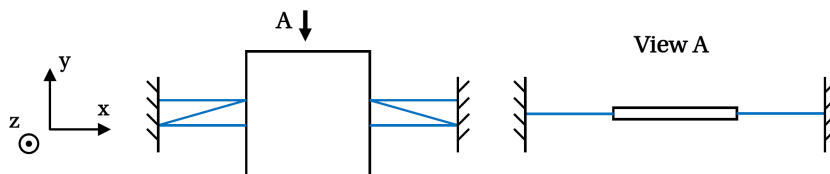


Figure 4.30: Flexure sketch with visualised constraints

The kinematic constraints of the flat torsion beam are illustrated in figure 4.30. The flexure is both under constrained and over constrained. The translations in X and Y directions are constrained twice. Rotation along the the Z axis is also constrained twice. As a result, the flexure has 3 DOF: translation in Z, rotations about X and Y. It is desired to have only the rotation around the X axis to be actuated, therefore, this flexure is under constrained two times, and over constrained 3 times.

### 4.5.4. Flexure geometry design

The geometry of the flat torsion beam selected in section 3.4.2 is defined only by three dimensions: length, width and thickness. The length and width are limited by the available space, their precision is determined the manufacturing process. The thickness of the beam is limited by the available sheet thicknesses, which are displayed in 4.11.

In sections 4.4 and 4.3, the required stiffness was determined for both the LF and HF scanners. Because, there are three variables that determine the stiffness of the torsion beam, many possible solutions exist that yield required stiffness values. Therefore, more restrictions have to be imposed, to determine optimal geometry. For this reason, the flexure also has to have significantly increased higher order mode frequencies and a limited stress value at the maximum rotation of the scanner. A rule of thumb in flexure design is to have the resonance frequency of the higher order modes of not actuated degrees of freedom at least 10 times larger than the first mode frequency. It will be referred to this rule several times in the following sections, therefore, the frequency factor

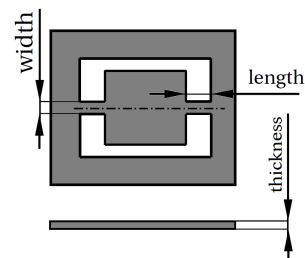


Figure 4.31: HF scanner flexure sketch



$f_{thumb} = 10$  is defined. However, it will be seen in section 4.5.6, that such a requirement is too strict for an under-constrained flexure. The maximum fatigue stress for a material is determined in section 4.5.5.

#### 4.5.5. Fatigue stress

The fatigue limit of mechanism is dependant upon the expected operating cycle number. The EasyScan is expected to operate without failure when used for 50 minutes/day for 5 days/week for 5 years. Assuming 260 workdays/year worldwide results in  $1.81 \times 10^{10}$  oscillation cycles for the HF scanner and  $3.51 \times 10^7$  cycles for the LF scanner. Due to so many oscillation cycles, high cycle fatigue condition can be assumed. Titanium and stainless steel can be considered to have an endurance limit at high cycle fatigue [26]. Endurance limit for steel AISI 301 is  $\sigma_{301} = 552$  MPa [2] and for titanium grade 5  $\sigma_{T5} = 510$  MPa [23]. However, these values are for an unnotched piece of material. To more accurately evaluate the endurance limit for a notched specimen, the method described by Schijve[33] is used. Additional factors such as loading type, stress concentration, and surface roughness have to be evaluated. The flexure is loaded in torsion, therefore, factor of  $S_{L301} = 0,6$  for steel and  $S_{LT5} = 0,48$  for titanium need to be taken into account. It is assumed, that due to water jet cutting, the surface roughness on the flexure will be  $R_a = 5 \mu\text{m}$ , therefore, a factor of  $S_{Ra} = 0,7$  is taken into account. The stress concentration factor due to the radius of the fillet at the base of the beam gives a factor of  $S_{conc} = 0,7$ . Taking into account all the mentioned factors the resultant endurance limit for stainless steel AISI301 is  $\sigma_{301*} = 162$  MPa and for stainless steel  $\sigma_{T5*} = 120$  MPa. These stress values are listed in table 4.12 and will be used as maximum limits for the stresses experienced by the flexure.

Material	Fatigue stress limit
AISI 301	162 MPa
Titanium grade 5	120 MPa

Table 4.12: Maximum fatigue stress of stainless steel and titanium

#### 4.5.6. HF flexure design

The shape of the first mode of the flexure needs to be a rotation around the desired axis of rotation. Because, the inherent design of the flexure is under constrained, it is difficult to keep the higher order modes as far as possible from the first mode. The three unconstrained DOF and their resultant oscillation motions are displayed in figure 4.32. One of the unconstrained DOF is the desired rotation. The next two are the unconstrained translation and the unconstrained rotation. For the sake of clarity in the rest of this thesis the mentioned DOF will be referred to, as depicted in figure 4.32: desired rotation, unconstrained translation, unconstrained rotation.

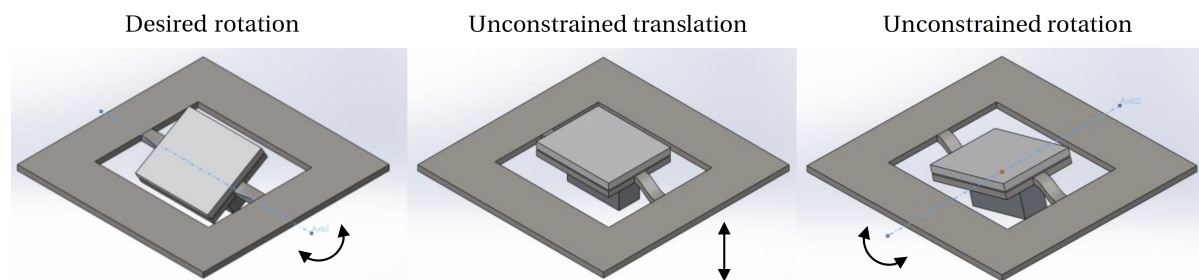


Figure 4.32: Unconstrained DOF of the flexure

The resonance frequency for each of the mode is derived by:

$$f_{DOF} \approx \frac{1}{2\pi} \sqrt{\frac{k_{DOF}}{I_{DOF}}} \quad (4.11)$$

where

$f_{DOF}$  = resonance frequency of the specified DOF [Hz]

$I_{DOF}$  = inertia of the specified DOF [kg or  $\text{kg} \cdot \text{m}^2$ ]

$k_{DOF}$  = stiffness of the specified DOF [N/m or Nm/rad]

The stiffness of each of the unconstrained DOF is derived by using standard formulas of Roark [32]. For the desired rotational DOF, the torsion stiffness of the beam is described as:

$$J_{tor} = ab^3 \left( \frac{16}{3} - 3.36 \frac{b}{a} \left( 1 - \frac{b^4}{12a^4} \right) \right) \quad a = \frac{w}{2} \quad b = \frac{t}{2} \quad b \leq a \quad (4.12)$$

$$k_{tor} = \frac{GJ_{tor}}{l}; \quad k_{tor*} = 2k_{tor}; \quad (4.13)$$

where:

$w$  = torsion beam width [m]

$t$  = torsion beam thickness [m]

$l$  = torsion beam length [m]

$G$  = material shear modulus [MPa]

$J_{tor}$  = beam torsion constant [m<sup>4</sup>]

$k_{tor}$  = torsion stiffness of a single beam [Nm/rad]

$k_{tor*}$  = torsion stiffness of the whole flexure [Nm/rad]

The torsion stiffness  $k_{tor}$  is estimated for a single beam on one side of the mirror. The total torsion stiffness of the flexure  $k_{tor*}$  is double that of  $k_{tor}$  because there is a torsion beam on each side of the mirror.

The unconstrained translational DOF is assumed to be fixed in between two cantilever beams which have the rotation of the "free" end restricted, as showcased in figure 4.33.



Figure 4.33: Fixation sketch of the unconstrained translational DOF

The vertical stiffness for a beam that is fully constrained on one side and has a slope angle restriction on the other is described as:

$$I_{vert} = \frac{wt^3}{12} \quad k_{vert} = \frac{12EI_{vert}}{l^3} \quad k_{vert*} = 2k_{vert} \quad (4.14)$$

where:

$E$  = material Young's modulus [MPa]

$I_{vert}$  = area moment of inertia of the beam [m<sup>4</sup>]

$k_{vert}$  = vertical translation stiffness of a single beam [N/m]

$k_{vert*}$  = vertical translation stiffness of the whole flexure [N/m]

The derivation of the stiffness for the unconstrained rotational DOF is more complicated because standard formulas for such a configuration were not found. The configuration's representation is depicted in figure 4.34.

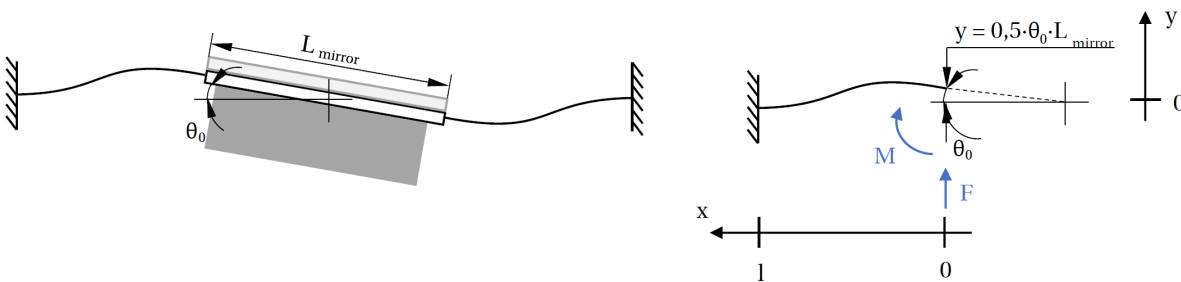


Figure 4.34: Fixation sketch of the unconstrained rotational DOF

To estimate loads acting on the end of the beam, the mirror part is cut off from the beam and an arbitrary force and moment are applied as if they were bending the beam. Then the general differential elastic equation is applied for the beam:

$$EI \frac{d^2 y}{dx^2} = M(x) = Fx - M \quad (4.15)$$

Deriving the elastic equation once with respect to  $x$  yields the slope function  $\theta(x)$ . Deriving the elastic equation twice with respect to  $x$  yields the displacement function  $y(x)$ :

$$\theta(x) = C_1 - \frac{x(2M - Fx)}{2EI} \quad y(x) = C_2 + C_1 x - \frac{x(3Mx - Fx^2)}{6EI} \quad (4.16)$$

The two equations 4.16 have four unknowns:  $C_1, C_2, F, M$ . Four boundary conditions are applied:

$$\theta(0) = \theta_0 \quad \theta(l) = 0 \quad y(0) = \frac{\theta_0 L_{mirror}}{2} \quad y(l) = 0 \quad (4.17)$$

Applying four boundary conditions yields four equations, therefore, the unknowns can be solved for. Of interest are the expressions for the moment  $M$  and force  $F$ :

$$F(0) = \frac{6EI\theta_0(l + 2L_{mirror})}{l^3} \quad M(0) = \frac{2EI\theta_0(2l + 3L_{mirror})}{l^2} \quad (4.18)$$

The force and moment acting on the mover are of equal magnitude but opposite direction than acting on the beam. The total torque acting on the mover from a single beam is:

$$M_{total} = \frac{F(0)L_{mirror}}{2} + M(0) = \frac{3EIL_{mirror}\theta_0(l + 2L_{mirror})}{l^3} + \frac{2EI\theta_0(2l + 3L_{mirror})}{l^2} \quad (4.19)$$

Taking the derivative of the total moment of equation 4.19 with respect to rotation angle  $\theta_0$  yields the stiffness of the mover. The total flexure stiffness  $k_{\theta_0^*}$  for this rotational DOF is twice the stiffness of a single beam:

$$k_{\theta_0} = \frac{dM_{total}}{d\theta_0} = \frac{4EI(l^2 + 3L_{mirror}l + 3L_{mirror}^2)}{l^3} \quad k_{\theta_0^*} = 2k_{\theta_0} \quad (4.20)$$

The constrained DOF are assumed to be sufficient stiffness, therefore, they are not taken into account. The max stress value in the flexure is calculated by assuming a  $\theta_{3mrad} = 3$  mrad rotation of the torsion beam. The stress value is then:

$$\sigma_{max} = \frac{3k_{tor}\theta_{3mrad}}{8ab^2} \left( 1 + 0.6095 \frac{b}{a} + 0.8865 \left( \frac{b}{a} \right)^2 - 1.8023 \left( \frac{b}{a} \right)^3 + 0.9100 \left( \frac{b}{a} \right)^4 \right) \quad b \leq a \quad (4.21)$$

The maximum stress value experienced by the flexure must be lower than the stress values derived in the fatigue analysis section.

The inertia of a specific scanner configuration is determined in the same way as in figure 4.8.

Since there are four design variables that determine the flexure performance ( $w, h, t$  and the material), it does not take significant computational power to calculate the performance of each configuration. Table 4.13 lists the design variable limits. The minimum width and length are selected to be 1 mm in order to have only a  $\pm 5\%$  tolerance of the dimension to keep the design sensitivity low. The maximum beam length is selected to be 2 mm because a longer torsion would simply not fit. The maximum width in theory could be 6 mm long (mirror facet length). However, it will be shown that such long torsion beam widths do not yield feasible results. Therefore, the maximum beam width is set to 3 mm, so that a sufficient amount of results would be computed in order to evaluate the behaviour of the design space.

The characteristics of all the flexures in the design space are computed. Then a data search is done to find configurations, which have the resonance frequency at 4670 Hz with a frequency tolerance of  $\pm 2.5\%$ . The computed design space for both of the AISI301 and titanium grade 5 is displayed in figure 4.35.

Variable	Minimum	Maximum	Step size
w	1 mm	3	0.05 mm
l	1 mm	2	0.05 mm
t	Based on available sheet thickness of a material listed in table 4.11		

Table 4.13: Design variable limits for the HF scanner flexure

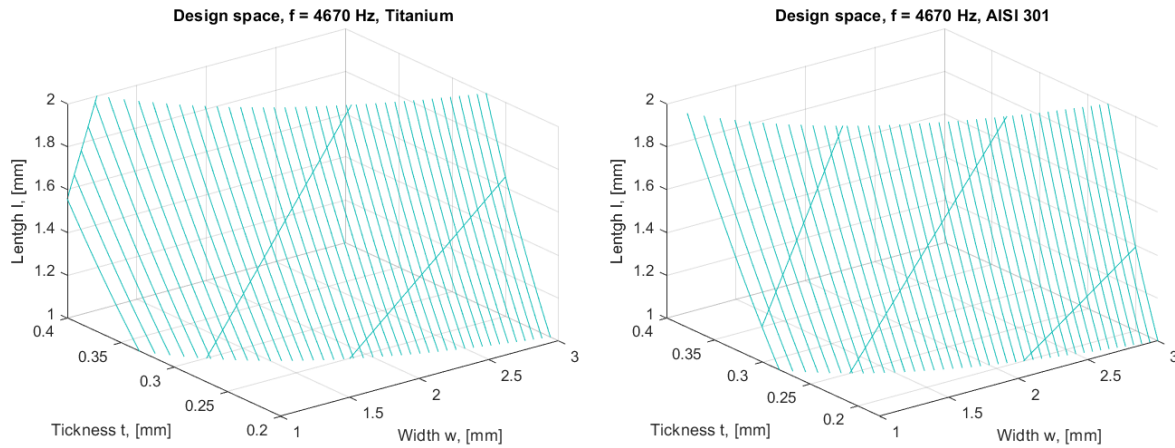


Figure 4.35: HF flexure configurations for flexure material of AISI301 and titanium grade 5 at resonance frequency of 4670 Hz

Initially, the design space was meant to be filtered to remove configurations that have frequencies of unconstrained modes at less than factor  $f_{thumb}$  higher than the frequency of the first mode. When such a rule was applied to the design space, no feasible results were found. This behaviour is not unexpected, as the flexure is under constrained, making it difficult to have sufficient stiffness for those DOF. Therefore, the frequency requirement  $f_{thumb}$  was reduced to 4,5. Additionally, the resultant design space is filtered to find configurations that have a maximum stress, which is less than the fatigue limit. With the mentioned filtering rules applied, around 20 configuration for each material are found. The results are displayed in figure 4.36.

Titanium grade 5							Stainless steel AISI 301						
Desired rotation frequency [Hz]	Unconstrained translation frequency [Hz]	Unconstrained rotational frequency [Hz]	Stress, [Mpa]	t,[mm]	w,[mm]	l,[mm]	Desired rotation frequency [Hz]	Unconstrained translation frequency [Hz]	Unconstrained rotational frequency [Hz]	Stress, [Mpa]	t,[mm]	w,[mm]	l,[mm]
4561	23380	43771	66	0,25	1,80	1,00	4563	22588	42662	90	0,20	2,10	1,00
4630	23702	44374	66	0,25	1,85	1,00	4620	22855	43167	90	0,20	2,15	1,00
4698	24020	44970	66	0,25	1,90	1,00	4677	23119	43666	90	0,20	2,20	1,00
4585	22325	42067	63	0,25	1,90	1,05	4564	21488	40847	86	0,20	2,20	1,05
4765	24334	45558	66	0,25	1,95	1,00	4733	23381	44159	90	0,20	2,25	1,00
4650	22617	42617	63	0,25	1,95	1,05	4619	21731	41309	86	0,20	2,25	1,05
4714	22905	43160	63	0,25	2,00	1,05	4673	21971	41765	86	0,20	2,30	1,05
4606	21361	40511	60	0,25	2,00	1,10	4727	22208	42217	86	0,20	2,35	1,05
4778	23190	43696	63	0,25	2,05	1,05	4779	22443	42664	86	0,20	2,40	1,05
4668	21627	41014	60	0,25	2,05	1,10	4721	21148	40460	82	0,20	2,45	1,10
4729	21889	41511	60	0,25	2,10	1,10	4771	21362	40870	82	0,20	2,50	1,10
4596	24711	46081	79	0,30	1,20	1,00	4591	23743	44717	113	0,25	1,25	1,00
4708	25220	47031	79	0,30	1,25	1,00	4695	24213	45603	113	0,25	1,30	1,00
4595	23440	43995	75	0,30	1,25	1,05	4582	22504	42659	107	0,25	1,30	1,05
4702	23905	44866	75	0,30	1,30	1,05	4681	22933	43472	107	0,25	1,35	1,05
4594	22293	42112	72	0,30	1,30	1,10	4573	21387	40803	102	0,25	1,35	1,10
4696	22718	42914	72	0,30	1,35	1,10	4778	23354	44269	107	0,25	1,40	1,05
4593	21253	40404	69	0,30	1,35	1,15	4668	21780	41552	102	0,25	1,40	1,10
4690	21643	41145	69	0,30	1,40	1,15	4761	22165	42287	102	0,25	1,45	1,10
4786	22026	41874	69	0,30	1,45	1,15	4746	21090	40494	98	0,25	1,50	1,15
4777	21017	40211	66	0,30	1,50	1,20	4701	22095	42310	116	0,30	1,00	1,15
							4742	21240	40933	112	0,30	1,05	1,20

Figure 4.36: Computed HF flexure configurations that have higher order modes at least 6 times higher than first mode, and a maximum stress that is lower than the fatigue limit

The computed results indicated that the most limiting factor in the design is the unconstrained trans-

lation resonance frequency, which is only about 4.5 times larger than desired rotation frequency. No configurations were found, which have a sufficient unconstrained translational frequency. The unconstrained rotational frequency is about 9 times larger than the desired rotational frequency. Another interesting observation, is that the maximum stress experienced by the flexure reduces with a reducing flexure thickness. In addition, the length of the flexure is almost equal or nearby the minimum allowable value of 1 mm. This is because the stiffness of each of the DOF is inversely proportional to the length, therefore, a higher stiffness is reached with a smaller beam length.

The difference between the frequencies for feasible configurations of titanium grade 5 and stainless steel AISI 301 are not substantial. In both cases, very similar values for the unconstrained translation and unconstrained rotation frequency are achieved. A slight difference exists in the maximum stress values. For stainless steel the maximum stress computed for a feasible configuration is 72 % of the limit. For titanium the maximum stress computed for a feasible configuration is 63 % of the limit. Both of the materials have configurations with relatively big beam widths reaching up to 2.5 mm. Having larger dimensions results in less sensitivity to machining tolerance, which is a desired parameter.

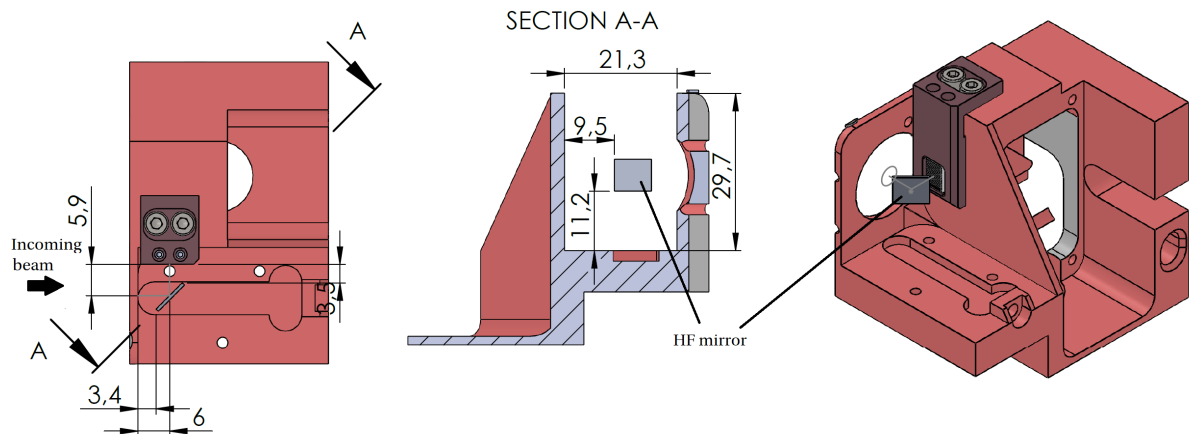


Figure 4.37: HF mirror position in the OPMOD

To select the right flexure configuration the analytically derived flexure configurations need to be checked with FEA to determine, whether the frequencies of both analyses match. The geometry data in figure 4.36 is enough to have a preliminary flexure design. The available space is very limited, as showcased in figure 1.10. A closer look shows that this is very problematic, as the mirror needs to be very close to the other OPMOD elements. In addition, the original scanner has an integrated translation and rotation alignment mechanism, with is also desired for the prototype, so that misalignment would not be the reason for a failed test. It is also foreseen that several flexures will be tested, therefore, a removable mounting is desired. All of these factors limit the possible solutions for mounting the flexure. Therefore, it is selected that the prototype flexure will be mounted with bolts.

The designed flexure is showcased in figure 4.38. The flexure is unsymmetrically mounted with three bolts as there is no available space for an additional bolt. Such mounting leads to over constraint, however, without gluing the flexure, there is no other option of making the flexure removable that would be feasible in such a small space.

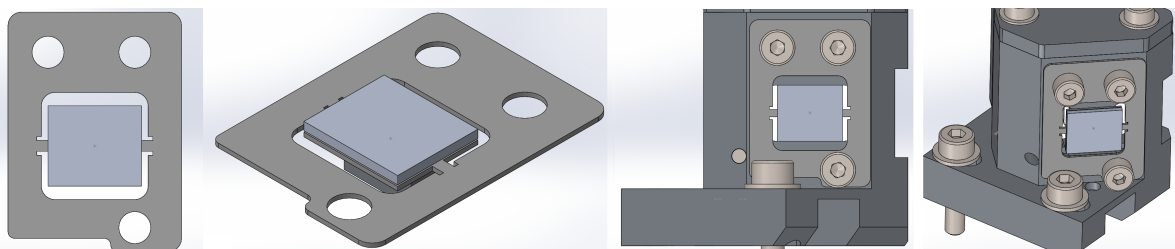


Figure 4.38: Left: Preliminary HF flexure configuration. Right: Preliminary HF flexure configuration mounted in the housing.

As the flexure has a preliminary design, it is now possible to compute the performance of different flexure configurations, that are listed in figure 4.36. *Solidworks Simulation* is used to do conduct the frequency analysis of the flexure. The boundary conditions for the flexure are showcased in figure 4.39. The radius at the bases of the torsion beam is assumed 0.1 mm as the jet of the water jet cutter has a diameter of 0.2 umm. Fixed boundary conditions are assumed on the base surface of the flexure and the bolt contact areas. This is the most constrictive boundary condition, but it is fine for a first estimation.

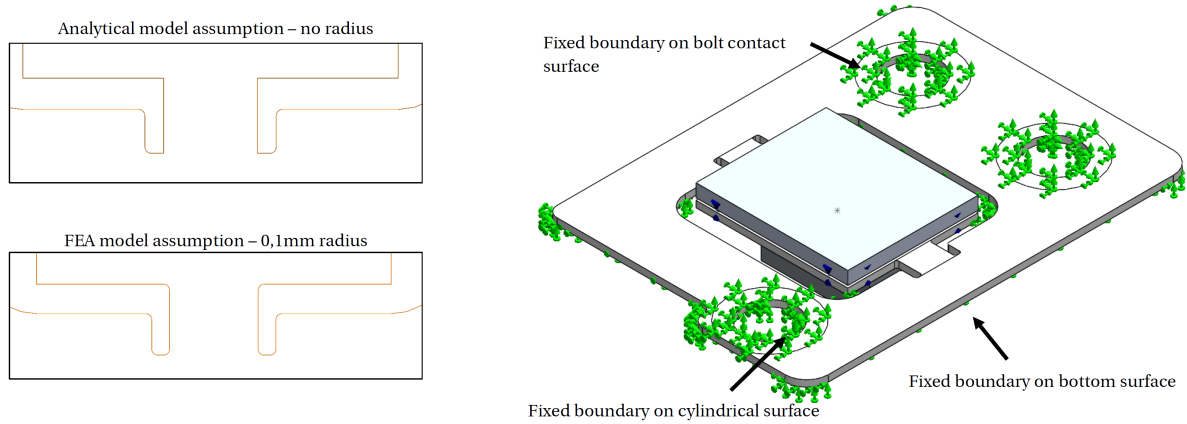


Figure 4.39: FEA model assumptions and boundary conditions

The computed first mode of each of the selected flexure designs is showcased in figure 4.40. It is clear, that there is a discrepancy between the analytical model and the FEA results. The difference in results seems to be related to the ratio between of the beam width and thickness. Where the ratio is large, the difference seems to be bigger. For example, the AISI301 configuration with  $t = 0.2\text{ mm}$ ;  $w = 2.1\text{ mm}$ ;  $l = 1.00\text{ mm}$ ; the ratio is 10.5 and there is a frequency difference of 1,76. Whereas for the AISI301 configuration with  $t = 0.3\text{ mm}$ ;  $w = 1.00\text{ mm}$ ;  $l = 1.15\text{ mm}$ ; the ratio is 3,3 and there is a frequency difference of 1.12. The same behaviour can be observed for the titanium configurations. Because the flexure configurations with larger beam widths have a larger frequency discrepancy, the width (or the length) needs to be reduced to achieve the required resonance frequency of the first mode. That means, that the beam dimensions will converge towards lower width to thickness ratio. Therefore, it is best to select the values computed by the analytical model, which already have a low width to thickness ratio and then optimize the selected geometry.

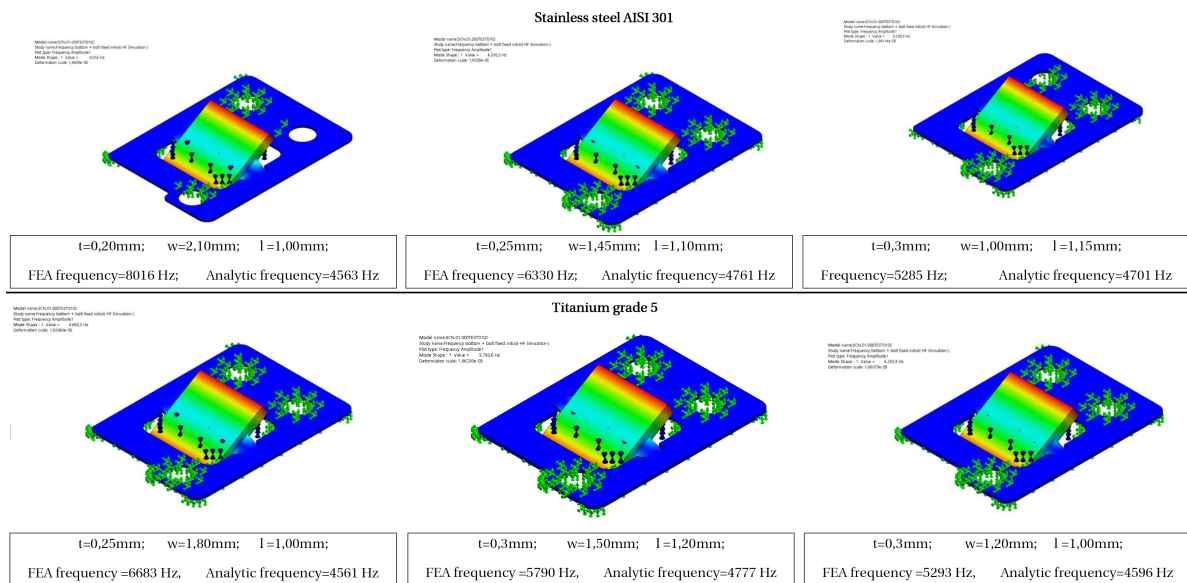


Figure 4.40: First mode of each of the selected flexure designs for stainless steel AISI 301 and titanium grade 5

Flexure configurations of both materials that experience similar level of frequency discrepancy have almost equal torsion beam lengths and widths (right side of figure 4.40). Therefore, flexures made either of titanium or stainless steel will have the same level of sensitivity to machining tolerances. Thus, the AISI 301 material is chosen as the flexure material for the HF scanner, as it is cheaper and more widely available. The flexure configuration  $t = 0.3 \text{ mm}$ ;  $w = 1.00 \text{ mm}$ ;  $l = 1.15 \text{ mm}$  is selected as the base configuration, because it has the lowest width to thickness ratio.

#### 4.5.7. Boundary condition influence to frequency

Boundary conditions for the HF flexure with geometry of  $t = 0.3 \text{ mm}$ ;  $w = 1.0 \text{ mm}$ ;  $l = 1.15 \text{ mm}$  is investigated by comparing three different situations. The boundary conditions for the flexure are displayed in figure 4.42. The first situation is the already used condition of fixed faces, which assumes no displacement for the selected faces. This is the most strict assumption resulting in the stiffest configuration. However, these boundary conditions are not realistic, as the stiffness between the flexure and the housing is finite. A less strict boundary condition is roller contact on the bottom surface of the flexure and a radial translation boundary for cylindrical bolt hole surfaces. Such boundary conditions allow for in plane flexing of the flexure. However, the flexure contact surfaces with the housing and bolt still are assumed to have infinite stiffness. The last configuration assumes a finite stiffness normal to the contact surface between the flexure and the housing. The finite stiffness is estimated by using the methodology described by Shigley [27]. The stiffness of each frustum, showcased in figure 4.41, is calculated by:

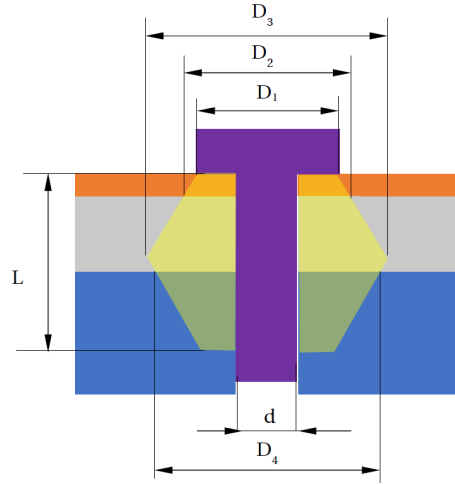


Figure 4.41: Tapped joint stress distribution frustums used to determine joint stiffness

$$k_{frust} = \frac{0,577\pi Ed}{\ln \frac{(1,155t_f + D - d)(D + d)}{(1,155t + D + d)(D - d)}} \quad L = t_w + t_{flex} + d; \quad (4.22)$$

where

$k_{frust}$  = stiffness of an individual frustum [N/m]

$d$  = inner diameter of the frustum [m]

$D$  = smallest value of the frustum outer diameter [m]

$t$  = frustum thickness [m]

$E$  = material Young modulus [MPa]

$t_f$  = frustum height [m]

$t_w$  = washer thickness [m]

$t_{flex}$  = flexure thickness [m]

$L$  = joint grip length [m]

The frustum angle is assumed to be  $\alpha = 30^\circ$ . The flexure is mounted by M2 bolts with washers, by screwing the bolts into a tapped hole. The estimated stiffness of one such member joint is  $k_{bolt} = 7.76 \times 10^8 \text{ N/m}$ . With three bolts the total stiffness triples. The total stiffness is assumed to be acting on the flexure housing contact surface. This assumption is not particularly accurate because in reality the stiffness of the flexure is not the same in each position, however, it is a suitable estimation to investigate mounting stiffness influence. The boundary condition configurations and the respective first mode frequencies are illustrated in figure 4.42.

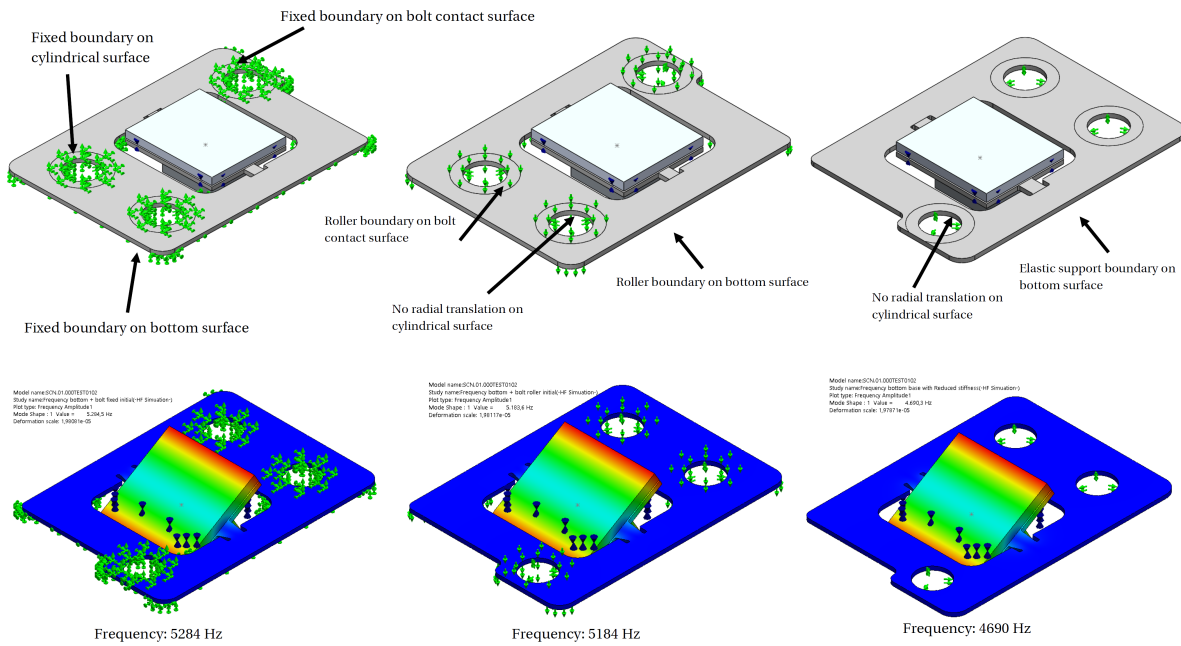


Figure 4.42: FEA boundary condition comparison for AISI 301 flexure  $t = 0.3 \text{ mm}$ ;  $w = 1.0 \text{ mm}$ ;  $l = 1.15 \text{ mm}$

The results show that the resultant resonance frequency of the first mode (and other modes) varies significantly. While there was only a 100 Hz difference between the fixed and roller contact configurations, there was a difference of around 600 Hz between fixed and elastically supported flexure. Therefore, it can be concluded that the resonance frequency of the flexure is very sensitive to boundary conditions. The real resonance frequency of the manufactured scanner may be somewhere between the computed values. Therefore, the best approach to determine the flexure geometry parameters would be to build several different models of flexure and test them.

Flexure version	Desired rotation frequency [Hz]	Unconstrained translation frequency [Hz]	Unconstrained rotation frequency [Hz]	Torsion beam length [mm]	Torsion beam width [mm]	Torsion beam thickness [mm]
1	4822	14494	23452	1,25	0,95	0,3
2	5153	15580	24253	1,20	1	0,3
3	5511	16743	24990	1,15	1,05	0,3

Table 4.14: Flexure versions manufactured for testing

Through trial and error, three flexure models were selected and are listed in table 4.14. The frequencies were determined with the roller contact boundary condition. The resultant desired frequencies are larger than the required operational requirement, because the roller contact boundary conditions is very restrictive, therefore, it is expected that the real resonance frequencies of the flexures will be lower. The difference in resonance frequency between the flexure version 1 and 3 is around 700 Hz, which is assumed to be enough margin. The first five modes of the test flexures are showcased in figure 4.43.



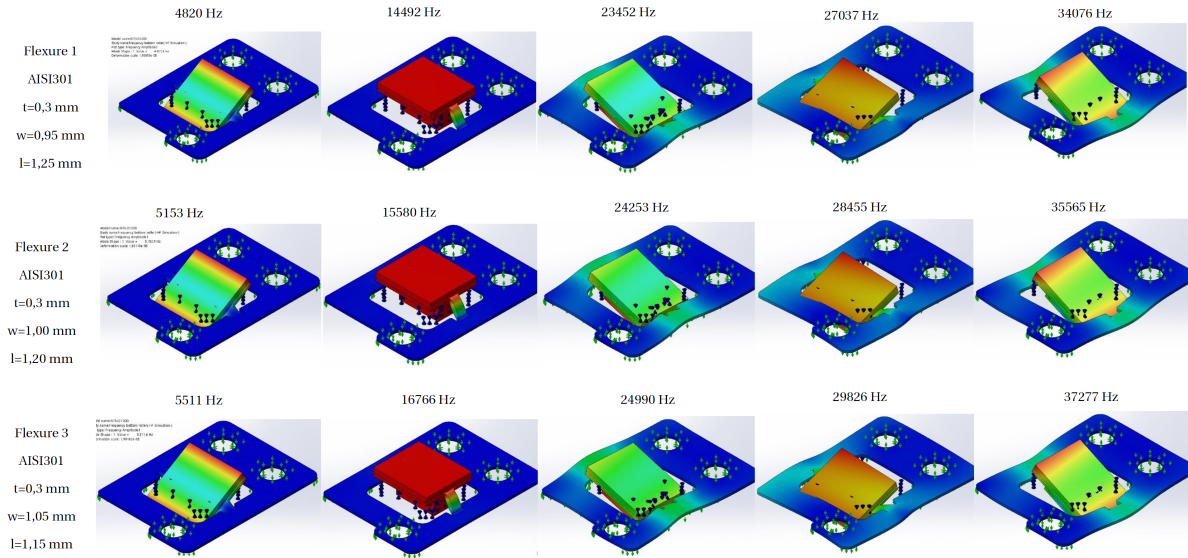


Figure 4.43: First 5 modes of each flexure model

As predicted by the analytical model, modes 2 and 3 represent the unconstrained DOF. The resonance frequency of the unconstrained translation is only about 3,3 times higher than the operational frequency. The resonance frequency of the constrained rotation is only about 5,2 times higher than the operational frequency. However, if mode 2 were to be excited, the translation of the mirror would result with beam motion along the scan line. Therefore, the motion of mode 2 should not negatively effect the performance of the scanner. The same cannot be stated about mode 3, because the unconstrained rotation would result in beam motion perpendicular to the scan line. Therefore, the motion of mode 3 could result in a warped scan beam. A warped scan beam may result in an improperly scanned image. Even though, the higher order modes are relatively close to the operational frequency, there are no additional options to improve the performance as the flexure is inherently limited by the two dimensional design. Whether higher order modes are significant to the performance of the scanner, will be observed during scanner validation.

#### 4.5.8. Operational loads

A linear dynamic FEA simulation is conducted with *Solidworks Simulation* in order to determine the deformation and stress at the operating frequency. The loads acting on the magnet were computed in section 4.2.9, however, the forces and the torque are summed up over the entire magnet surface and outputted with respect to the axis of rotation. To make an equivalent estimation, the force values will be assumed the same, as computed in section 4.2.9. However, their application point will be corrected, so that an equivalent torque equal to the torque generated by the electromagnetic actuator would be created. For simplicity, the study is conducted by assuming that the loads are sinusoidal, which is not exactly true, as the current generated by the HF electronics has a triangular shape, as illustrated in figure 4.27. The RMS current for the triangular shape waveform was estimated as 32 mA. Assuming the same amount of RMS current for a sinusoidal signal, the peak current would then be  $I_{max} = 45.3$  mA. Due to the small rotation of the HF scanner, the loads can be assumed equal to the loads acting at 0 mrad rotation. The loads that are acting on the scanner are listed in table 4.15.

Torque	Lateral force	Vertical force
$3.12 \times 10^{-4}$ Nm	0.137 N	0.373 N

Table 4.15: Loads acting on the HF scanner magnet at a rotation of 0 mrad and at a current of 45.3 mA

In section 4.2.10 it was stated, that the vertical force acting in the Z direction varies only by 0.03 %. It is two magnitudes smaller than the force in the Y direction, therefore, it can be disregarded in the dynamic analysis. The application point of the lateral force is corrected, as showcased in figure 4.44.

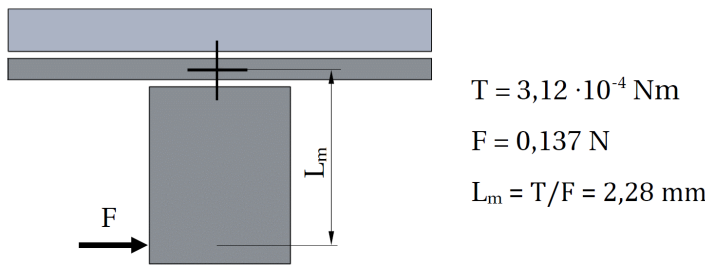


Figure 4.44: Load schematic of HF scanner used in the dynamic analysis

The load frequency is set to  $f = 4650 \text{ Hz}$  and the damping ratio is considered  $\zeta = 0.05$ . The resultant stress and displacement plots are showcased in figure 4.45.

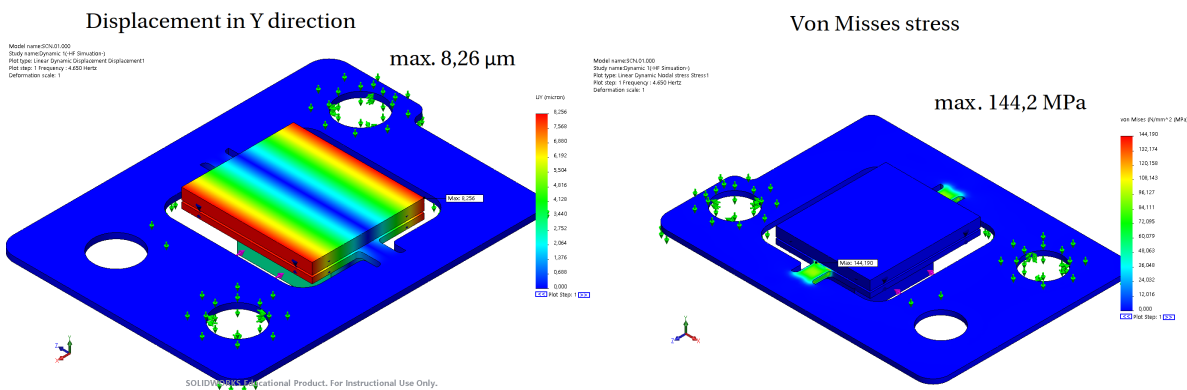


Figure 4.45: HF scanner stress and displacement when loaded by a  $F = 0.131 \text{ N}$  lateral force at a frequency of  $f = 4650 \text{ Hz}$

The maximum displacement in the Y direction, which occurs on the facet edge of the mirror is  $8.26 \mu\text{m}$  and is  $0.74 \mu\text{m}$  short of the requirement showcased in figure 1.7. This would mean, that the HF scanner does not reach the required  $3 \text{ mrad}$  amplitude, however, the flexure, that is simulated has a resonance frequency at  $4822 \text{ Hz}$ , which is  $172 \text{ Hz}$  away from the required resonance frequency. Therefore, if the real resonance frequency is closer to the operating frequency the amplitude would be higher. This is showcased in figure 4.46 which illustrates output displacement of the mirror facet with respect to the load frequency. The load frequency was varied from  $4550 \text{ Hz}$  to  $5150 \text{ Hz}$ . The plot showcases that the displacement of  $9 \mu\text{m}$  is achieved between load frequencies of  $4710 \text{ Hz}$  and  $4900 \text{ Hz}$ , which would give a bandwidth for feasible operation of  $f_b = 190 \text{ Hz}$ . This study shows that the scanner is able to achieve the required amplitude if the resonance frequency is at a sufficient value. However, due to the uncertainty of the boundary condition influence on the resonance frequency, the performance of the scanner can be better or worse. Therefore, three different flexure models were designed (table 4.14) and will be tested in the prototype, to determine what is the right flexure geometry, that ensures that the scanner reaches the required amplitude at the operating frequency.

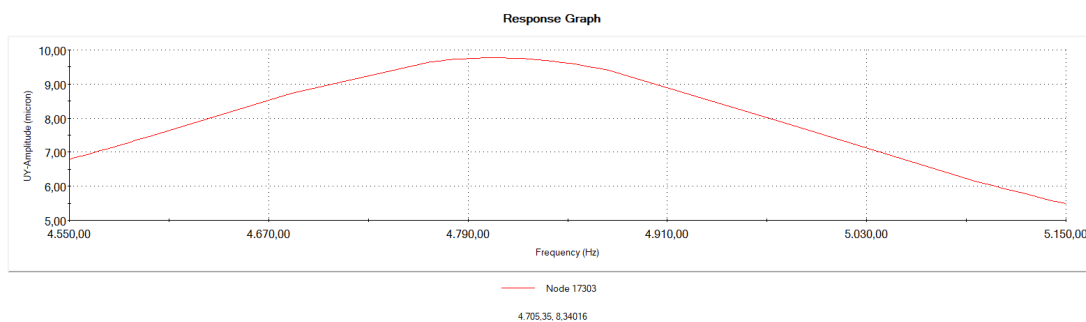


Figure 4.46: HF scanner displacement frequency response when loaded by a  $F = 0.137 \text{ N}$  lateral force

The maximum stress of the flexure at the operating frequency was recorded to be 144.2 MPa, which is below the  $\sigma_{301} * 162$  MPa fatigue limit. However, because the scanner does not reach the required amplitude, the stress is not the maximum value achieved during operation. Figure 4.47 illustrates the stress with respect to the frequency. The fatigue stress limit is not exceeded throughout the whole computed frequency range.

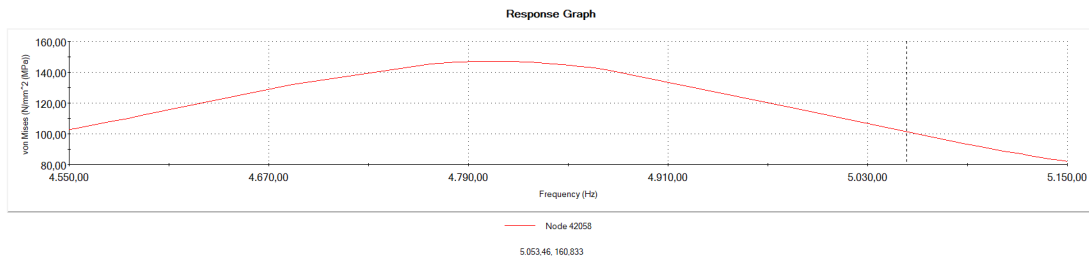


Figure 4.47: HF scanner stress frequency response when loaded by a  $F = 0.137$  N lateral force

Finally, the static vertical electromagnetic load is evaluated. The resultant stresses and displacement are displayed in figure 4.48. The maximum stress is 10.1 MPa and the maximum displacement is  $0.19 \mu\text{m}$ . If the stresses due to the dynamic loading and the static loading were to be linearly added, the sum would still be less than the fatigue stress limit of  $\sigma_{301} * = 162$  MPa, therefore, the flexure will not experience premature failure.

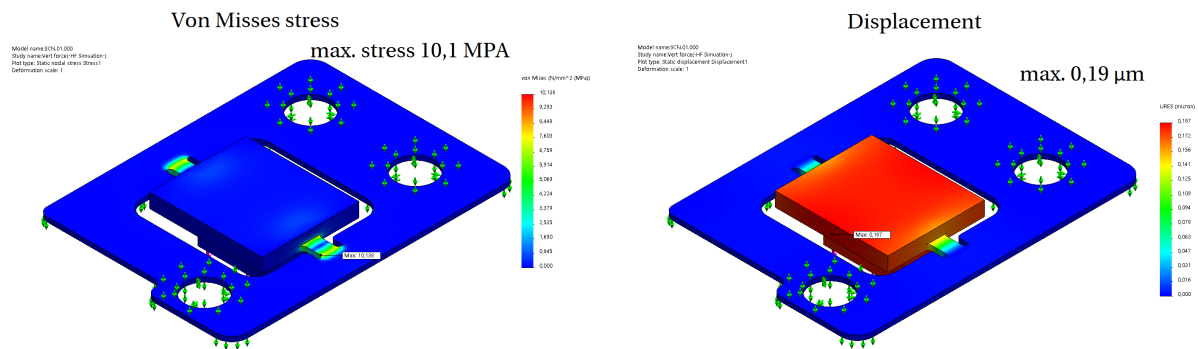


Figure 4.48: HF scanner stress frequency response when loaded by a  $F = 0.137$  N lateral force

#### 4.5.9. Shock loads

Simulations for shock loads of 25G in all three directions were conducted. The maximum stresses that the flexure experiences are showcased in figure 4.49. The maximum stress is recorded for flexure 1 and reaches the value of 4.5 MPa, which is well below the yield stress of the material, therefore, the flexures are not susceptible to shock loads.

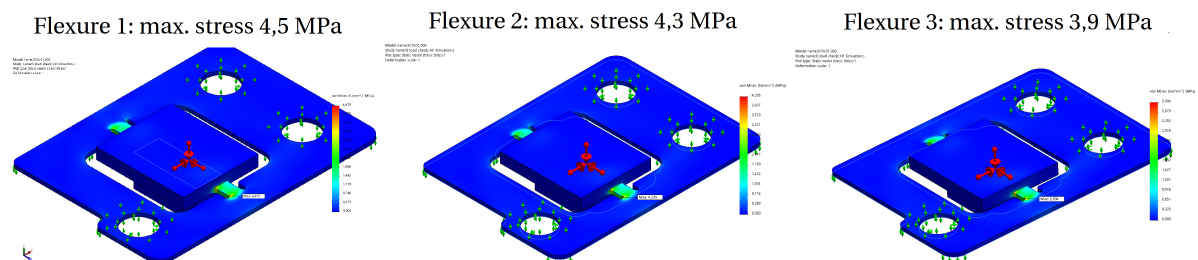


Figure 4.49: Flexure stresses due to a 25 G load in all three direction

4.5.10. LF flexure design

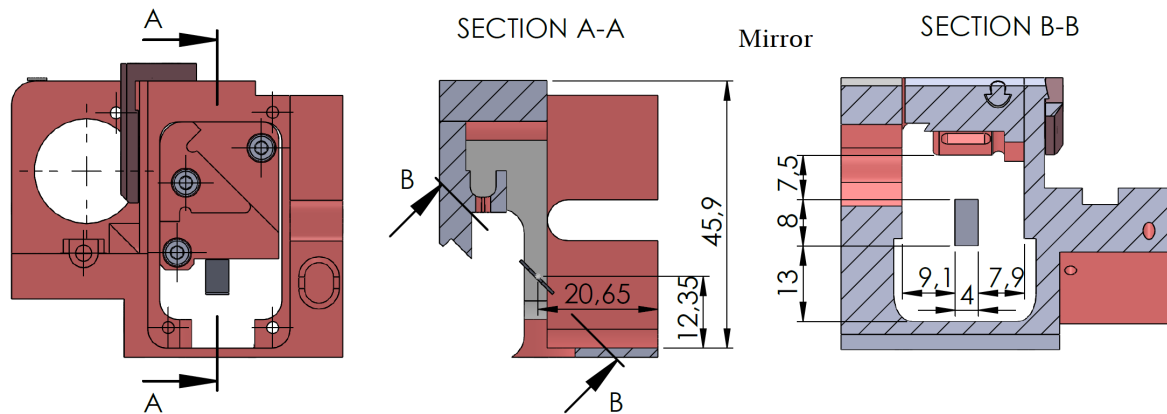


Figure 4.50: Available space around the LF mirror

The same approach that was used for designing the HF flexure is applied for the LF flexure. The available space around the LF mirror determines the maximum dimensions of the torsion beam. The available space is showcased in figure 4.50.

By using the same reasoning, as in section 4.5.6, the beam dimension limits are selected for the LF torsion beam. The design variable limits for the LF flexure are listed in table 4.16.

Variable	Minimum	Maximum	Step size
w	1 mm	7.8	0.05 mm
l	1 mm	5	0.05 mm
t	Based on available sheet thickness of a material listed in table 4.11		

Table 4.16: Design variable limits for the HF scanner flexure

The LF design space is computed for all configurations. A data search is done to find the configurations, which have the desired rotational stiffness at  $k_{LF}=1.70 \times 10^{-2} \text{ Nm/rad}$ , with a tolerance of  $\pm 2.5\%$ . The computed data is filtered to find feasible configurations. Similarly to the HF flexure design, the frequency factor rule of  $f_{thumb} = 10$  did not hold up. However, in this case, even reducing the frequency requirement to 4,5 did not help, as it did in the case of the HF scanner. Even reducing the requirement to 1 did not yield results. The problem of filtering out all of the configurations was not only due to insufficient stiffness, but also to large stresses. In order to at least get some results the fatigue stress requirement calculated in section 4.5.5 was changed, so that the maximum stress value would be considered the fatigue stress of an unnotched specimen. Due to this change, the reliability of the estimated infinite flexure life would not be certain.

However, even with the increased fatigue stress limit the filtered configuration result number was limited. The filtered results, when the fatigue stress limit is set to the unnotched specimen limit and the frequency factor is set to 1,3, are illustrated in figure 4.51. Note, that the filtered results are only displayed for the AISI 301 material, because no feasible results were found for titanium grade 5 at the mentioned filter setting. The available material thickness is too large to achieve small stiffness values with the imposed geometry.

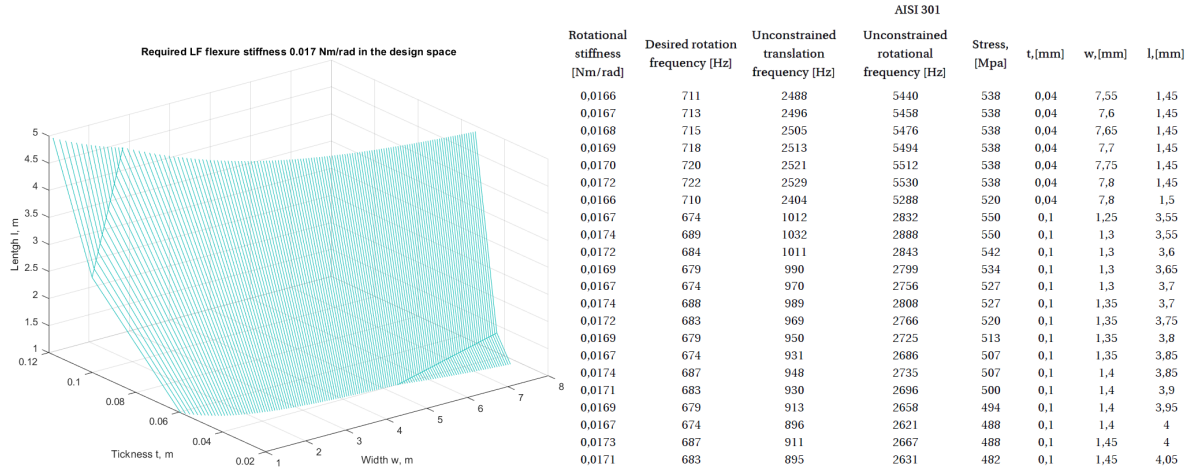


Figure 4.51: Computed results for AISI 301 when the higher order mode frequency factor is  $f_{thumb} = 1,3$  and the fatigue stress is  $\sigma_{301} = 552$  MPa

The data indicates that all of the configurations are fairly limited by the maximum stress, reaching at least 87% of the maximum value. Similarly as in the case of the HF scanner, the unconstrained translational frequency also is a limiting factor, as it is the reason why the frequency factor  $f_{thumb}$  needs to be decreased to 1,3. Some configurations were found that are less burdened by this. For example, configuration  $t = 0.04$  mm,  $w = 7.55$  mm,  $l = 0.04$  mm has an unconstrained translation frequency 3,5 times higher than the desired rotation frequency. However, similarly as in section 4.5.6, this model has a very high thickness to width ration. Therefore, when simulated with FEA the real rotational frequency does not match the analytically determined value. In any case, the unconstrained mode frequencies for all configurations are too low to ensure proper performance of the LF scanner. Therefore, it can be concluded that the flat torsion beam is not suitable to provide enough stiffness for the unconstrained DOF of the LF scanner. A different torsion beam type or a different guiding mechanism must be used.

#### 4.5.11. U torsion beam for LF flexure

The flat torsion beam was selected in section 3.4.2, because it was the simplest to manufacture and the most compact design. While the flat torsion beam flexure is arguably suitable for the HF scanner, with the given design space no feasible configurations can be found for the LF scanner. The next flexure concept that is also compact, and relatively simple is the U shape torsion beam. The geometry describing the cross-section of the U shape torsion beam is showcased in figure 4.52.

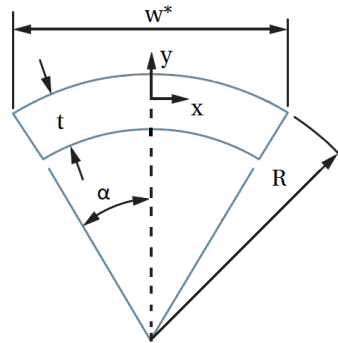


Figure 4.52: U shaped cross-section of torsion beam

The area moments of inertia for a U shaped torsion beam are expressed as:

$$I_x = R^3 t \left( \left( 1 - \frac{3t}{2R} + \frac{t^2}{R^2} - \frac{t^3}{4R^2} \right) \left( \alpha + \sin \alpha \cos \alpha - \frac{2 \sin^2 \alpha}{\alpha} \right) + \frac{t^2 \sin^2 \alpha}{3R^2 \alpha (2 - t/R)} \left( 1 - \frac{t}{R} + \frac{t^2}{6R^2} \right) \right) \quad (4.23)$$

$$I_y = R^3 t \left( 1 - \frac{3t}{2R} + \frac{t^2}{R^2} - \frac{t^3}{4R^3} \right) (\alpha - \sin \alpha \cos \alpha) \quad (4.24)$$

The torsion constant of the cross section is expressed as:

$$J_U = \frac{Ut^3}{3} \quad U = 2\alpha(R - t/2) \quad (4.25)$$

The maximum stress of a U shaped torsion beam loaded in torsion is expressed as:

$$\sigma_{max} = \frac{T(3U + 1,8t)}{U^2 t^2} \quad U = 2\alpha(R - t/2) \quad (4.26)$$

With the cross-section and torsion beam constant determined, the stiffness values of the beam can be computed. The selected design space limits are showcased in table 4.17. The minimum length  $l$  is set to 1 mm, to have a dimension tolerance of only  $\pm 5\%$ . The minimum radius  $R$  and angle  $\alpha$  are selected as reasonably manufacturable values. The maximum beam length  $l$  is determined by the available space. The maximum angle  $\alpha$  is set to  $45^\circ$ , which is the maximum manufacturable value. The maximum radius  $R$  is set to 30 mm, as more feasible results appear if the value is increased further. The step sizes are set according to either a manufacturing tolerance, or set to have a reasonably fine design space.

Variable	Minimum	Maximum	Step size
R	1 mm	30 mm	0.1 mm
l	1 mm	5 mm	0.05 mm
$\alpha$	$5^\circ$	$45^\circ$	$1.4^\circ$
t	Based on available sheet thickness of a material listed in table 4.11		

Table 4.17: Design variable limits for the HF scanner flexure

The design space is computed to find flexure stiffness values of  $k_{LF} = 1.7 \times 10^{-2}$  Nm/rad. Then the design space is filtered to find results that have a unconstrained mode frequencies with a frequency factor of  $f_{thumb} = 10$ . The fatigue stress limit was set to the value of an unnotched specimen fatigue limit of 552 MPa. The computed results are showcased in figure 4.53.

AISI 301									
Rotational stiffness [Nm/rad]	Desired rotation frequency [Hz]	Unconstrained translation frequency [Hz]	Unconstrained rotational frequency [Hz]	Stress, [Mpa]	t, [mm]	$\alpha$ , [deg]	R, [mm]	W*, [mm]	l, [mm]
0,0166	710	58552	120923	122	0,04	28,1	5,3	5,0	1
0,0168	715	73976	152779	152	0,04	35,2	4,3	5,0	1
0,0167	712	75799	156543	159	0,04	36,6	4,1	4,9	1
0,0169	716	80079	165382	165	0,04	38,0	4	4,9	1
0,0166	711	81010	167305	171	0,04	39,4	3,8	4,8	1
0,0171	720	84225	173945	171	0,04	39,4	3,9	4,9	1
0,0168	714	84755	175039	177	0,04	40,8	3,7	4,8	1
0,0172	724	88210	182175	177	0,04	40,8	3,8	5,0	1
0,0169	716	88306	182373	183	0,04	42,2	3,6	4,8	1
0,0173	726	92007	190016	183	0,04	42,2	3,7	5,0	1
0,0169	718	91637	189252	189	0,04	43,6	3,5	4,8	1
0,0166	711	88843	184671	180	0,04	43,6	3,6	5,0	1,05
0,0170	719	94723	195625	195	0,04	45,0	3,4	4,8	1
0,0167	712	91947	191124	186	0,04	45,0	3,5	4,9	1,05

Figure 4.53: Computed LF U shape torsion beam results for AISI 301 when the higher order mode frequency factor is  $f_{thumb} = 10$  and the fatigue stress is  $\sigma_{301} = 552$  MPa

The performance of the U shape torsion beam is much better than that of the flat torsion beam, as feasible results can be found with a frequency factor of  $f_{thumb} = 10$ . Therefore, the unconstrained DOF can be considered sufficiently constrained. Additionally, the stress of the U shaped torsion beam are reduced to about

2.5 times when compared to the results computed for the flat torsion beam in figure 4.51. One concerning aspect, is that the width  $w^*$  of the torsion beam reaches values of about 5 mm. This may be problematic, because when the width to thickness ratio of the torsion beam is large, the analytical results start to diverge from FEA. To check the validity of the analytical results the configuration  $t = 0.04$  mm,  $R = 3.5$  mm,  $\alpha = 43.6^\circ$ ,  $l = 1$  mm is selected to be simulated with FEA, as it has the smallest beam width of  $w^* = 4.8$  mm.

However, when making a 3D model of the LF scanner with the U shape torsion beam, design problems become apparent. The 3D model of the flexure is showcased in figure 4.54. An apparent problem of this kind of design is that the surfaces on which the magnet and the mirror need to be mounter are curved, which complicates the assembly process. Additionally, due to the design of the flexure, additional parts of the flexure will be flexing which were not intended to flex.

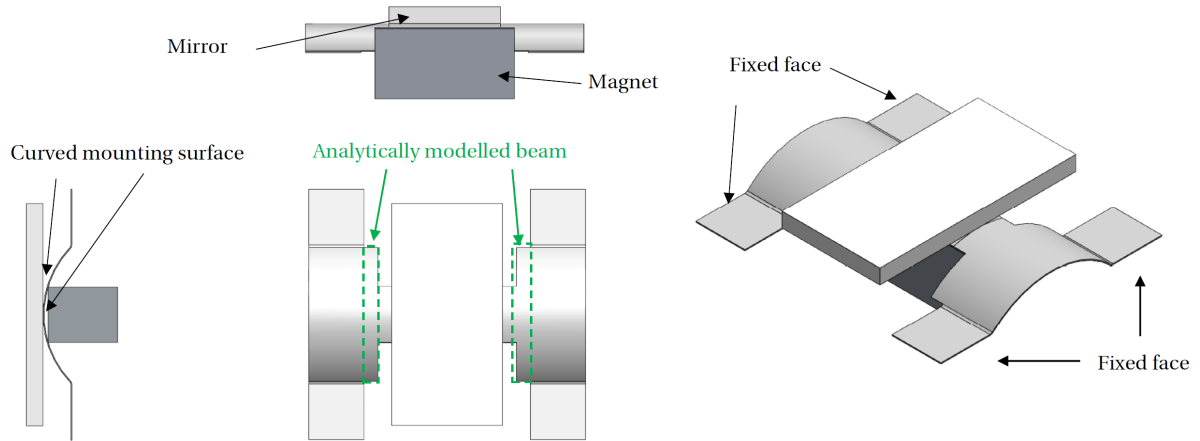


Figure 4.54: CAD model of the LF flexure with the U shape torsion beam

Nonetheless, a frequency analysis of the selected flexure configuration was conducted and the computed first five modes are displayed in figure 4.55. The first mode, which has the desired rotational motion, has a frequency of 1119 Hz which is 55 % higher than the analytical value. Another thing to note, is that the second mode has a frequency of 6064 Hz, which is 5.4 times larger than the first mode. Even though the frequency factor of  $f_{thumb} = 10$  is not reached, the model shows that there is a great improvement in increasing the stiffness of the unconstrained DOF.

Due to the fact that the FEA results differ from the analytically predicted results and the real flexure behaviour would be much more difficult to predict analytically, it is best to use FEA analysis to optimize the LF flexure geometry. However, at this moment in the project no manufacturer was found that could do this small scale bending, therefore, the manufacturing limits of the flexure were unknown. Also, as time was already running behind schedule, therefore, in consultation with the CEO of EasyScan, it was decided to postpone the development of the LF scanner. Therefore, additional design for the LF scanner is not discussed in the further sections.

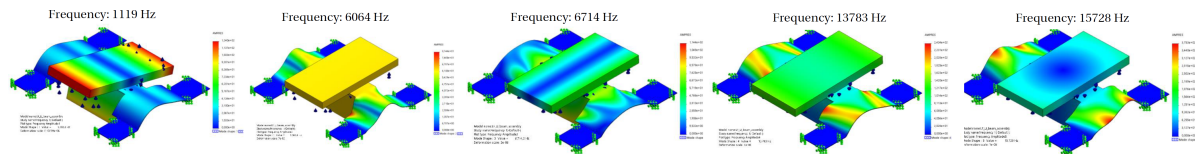


Figure 4.55: First five modes of the LF scanner with the U shape torsion beam

## 4.6. Error budget and sensitivity analysis

Due to the relatively small dimensions of the scanner, tolerances can have a significant influence on scanner performance, namely the resonance frequency. To estimate the total effect, a local sensitivity analysis is done by taking the derivatives of the mathematical expression of the resonance frequency with respect to each of the design variables. The design variables are showcased in figure 4.56. The only exception is done for mirror and magnet misalignment, as the derivative of the resonance frequency with respect to these parameters

is 0 at the design point. Therefore, misalignment error sensitivity is estimated by calculating the effect on frequency at the misaligned design point. The design point is selected to be configuration flexure 2, as it has geometry that is a middle value when compared to flexures 1 and 3. The computed results are showcased in table 4.18.

Parameter	Tolerance	Sensitivity	Effect on frequency
Torsion beam width $W1$	$\pm 0.05$ mm	2835.3 Hz/mm	$\pm 141.8$ Hz
Torsion beam length $L1$	$\pm 0.05$ mm	-1917.5 Hz/mm	$\pm 95.9$ Hz
Mirror width $W3$	$\pm 0.1$ mm	-207.4 Hz/mm	$\pm 20.7$ Hz
Mirror length $L3$	$\pm 0.1$ mm	-63.5 Hz/mm	$\pm 6.3$ Hz
Mirror height $T3$	$\pm 0.05$ mm	-827.3 Hz/mm	$\pm 41.4$ Hz
Flexure base length $B1$	$\pm 0.05$ mm	-89.9 Hz/mm	$\pm 4.5$ Hz
Flexure base width $A1$	$\pm 0.05$ mm	-314.2 Hz/mm	$\pm 15.7$ Hz
Flexure thickness $T1$	$\pm 0.02$ mm	18453.5 Hz/mm	$\pm 369.1$ Hz
Magnet length $L2$	$\pm 0.1$ mm	-245.4 Hz/mm	$\pm 24.5$ Hz
Magnet width $W2$	$\pm 0.1$ mm	-745.3 Hz/mm	$\pm 74.5$ Hz
Magnet height $T2$	$\pm 0.1$ mm	-1248.5 Hz/mm	$\pm 124.8$ Hz
Mirror glue thickness $H2$	$\pm 0.05$ mm	-146.7 Hz/mm	$\pm 7.3$ Hz
Magnet glue thickness $H1$	$\pm 0.05$ mm	-1185.9 Hz/mm	$\pm 59.3$ Hz
Mirror misalignment $X3$	$\pm 0.2$ mm	-116.8 Hz/mm	$\pm 23.4$ Hz
Magnet misalignment $X2$	$\pm 0.2$ mm	-168.8 Hz/mm	$\pm 33.8$ Hz
Root square sum of effect on frequency			$\Delta_M = \pm 441.1$ Hz

Table 4.18: Error budget analysis for the HF scanner

The total predicted tolerance on frequency is  $\Delta_M = \pm 441.1$  Hz of which the main contributor is the flexure thickness. The tolerance of the flexure thickness is based on the tolerance of the metal sheet that the flexure is cut out of. To improve this tolerance, additional machining would have to be introduced or a better tolerated sheet must be used.

Torsion beam width and length are tolerances which have also have significantly large effect on the tolerance of the scanner frequency. This is because these dimensions determine the stiffness of the flexure. A more accurate manufacturing process would have to be chosen in order to reduce the effect on frequency from these two variables.

Another surprisingly influential parameter is the magnet height. However, the tolerance of the magnet is given by the manufacturer, therefore, nothing can be done to improve it, apart from changing the magnet and reconfiguring the actuator.

What is interesting is that mirror and magnet misalignment constitute less than 10% of the total tolerance, which would mean that a lot of effort does not have to be made to position them accurately. However, this proposition has to be taken with caution as the effect of misalignment on magnetic circuit performance is not evaluated. Additionally, the effect of bolt induced stress is not included in this analysis.

The estimated tolerance  $\Delta_M$  is already larger than the frequency bandwidth of  $f_b = 190$  Hz, estimated in section 4.5.8. Even though frequency bandwidth is estimated by varying the input load frequency, according to equation 3.1, the result would still be the same if the resonance frequency of the scanner was varied instead. Because the frequency bandwidth is more than twice smaller than the tolerance  $\Delta_M$ , it is likely that the scanners will have to use more current than it was initially designed for, in order to account for the high machining tolerance.

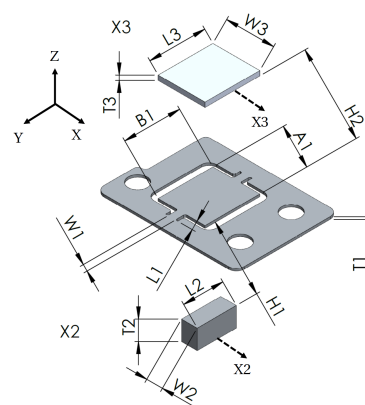


Figure 4.56: Sensitivity analysis design variables



## 4.7. Finalized magnetic actuator

With the magnetic circuit and the flexure designed, the only thing left to do is to put everything together. Because the scanner is already small, designing a separate ferromagnetic yoke, which would be mounted in the housing would be complicated and take up additional assembly time. Therefore, it was decided to design the housing out of the ferromagnetic AISI 430, so that the whole housing, would be acting as a ferromagnetic yoke. That benefit is, that the reluctance of the ferromagnetic yoke itself is greatly reduced, due to the large cross sectional areas of the housing. The finalized HF scanner is showcased in figure 4.57.

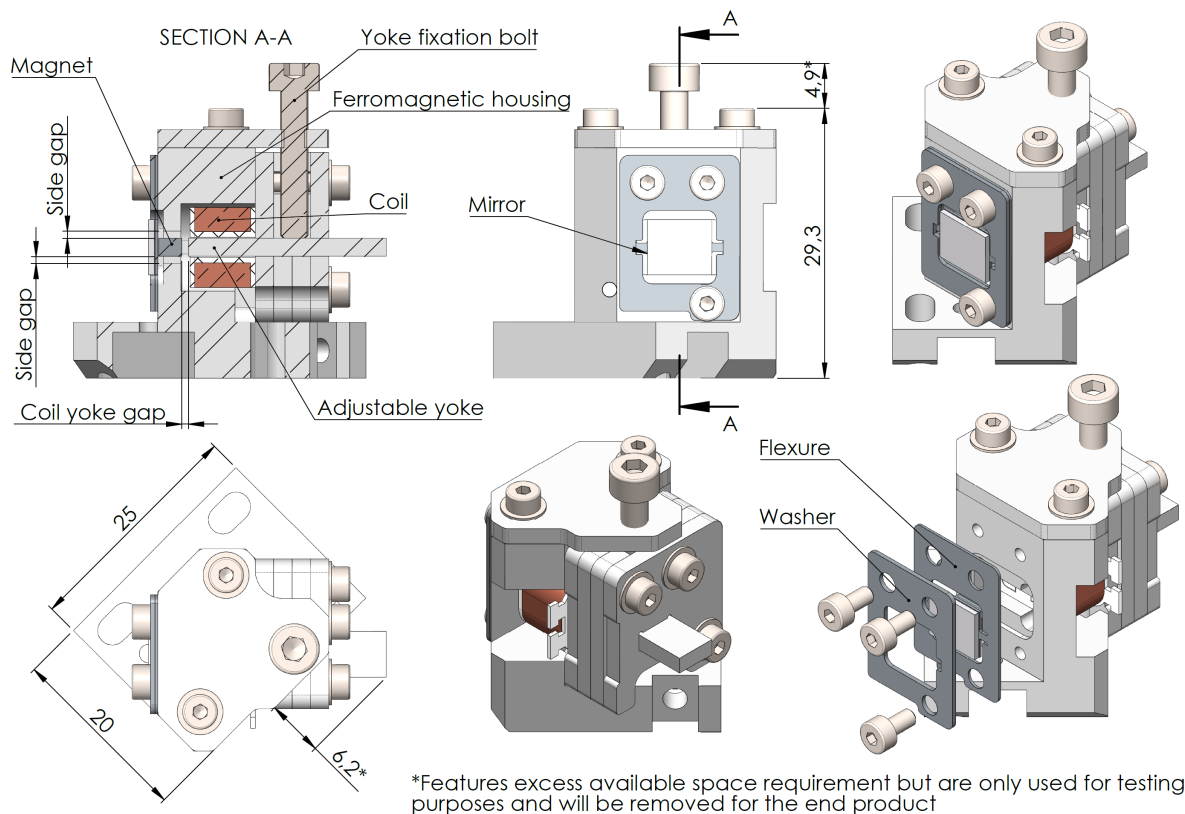


Figure 4.57: Finalized HF scanner design

To impose the strict boundary conditions, discussed in section 4.5.7, a custom washer is manufactured. The washer has a form, which covers the whole flexure, except the torsion beam. The finalized design is computed in COMSOL to check the magnetic field density distribution. The simulation is ran at a current level of  $I=0.18\text{A}$ , which is almost three times higher than the peak current of 55 mA, determined in section 4.4. Therefore, the computed results will have a margin of safety for saturation, in case higher current was needed to be used. The results are showcased in figure 4.58. The maximum magnetic field density in the yoke is located at the facets close to the magnet and reach the value of 0.9 T. The saturation flux density of AISI430 is 1.5 T, therefore, the yoke will not be saturated.

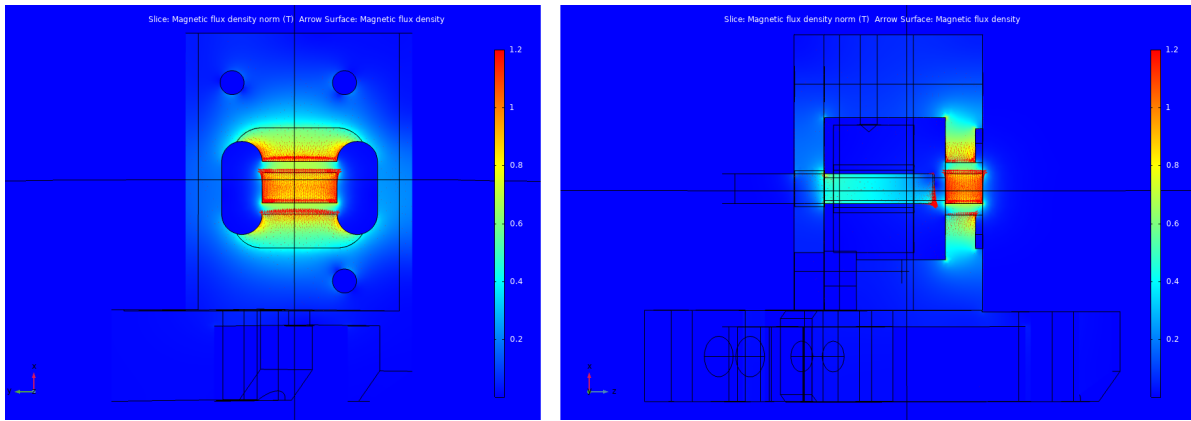


Figure 4.58: Magnetic field density of the finalized HF scanner when the current is  $I = 0.18\text{A}$

## 4.8. Scanner assembly

To achieve optimal performance, the scanner must be assembled accurately. While the scanner's resonance frequency is most sensitive to manufacturing tolerances, it is still important to glue the magnet and the mirror as accurately as possible. The flexure does not have reference surfaces from which the position of the mirror and the magnet could be precisely set. Therefore, a gluing jig was designed and 3D printed from PLA, which is showcased in figure 4.59.

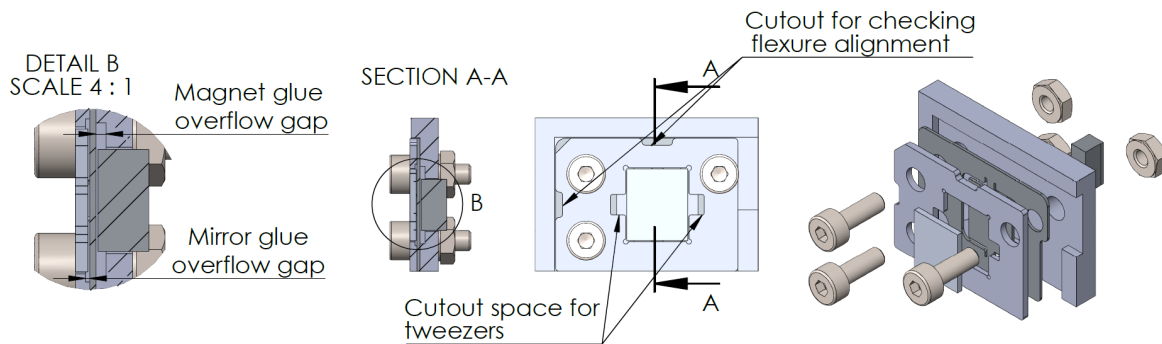


Figure 4.59: Flexure gluing jig

It is important to not glue the jig to the parts, therefore, gaps for glue overflow are designed in the gluing jig. Moreover, cut-outs are made to make space for tweezers that hold the mirror, so that the mirror can be placed properly. Furthermore, extra cut-outs are made in the gluing jig, through which flexure contact with the gluing jig can be seen. This is used in order to visually inspect, whether the flexure is aligned with the gluing jig.

The structural adhesive for the flexure must be strong and resistant to vibrations. Additionally, it has to offer good contact strength between metallic and glass parts. *3M™ Scotch-Weld™ Epoxy Adhesive 2216* is a two-part, room temperature curing epoxy with high peel and shear strength. Technical properties of the adhesive are listed in table 4.19. The average shear stress on the magnet joint from a  $F_L = 0.137\text{N}$  lateral force is  $\tau_S = 0.014\text{MPa}$ . The average shear stress is three orders of magnitude less than the shear stress limit of the adhesive, therefore, a more comprehensive study of the glued joint is not done and it is assumed that the joint has sufficient strength.

To cure the adhesive faster, a lab oven was used, which was set to  $45^\circ\text{C}$ . This temperature is used, because the gluing jig material PLA has a glass transition temperature at  $T_G = 60^\circ\text{C}$ . Therefore, a lower temperature needs to be used to avoid warping of the gluing jig. The flexures were cured in the oven for 3 hours and then left to cure at room temperature overnight. An assembled flexure is showcased in figure 4.60.

Property	Value
Overlap shear on etched aluminium at 24 °C	22 MPa
Cure time at 24 °C	7 days
Cure time at 66 °C	120 min

Table 4.19: Technical data of adhesive 3M™ Scotch-Weld™ 2216

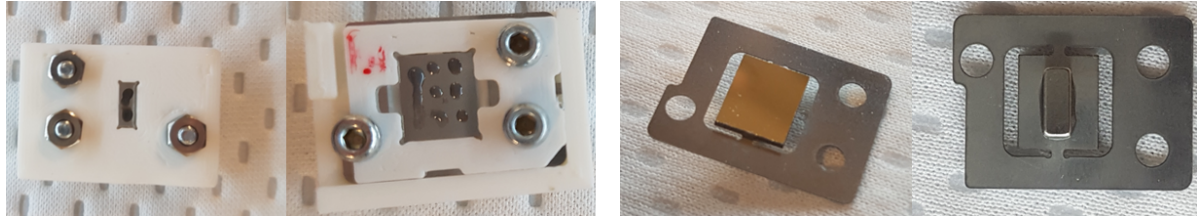


Figure 4.60: Left: Flexure in gluing jig with applied glue. Right: Mirror and magnet glued to flexure

Mounting the flexure in the housing is a sensitive process, because the magnet experiences significant attractive forces when in close proximity to the ferromagnetic yoke. Because the magnet needs to be placed with certain distance from the yoke, proper technique must be used. An optimal approach is to utilize ferromagnetic feeler gauges to position the flexure in the yoke, which is displayed in figure 4.61. Due to the construction of the prototype and the lack of proper tooling, there was uncertainty in the flexure position in the perpendicular direction to the gaps as indicated by figure 4.61.

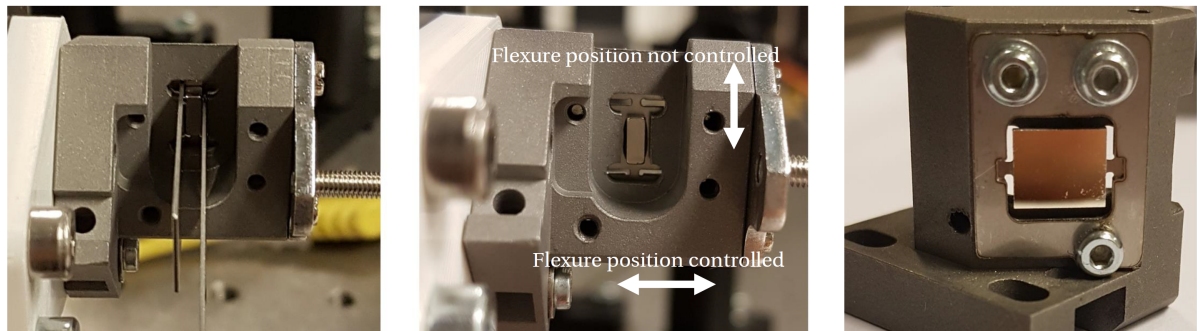


Figure 4.61: Left: Magnet centred with feeler gauges. Center: Flexure mounted in housing. Right: Front view of scanner

The actuator coil was wound manually on a 3D printed bobbin made from PLA[4]. A manual coil winding assembly was designed and used for winding the coil. Because the coil and the wire are relatively small, it is difficult to wind the coil evenly, and to achieve required dimensions. Best results were achieved when using a stereo microscope to accurately see the wire position on the coil during the winding process. The wound coil and the coil winding assembly are displayed in figure 4.62.



Figure 4.62: Left: Manual coil winding assembly. Right: Wounded coil

The distance between the yoke and the magnet is set with feeler gauges and fixed with a tightening screw.

The yoke position setting process and the whole assembled scanner mounted in the EasyScan OPMOD are displayed in figure 4.63:

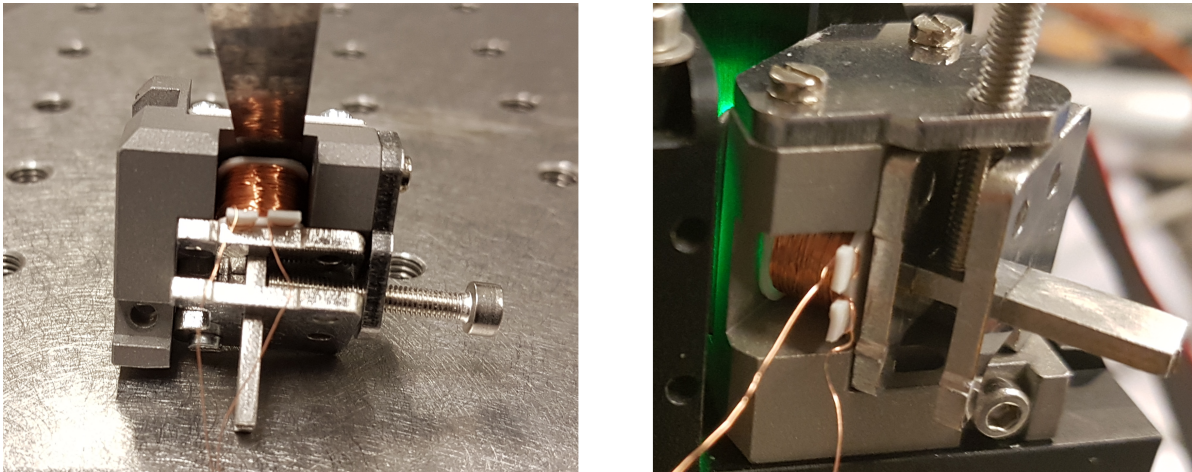


Figure 4.63: Left: Setting coil yoke position with feeler gauge. Right: Fully assembled HF scanner mounted in the OPMOD of the EasyScan

# 5

## Design validation

### 5.1. Validation outline

The main objective of validation is to find out, whether the design actually reaches the required operational parameters. Only the HF scanner prototype is built. The scanner must reach the  $\pm 3$  mrad amplitude at the operational frequency of 4650 Hz with a driving signal of  $\pm 5$  V signal. However, due to uncertainty of the flexure resonance frequency and the thin air damping, several models of flexures and housings were built. The tested models are listed in table 5.1.

Flexures		Housings	
Model	Frequency	Model	Air gap size
1	4822 Hz	1	0.5 mm
2	5153 Hz	2	0.75 mm
3	5511 Hz	2	1.0 mm

Table 5.1: Tested HF flexure and ferromagnetic housing models

Additionally, the yoke gap is also made adjustable, to find out how small the gap can be set. Moreover, there is uncertainty in the thermal heating effects of the coil. To manage all of the design variables, the validation path is set as:

- Test thermal effects on the coil by measuring the temperature of the coil surface, while increasing the current running through the coil. Determine the coil temperature increase.
- Determine the yoke gap influence on the scanner amplitude, by reducing the gap size and measuring scanner amplitude at each yoke gap distance. Determine a minimum yoke distance that does not negatively impact scanner performance. The minimum yoke distance is then set for the following tests.
- Measure the amplitude at the operating frequency of each flexure with each scanner housing. If the amplitude is not reached at the input signal of  $\pm 5$  V, the input signal is increased to  $\pm 12$  V and the amplitude is measured. Determine the resonance frequency of each flexure with each scanner housing.
- Additionally, a resonance frequency dependency on input signal was noticed during testing. Therefore, the effect was observed for a single flexure by measuring the resonance frequency and amplitude at different input signal levels.

There are in total three flexure models and three housing models, which in total make nine different scanner combinations.

### 5.2. Coil test

Various sources indicated different current density values, at which no thermal issues occur [12], [28]. The device configuration and geometry play a significant role in determining the maximum current density, therefore, the best course of action is to do a practical test, to determine the effect of different current densities.

The coil was connected to a power supply, whose voltage could be regulated. The temperature of the coil surface was measured with a thermocouple. The current running of the coil was measured with a multimeter. The results were displayed in figure 5.1.

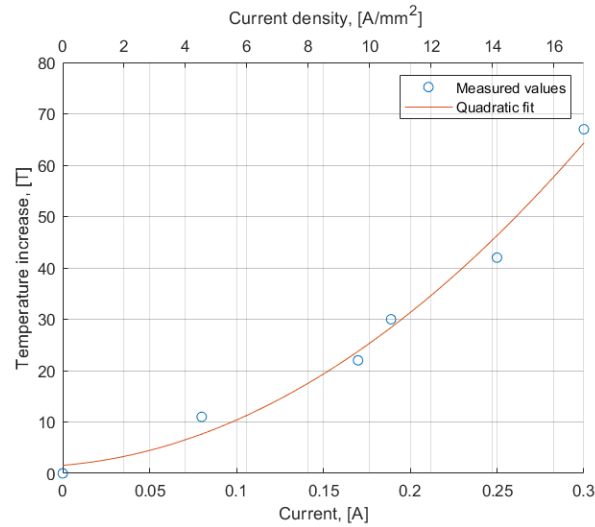


Figure 5.1: Plot of the measured temperature of the coil

The results show that at the maximum output current of the EasyScan electronics ( $I_{max} = 40\text{ mA}$ ), the coil heats up only about  $4^\circ\text{C}$ , which is not a significant amount. Increasing current to the current density of  $5\text{ A/mm}^2$  resulted in a current of about  $89\text{ mA}$  and a temperature increase of  $9^\circ\text{C}$ . At the current density of  $10\text{ A/mm}^2$ , the temperature increase of the coil was about  $25^\circ\text{C}$  and the current running through the coil was about  $0.17\text{ A}$ . Increasing the current to  $0.30\text{ A}$  resulted in the a temperature increase of about  $65^\circ\text{C}$ . After that point, the PLA bobbin started to melt. Depending on what kind of temperature increase is acceptable, the coil current can be set accordingly.

### 5.3. Scanner amplitude measurement setup

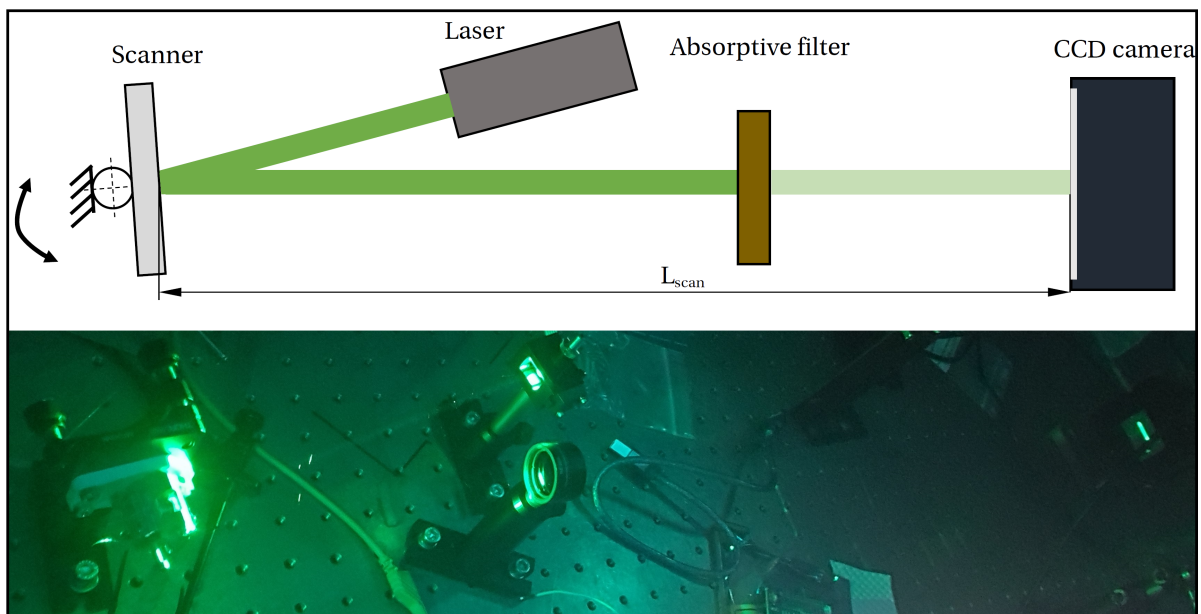


Figure 5.2: Scanner amplitude measurement test setup

The test setup used to measure the scanner's amplitude is displayed in figure 5.2. The laser used in the setup, is the same laser used in the EasyScan. The camera used for capturing images is the *Allied Vision GE4000*, which has a resolution of 4008 x 2672 pixels, with pixel size of 9  $\mu\text{m}$  x 9  $\mu\text{m}$ . The absorptive neutral density filter is used to reduce the intensity, so that the recorded image does not become saturated. The exposure time of the camera was set to 100 ms, which is around 500 times longer than the period of oscillation of the HF scanner.

The distance which the beam travels on the CCD is determined by taking three unsaturated images:

- Unsaturated image of the stationary beam.
- Unsaturated image of the moving beam.
- Background image (laser is turned off).

The background image is subtracted from both the stationary and the moving beam image to remove the intensity bias. Then, the points of highest intensity in both unsaturated images are found. The stationary beam image has one such point, due to the Gaussian distribution of the intensity. For the moving beam image, two points of maximum intensity are found. The FWHM of the beam in the row with the highest intensity is taken. If the points of highest intensity in the moving image are not in the same data row, the image is rotated. By having the FWHM of both, the stationary and moving beam the scanner amplitude can be calculated as:

$$\alpha_{scan} = \pm \frac{(FWHM_{mov} - FWHM_{stat}) d_{px}}{4L_{scan}} \quad (5.1)$$

where:

$d_{px}$  = pixel size [ $\mu\text{m}$ ]

$\alpha_{scan}$  = mechanical scan angle of scanner [mrad]

$FWHM_{mov}$  = FWHM of the moving beam [px]

$FWHM_{stat}$  = FWHM of the stationary beam [px]

$L_{scan}$  = distance between scanner and CCD camera [mm]

Stationary and moving beam images for the original HF scanner of the EasyScan are displayed in figure 5.3.



Figure 5.3: Top: stationary beam reflected from the original scanner. Bottom: moving beam reflected from the original scanner at max amplitude

## 5.4. Scanner amplitude measurement results

### 5.4.1. Yoke position influence

As mentioned in section 5.1, the first parameter to determine is the optimal coil yoke distance. Flexure 1 was used for the test, while mounted without a washer. The flexure was mounted in the housing 1, which has the lowest side air gap of 0.5 mm. For the first device test, it was decided not to use the washer in order to observe what effect the washer has on the resonant frequency. The test measurement procedure was conducted as following:

1. The yoke air gap size is set to the maximum distance of 1 mm.
2. Input signal is set to 10 V P-P.

3. The resonance frequency of the flexure is found, the image of the moving beam is read out with the CCD. If the amplitude of the moving beam does not fit in the CCD then, then the input signal voltage is reduced .
4. Yoke air gap is reduced. Steps 3 is repeated.

The measured results are displayed in figure 5.4. It was noticed during measurements that the resonance frequency shifts, when the scan amplitude is increased. This behaviour was discussed in section 4.4 and is minimum, when considering oscillations under 3 mrad, however, the effect can be more clearly observed at higher amplitudes. The investigation of this effect is discussed in more detail in section 5.4.5.

The results show that the maximum scan amplitude increases with decreased air gap size, which is expected, as the reluctance between the lower air gap and the magnet decreases, therefore, increasing the total flux supplied by the coil. At the yoke air gap value of 0.4 mm the scan amplitude reaches  $\pm 8.8$  mrad which was the maximum that the test setup could measure. The test set up was not rearranged in order to increase the measurable amplitude reach because of fear that at a higher amplitude the flexure may brake. Therefore, to reduce the gap further, the input voltage was reduced, so that the maximum scan rotation would stay at around 8.8 mrad value. The reduced voltage values are displayed on the plot.

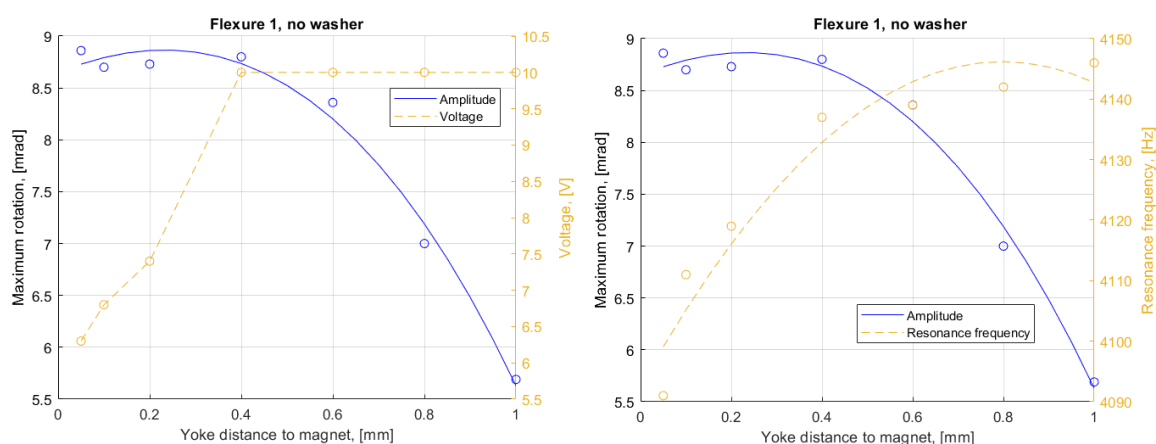


Figure 5.4: Flexure 1 mounted without a washer amplitude, while operating at the resonance frequency

During design (section 4.2.6) there was a concern, that due to the small air gap size the damping may increase. This was less of a concern for the air gap between the coil yoke and the magnet, however, there still was uncertainty. The results show that that reducing the yoke air gap at no point showed a negative effect on the scanner amplitude. Even at the smallest possible gap size of 0.05 mm, a reduction in the driving voltage was observed, when comparing to larger gap sizes. A smaller gap size was not possible to set, due to the available tooling. Additionally, setting the yoke gap at 0.05 mm proved to be difficult, due to the low stiffness of the feeler gauge. For convenience, the air gap size is set to 0.1 mm. Further testing of air gap influence on achievable amplitude was not investigated for other flexures, due to the assumption that the effect is the same for different flexures. Additionally, the same flexure was mounted with the washer to investigate the difference in the resonance frequency. The resonance frequency of the flexure with a washer was recorded as 4421 Hz, which is 275 Hz larger than the frequency without a washer. Therefore, further measurements are done with the washer mounted.

#### 5.4.2. Flexure model results

Three different versions of the flexure were designed in order to account for the uncertainty of the mounting boundary conditions (section 4.5.7). In addition, three different scanner housings were produced in order to account for the uncertainty of the small air gap (section 4.2.6). The measurement procedure for a single flexure is described as:

1. The flexure is mounted on a housing, the resonance frequency is measured at an input signal of 1 V P-P
2. A square wave signal of 10 V P-P voltage and 4650 Hz frequency is imputed, the resultant amplitude is measured.



3. If the required scan amplitude is not achieved the input signal is increased to 24 V P-P and the amplitude is measured. The value of 24V is selected because it is theoretically the largest signal value that can be achieved with the currently used 12V power supply.

The performance of each flexure was very dependant on mounting alignment and screw tightness. Therefore, it was not possible to achieve the best result with each flexure at the first mounting attempt. This phenomena is discussed in more detail in section 5.4.3. To compare the performance of each flexure the best achieved results are taken into account. Figure 5.5 illustrates the best results of each flexure.

Flexure model	Unit	Housing	Resonance frequency**, [Hz]	Amplitude, ±[mrad]	RMS current, [mA]
Flexure 1	1	1	4421	6.04	69.7
		2	4440	4.31	69.9
		3	4432	4.36	59
Flexure 2	1	1	4130	2.61	62.2
		2	4215	2.32	56.9
		3	4364	2.31	60.9
Flexure 3	1	1	4657	8.79	33.65
		2	4694	5.12*	7.02*
		3	4753	4.53	26.19
	2	1	4533	4.07	30.06
		2	4720	5.24	27.17
		3	4554	6.11	27.7
3	1	4257	3.21	62.8	
	2	4331	3.15	58.2	
	3	4320	2.2	59.3	

Amplitude required: ± 3 mrad

Reaches amplitude at 10V P-P

Reaches amplitude at 24V P-P

Does not reach amplitude at 24V P-P

Input signal frequency: 4650 Hz

Input signal shape: square

\* At input voltage of 3 V P-P, because at 10 V P-P the amplitude would exceeded the measurement range and may lead to failure.

\*\* Measured at 1 V P-P

Figure 5.5: Best recorded performance results of each flexure

Firstly, the results show that flexure 1 and 2 did not achieve the required amplitude at an input voltage of 10 V P-P. Flexure 3 unit 1 achieved the required 3 mrad amplitude with an input signal of the currently used electronics. The maximum current at which this is achieved was 33.65 mA, therefore, the electronics of EasyScan can drive these scanners. Due to the success of flexure 3, two more units of the same version flexure were tested to make a preliminary look into reproducibility of the scanner. Flexure 3 unit 2 achieved the amplitude at 10 V P-P, but unit 3 did not. The resonance frequency of unit 3 in housing 1 was measured to be 4257 Hz, which is 393 Hz away from the required 4650 Hz frequency. When comparing the flexure 3 units 1 through 3, the maximum difference between the smallest and highest recorded resonance frequency is  $\Delta_f = 496$  Hz. This difference is in the range of the frequency tolerances  $\Delta_M = \pm 441.1$  Hz estimated in section 5.5. Therefore, the under performance of flexure unit 3 is most likely a result of machining/assembly tolerances.

It is interesting to note, that the maximum recorded resonance frequency of flexure 3 unit 1 is 758 Hz smaller than theoretically predicted frequency in table 4.14, which was estimated with strict boundary conditions. Therefore, the less constricting boundary conditions are more accurate at predicting the real resonance frequency.

Theoretically, the low resonance frequency of flexures 1 and 2 could also have been a results of the frequency tolerance  $\Delta_M$ . However, the highest recorded resonance frequency of flexure 2 has a frequency tolerance margin of only 155.1 Hz. Flexure 2 was designed to have higher resonance frequency than flexure 1 by 331 Hz, but the measured results show the opposite. Therefore, it is most likely that flexure 1 was manufactured with the resonance frequency ending up in the + side of the tolerance whereas the flexure 2 ended up in the - side of the tolerance. Flexure 3 units 1 and 2 outperformed flexures 1 and 2. Only flexure 3 unit 3 showcased performance that was worse than flexure 1, which can be attributed to manufacturing tolerance. Therefore, it can be concluded that the design of flexure 3 is the closest to the required resonance frequency from the three designed flexure models.

It is worth to mention, that the amplitude that flexure 3 units 1 and 2 reaches is higher than the 3 mrad value predicted in sections 4.4 and 4.5.8. The increase in amplitude can be attributed to the decreased coil air gap size, as it increases output torque almost twice, as indicated by figure 4.12. Additionally, the lower air gap size of housing 1 increases the output torque, however, the effect is not so straightforward, and mounting also plays a significant role. The effect of different side air gap sizes is discussed in section 5.4.4.

With a 24 V P-P input signal flexure 1 also achieved the required amplitude of 3 mrad. The same is almost true for flexure 3 unit 3, however, when mounted in housing 3 the amplitude is not achieved for this model. The current at 24 V P-P varies between different models, however, the maximum values recorded was 69.7 mA. With such current the increase in temperature is less than 9 °C. The scanner was operated at the mentioned current level for five minutes and no effect on performance was noticed. This means that if modifications were made on the EasyScan electronics, the scanner could be driven at higher current, which would compensate for the frequency tolerance of the scanner.

A look at the amplitude requirement leads to an intriguing conclusion. The requirement of the 3 mrad was derived from a limited amount of measurements by adding an margin of safety. However, the maximum value ever recorded for a calibrated image was  $\pm 1.41$  mrad. All of the tested flexure and housing combinations achieve this amplitude, whether at 10 V P-P or 24 V P-P input signal. Therefore, the question is whether the 3 mrad amplitude requirement is too strict. To be able to answer this, more measurements would have to be conducted. However, reducing the requirement may be a correct solution in order to make the scanner less sensitive to the frequency tolerance  $\Delta_M$ .

### 5.4.3. Mounting influence on frequency

It was mentioned in section 5.4.3 that the performance of each flexure was very dependant on mounting alignment and screw tightness. Bad mounting results in a curved scan beam. Examples of curved scan beam are showcased in figure 5.6. Such curving of the beam is undesired, as it may influence the focusing of the image and the vertical stripe elimination capabilities of the EasyScan. The problem with avoiding these light beams is that predictive behaviour was not noticed. The screw tightness of each scanner was different from another, some flexures even requiring mounting by only two bolts. If a third bolt was used, the light beam would start to curve. Some flexure would require normal tightening torques, while others would be almost completely loose in order to have a straight light beam. The most convenient way of adjusting the screw tightness, was to do it while the scanner is turned on and the beam shape could be seen live on the sensor. However, even with this method in some cases proper tightening could not be achieved and the flexure position was needed to be adjusted. Then, the process of adjusting the screw tightness would have to be tried again.

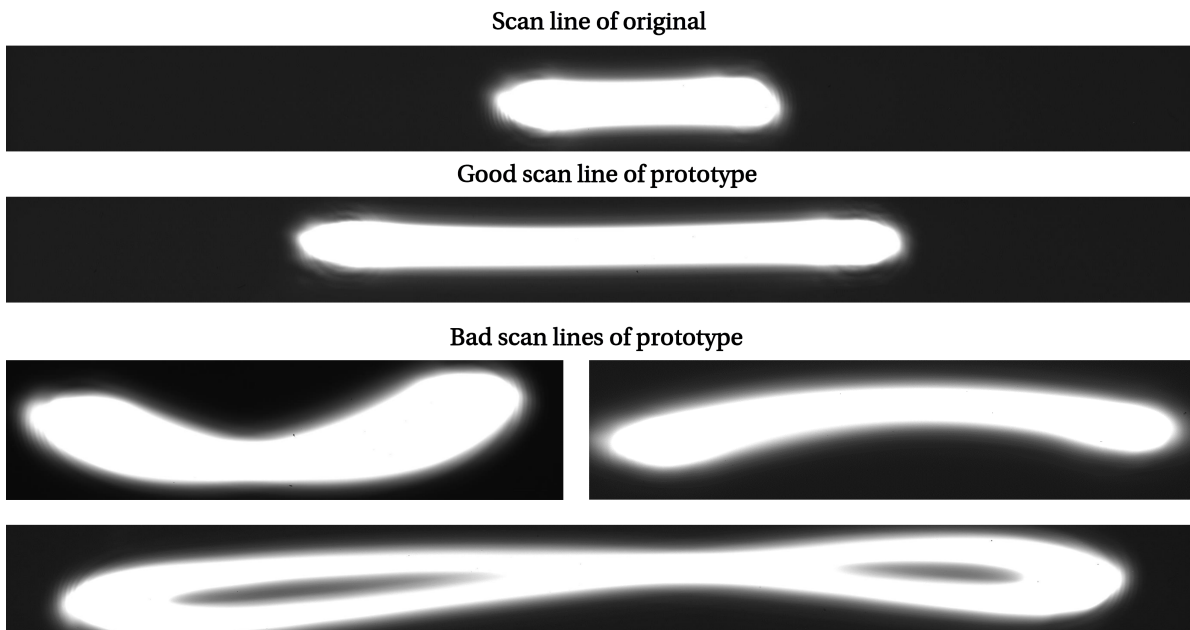


Figure 5.6: Saturated images of the scan line. The two upper scan lines are of acceptable quality. The bottom three scan lines are unacceptable and are a result of bad mounting

The cause of the beam warping is the tightening stress from the bolts. Additionally, the tightened bolt transmits not only an axial force on to the flexure, but also a torque. Theoretically, the torque can be compensated by using a torque plate, but this would require additional mounting space, which is already very limited. The only other way to avoid bolt induced stress would be to glue the flexure to the housing.

Due to the required fine tuning of the flexure mounting, the time required to do so also increases. For example, the most time consuming mounting procedure was for flexure 3 unit 3. It took 14 mounting attempts to finally achieve a straight scan line. Such long assembly times are not acceptable if you consider that the hourly wage for technical assembly in the Netherlands is 60 Eur/hour. Additionally, the difference between maximum and minimum resonance frequency measured during the mounting attempts was  $\Delta = 456$  Hz, which indicates that the frequency tolerance due to mounting is roughly half of the manufacturing/assembly tolerance  $\Delta_M = \pm 441.1$  Hz.

#### 5.4.4. Side air gap size influence

During the design process it was estimated that thin air gap may cause significant amounts of damping (section 4.2.6). Therefore, housings with side air gap sizes of 0.5 mm; 0.75 mm; 1 mm were designed in order to account for the uncertainty of damping.

Figure 5.4 shows that for flexure 1, flexure 2, and flexure 3 unit 3, the minimum gap size of 0.5 mm showed the highest amplitude. However, results are sporadic and a constant factor of how much the amplitude increases with the smallest gap size cannot be derived. This is even more true for flexure 3 units 1 and 2, for which housing 2 with air gaps of 0.75 mm showed the highest achieved amplitude.

The inconsistent behaviour of the amplitude is more a result of the mounting influence of the flexure, discussed in section 5.4.3, than that of the reduced gap size. However, since there was no obvious negative effect of the the smallest air gap size, it would be safe to conclude that an air gap size of 0.5 mm does not hinder performance.

#### 5.4.5. Frequency dependence on amplitude

It was observed that the resonance frequency of the flexure shifts with increasing amplitude. This effect is due to the non-linear negative magnetic stiffness, which was discussed in chapter 4.4. During design, it was assumed that due to the small rotation angle the non-linear magnetic stiffness can be neglected. However, this was observed for scan amplitudes lower than  $\pm 3$  mrad.

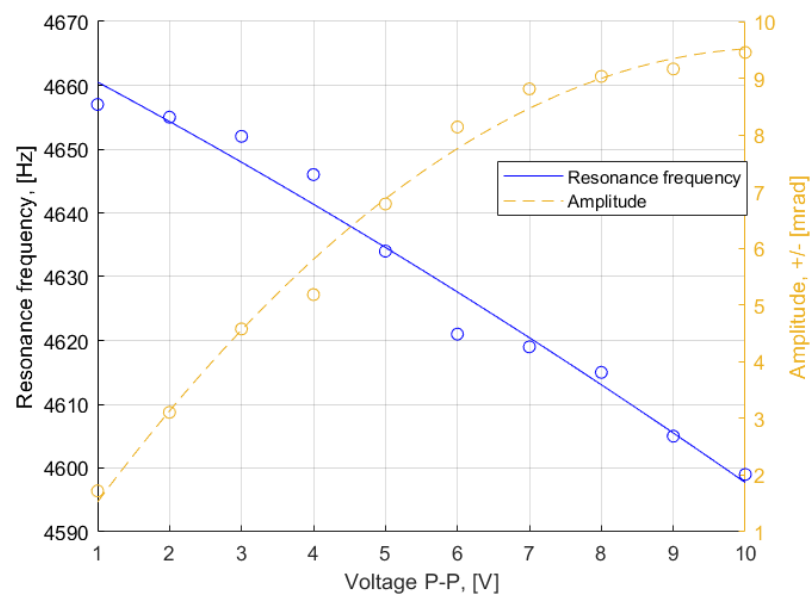


Figure 5.7: Resonance frequency dependence on input signal with a corresponding amplitude

The resonance frequency shift of flexure version 3 unit 1 was measured. The measurement procedure was:

1. Set input signal voltage is set to 1 V P-P.
2. Find the resonance frequency and measure the scan amplitude.
3. Increase the input signal voltage by 1 V P-P.

- Repeat steps 2 and 3 until the input signal voltage of 10 V P-P is reached.

The resultant plot is showcased in figure 5.7. The resonance frequency reduces with increasing amplitude. The frequency shift of  $\Delta f=60$  Hz is when there is an increase of amplitude from 1.7 mrad to 9.5 mrad. In the operational range of  $\pm 3$  mrad the change in resonance frequency is less than 10 Hz. When compared to the frequency tolerance of machining/assembly  $\Delta_M$  or the sensitivity to mounting conditions, this frequency shift phenomena becomes insignificant.

#### 5.4.6. Prototype test in the EasyScan OPMOD

The HF scanner with flexure version 3 unit 1 and housing version 1 was tested in the EasyScan OPMOD. The prototype managed to achieve the same level of image uniformity, as with the original scanner. Scanned test image comparison is displayed in figure 5.8. It is important to note, that the image illumination is a result of OPMOD alignment and not the performance of the HF scanner. Therefore, these differences do not influence the performance evaluation of the HF scanners.

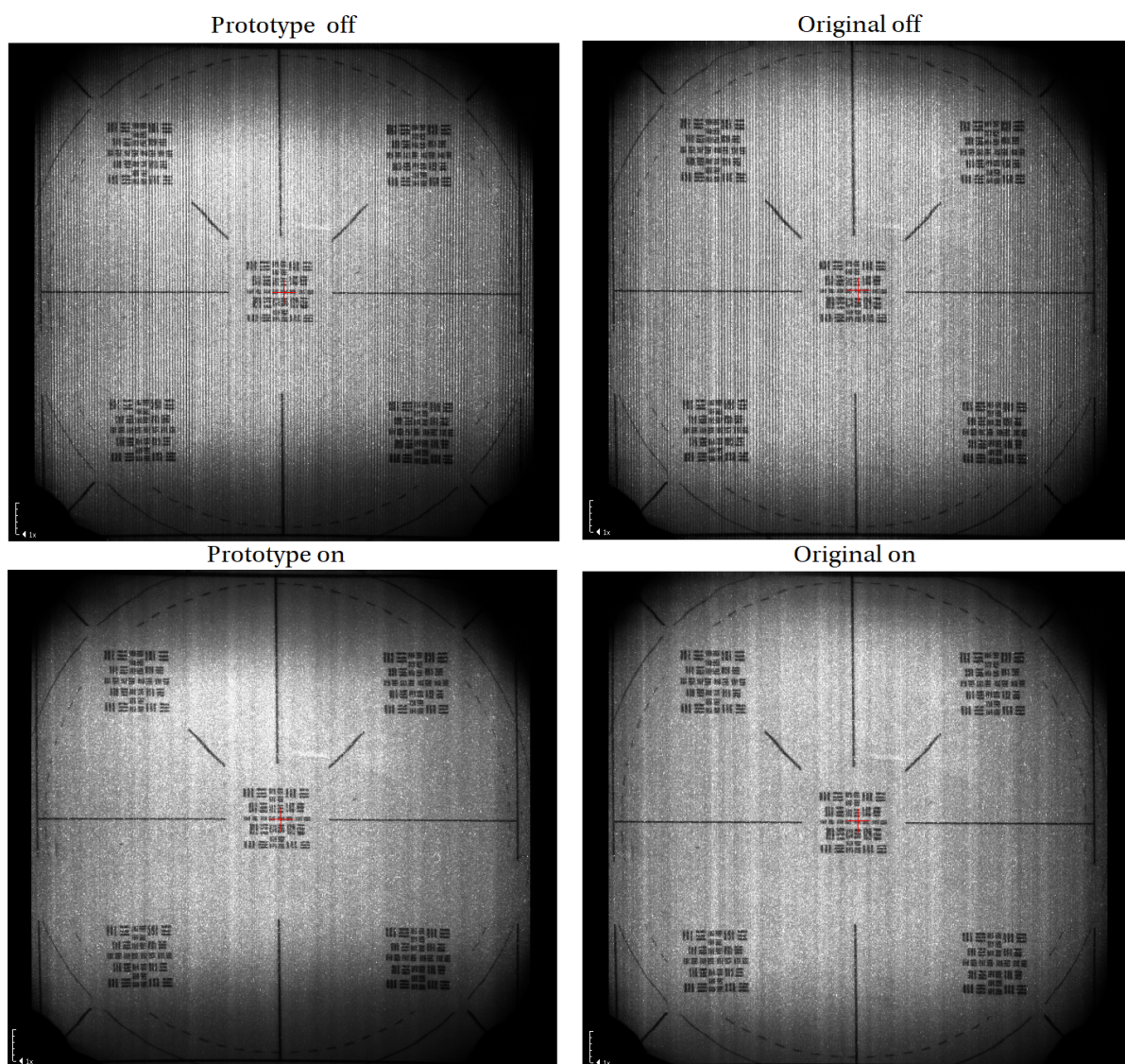


Figure 5.8: Calibrated test images for green laser of the original scanner and the prototype

The resulting image made with the prototype scanner may seem to have a slightly more uniform horizontal illumination distribution. This can be attributed to the fact that the prototype achieves a much higher amplitude than the original scanner at the lowest possible OPMOD potentiometer setting, as showcased in figure 5.9.

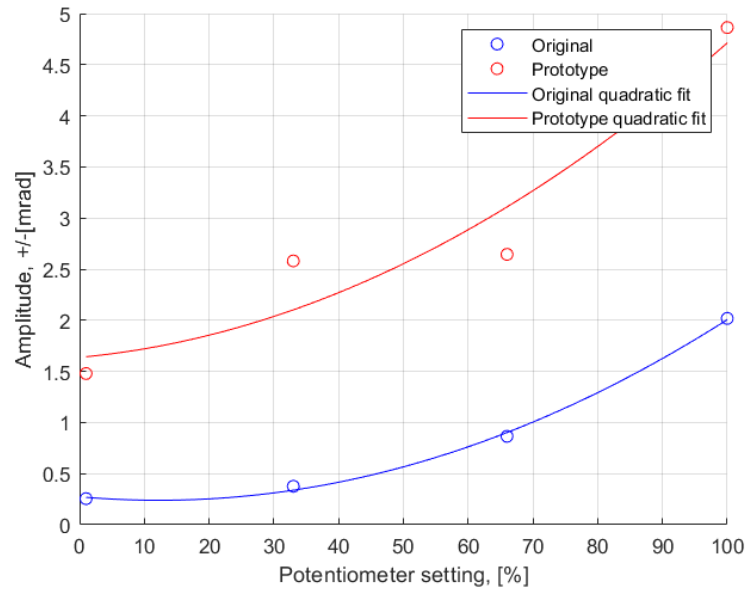


Figure 5.9: Scanning amplitude comparison between the original and the prototype scanner. Both of scanners were driven by the OPMOD and the according amplitudes are referenced to the potentiometer value of the OPMOD.

The behaviour of the prototype with respect to the potentiometer setting is also interesting, as the amplitude practically does not change between potentiometer values of 33 % and 66 %. This behaviour can be attributed to the warped beam scan path of the prototype scanner, which is a result of flexure mounting. On purpose, it was decided to test the performance of an imperfectly mounted flexure. The slightly warped beam of the HF scanner is showcased in figure 5.10.

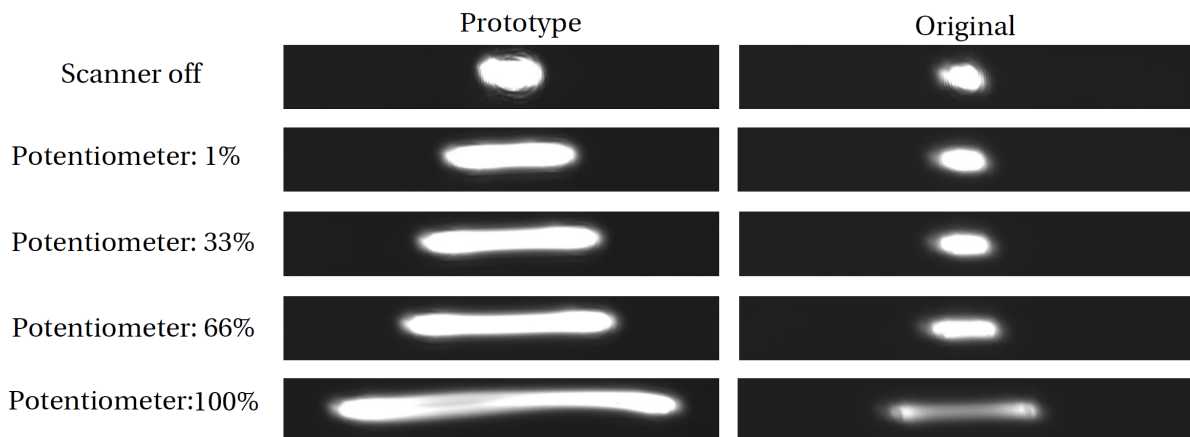
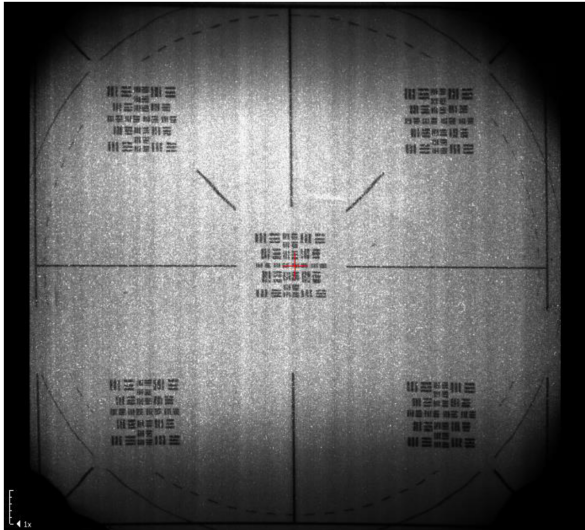


Figure 5.10: Prototype and original scanner beam shapes with respect to potentiometer setting.

Due to the design of the EasyScan electronics, the amplitude of the tested prototype could not have been lowered. This is a serious issue, as the scanner then operates at an excessive amplitude, therefore, causing a larger noise and using more power than necessary. To solve this problem, the potentiometer should be replaced by a variable resistor, so that smaller amounts of could be running through the scanner.

From figure 5.10 it can be seen the scan line of the prototype warps significantly at 100 % potentiometer setting. The effect of the warped beam on the scanned image can be seen in figure 5.11. When the beam warps, the image goes out of focus. Due to the OPMOD design, the focusing can be adjusted to refocus the beam, however, horizontal stripes appear on the bottom and top parts of the image, deteriorating image quality. More tests would need to be done to determine, how much warping is acceptable. However, generally the better approach would be to improve the mounting of the flexure in order to avoid warping all together.

Prototype: potentiometer 33%



Prototype: potentiometer 100%

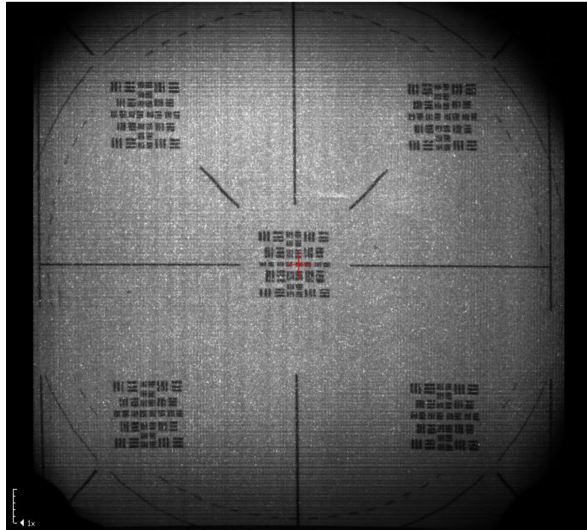


Figure 5.11: Scanned prototype test images with straight and warped beams

# 6

## Conclusion and recommendations

### 6.1. HF scanner

A prototype, which achieves the required amplitude of  $\pm 3$  mrad at the operating frequency of 4650 Hz, was developed. Design reliability was tested by manufacturing additional two units of the successful flexure model. Two out of the three flexure units achieved the required amplitude of 3 mrad. The failure of the third unit can be attributed to machining/assembly tolerances. In addition, unpredictable scanner sensitivity to mounting bolt tightness was discovered. In a recorded worst case scenario the frequency difference of the maximum and minimum recorded frequency value was 456 Hz. Furthermore, due to this spread the mounting of the flexure can take an unfeasible amount of time. A manufacturing/assembly tolerance of the resonance frequency of  $\Delta_M = 441.1$  Hz was estimated. Due to all of these factors, additional measures need to be made to ensure scanner reliability. These measures are:

1. Change the mounting of the flexure from bolting to gluing. This will remove the dependency of bolt tightness. Additionally, the cost of the scanner housing will be reduced, as tapped holes increase the price by almost 30 %. Mounting time would also be reduced, as assembling the flexure with bolts can take an unfeasible amount of time (worst case scenario recorded for a single flexure was 2 hours).
2. Improve scanner electronics so that a RMS current of at least 70 mA could be generated. This would result in less than 10 °C of a temperature increase that does not impact performance, and at least 75 % torque increase. This would help compensate for the machining/assembly tolerance  $\Delta_M$ . The coil itself can withstand a larger amount of current, therefore, a study on what is the maximum temperature increase that does not impact scanner performance is recommended.
3. The total scanner resonance frequency tolerance  $\Delta_M=441$  Hz is most dependant on sheet thickness tolerance and amounts to 84 % of the total tolerance. Therefore, improving the thickness tolerance by finding better tolerance sheet or applying additional manufacturing may drastically improve frequency tolerance. For example, reducing the thickness tolerance in half would result in 31 % reduced frequency tolerance  $\Delta_M$ .
4. Conducting a long term investigation of the in production scanners may lead to a reduction of the required scanner amplitude, as the design requirement of 3 mrad was derived from measurements of only 4 EasyScans, and is two times larger than the highest calibrated amplitude ever recorded.
5. Change the potentiometer of the HF driving electronics to a variable resistor. The potentiometer limits the minimum possible scanner current, therefore, in some cases the scanner is working at a higher oscillation amplitude, causing a larger noise than necessary.
6. The stiffness of the HF flexure can be increased, as no test resulted in failure, due to the resonance frequency being too large. This would also increase the unconstrained degree of freedom stiffness, therefore reducing warping.

## 6.2. LF scanner

The LF scanner was not fully designed, due to the poor support stiffness of the flat torsion beam. While the flat torsion beam design was feasible for the HF scanner, no feasible solutions were found in the design space of LF scanner. A conceptual design of a U shaped torsion beam was proposed, which showcased better performance than the flat torsion beam, as the higher order modes are at least 6 times larger the first mode. However, due to time constraints and limited machinability options, the design was not finished. It is recommended to further investigate manufacturing possibilities of the U shaped torsion beam in order to determine what is actually possible to manufacture and at what price.

## 6.3. Scanner cost

Many of the choices that lead to the resultant design were made in order to maintain the total cost of the scanner low. Figure 6.1 showcases the cost of each scanner component when accounting for manufacturing of 100 units.

Flexure cut with micro water jet and mounted with bolts

Part	Eur/unit
Magnet	0,20
Mirror	4,20
Coil	19,90
Coil cap + coil yoke	2,00
Flexure, (micro water jet)	14,65
Housing, (threaded)	105,00
Housing (original)	-17,51
<b>Total</b>	<b>128,44</b>

Flexure photo chemicaly etched and glued

Part	Eur/unit
Magnet	0,21
Mirror	4,20
Coil	19,90
Coil cap + coil yoke	2,00
Flexure, (etching)	3,27
Housing, (no threaded holes)	70,00
Housing (original)	-17,51
<b>Total*</b>	<b>82,07</b>

Price is estimated assuming manufacturing of 100 scanners

Target price is 150 Eur/scanner

Figure 6.1: Scanner part cost comparison

The total cost requirement for both scanners were set as 300 Eur/EasyScan. Allocating half of that amount for the HF scanner is a reasonable assumption. Additionally, because the original scanner housing is removed and replaced by the new one, the cost of the original housing can be added to increase the budget. The total price of the parts for the prototype scanner with the bolted flexure, is 128.44 Eur. This amounts to 86 % of the single scanner budget of 150 Eur. The most expensive part is the scanner housing. The prototype scanner housing is 6 times more expensive than that of the original scanner. There are several reasons for this. The original scanner is made of aluminium, which is much easier to machine than stainless steel. Secondly, the prototype scanner has in total 8 tapped M2 holes. Hole tapping for stainless steel at small screw sizes, such as M2 is a very precarious operation, which can lead to broken tap cutters. Therefore, carefully tapping the holes requires time and leads to an increased cost. Furthermore, the price of manufacturing is given by a manufacturer of European Union, which can be more expensive than countries from Asia.

If bonding with adhesive would be used instead of mounting with bolts, the cost of the housing could be reduced to 70 Eur/unit. In addition, the price of the flexure can be reduced by using photo chemical etching, instead of cutting the flexure with a micro water jet. If these changes were implemented then the total cost of the parts would be reduced to 82 Eur, leaving 68 Eur for the scanner assembly. Assuming that the price of technical assembly in the Netherlands is 60 Eur/hour, that would amount to 68 minutes of assembly time per scanner. If the assembly process was optimized, a one hour assembly time for a single scanner may seem like a reachable goal. Therefore, if gluing of the flexure would result in improved scan beam stability, then the price of a single scanner should be just about the required 150 Eur/scanner and would be feasible.



# **Appendices**



# A

## Magnetic circuit basics

### A.1. Main relations and determination of magnetic flux

Magnetomotive force (MMF) for coils and magnets is defined as:

$$\mathcal{F}_{coil} = NI \quad \mathcal{F}_{mag} = \frac{B_r l_m}{\mu_0} \quad (\text{A.1})$$

Reluctance of an element in a magnetic circuit is defined as:

$$\mathcal{R} = \frac{t}{\mu_0 \mu_r A_c} \quad (\text{A.2})$$

The magnetic flux  $\phi$  crossing a surface S is the surface integral of the normal component of  $\mathbf{B}$ :

$$\phi = \int_S \mathbf{B} \cdot d\mathbf{a} \quad (\text{A.3})$$

In most cases it is assumed that the magnetic flux density is uniform across the cross section of the yoke or an air gap, therefore A.3 simplifies to:

$$\phi = B_c S_c \quad (\text{A.4})$$

Analogous to Kirchoff's current law [11], the sum of flux in a node of a magnetic circuit is equal to zero:

$$\sum_n \phi_n = 0 \quad (\text{A.5})$$

If the magneto motive force  $\mathcal{F}_L$  and the reluctance  $\mathcal{R}_L$  of a loop are known then the flux in the loop can be expressed as:

$$\phi = \frac{\mathcal{F}_L}{\mathcal{R}_L} \quad (\text{A.6})$$

The relation of flux to MMF and reluctance in equation A.6 is analogous to Ohm's law [18], which is used in electric circuits. The voltage corresponds MMF, reluctance to resistance and current to flux. Examples of analogous circuits are showcased in figure A.1. For such a magnetic circuit the total flux would be calculated as:

$$\phi = \frac{\mathcal{F}}{\mathcal{R}_y + \mathcal{R}_g} \quad \mathcal{R}_y = \frac{2(L_1 + L_2) - t}{\mu_0 \mu_r A_c} \quad \mathcal{R}_g = \frac{t}{\mu_0 A_c} \quad \mathcal{F} = N_1 I_1 \quad (\text{A.7})$$

Usually in a good magnetic circuit the magnetic permeability of the yoke is much higher than that of vacuum  $\mu_r \gg 1$  then the reluctance of the yoke is much smaller than that of the yoke  $\mathcal{R}_y \gg \mathcal{R}_g$ . In such cases the reluctance of the yoke can be disregarded  $\mathcal{R}_t \approx \mathcal{R}_g$ .

For a more complicated circuit configuration the same equation A.6 can be used to find the fluxes. An example configuration is showcased in figure A.2. The reluctance of the yoke is disregarded. There are two inner loops to which equation A.6 can be applied.

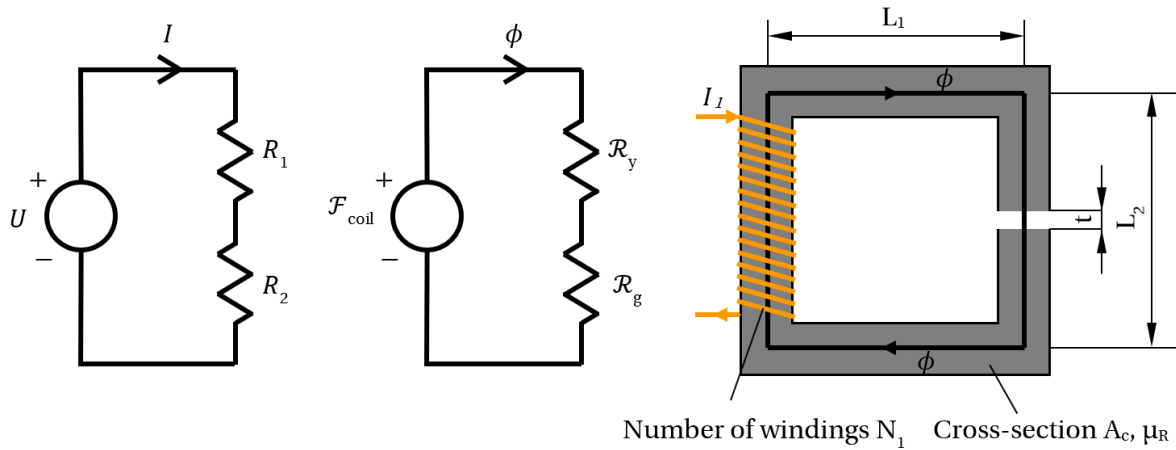


Figure A.1: Left: An arbitrary schematic of an electric circuit. Center: A magnetic circuit schematic analogous to the electric circuit on the left. Right: Configuration of magnetic circuit which corresponds to the magnetic circuit schematic.

$$\phi_1 \mathcal{R}_g + \phi_3 \mathcal{R}_m = \mathcal{F}_{mag} + \mathcal{F}_{coil1} \tag{A.8}$$

$$\phi_2 \mathcal{R}_g + \phi_3 \mathcal{R}_m = \mathcal{F}_{mag} - \mathcal{F}_{coil2} \tag{A.9}$$

If equation A.6 would be applied for the outer loop of the circuit, it would result in an equation which would not be linearly independent from equations A.8 and A.9. Because in total there are three unknowns  $\phi_1, \phi_2, \phi_3$ , a third equation is needed to solve for the unknowns. The third equation is obtained by using equation A.5 on node 1:

$$\phi_1 + \phi_2 - \phi_3 = 0 \tag{A.10}$$

Equations A.8,A.9,A.10 can be combined into a matrix form which, is a linear system of equations equivalent to the form  $\mathbf{Ax}=\mathbf{B}$ :

$$\begin{bmatrix} \mathcal{R}_g & 0 & \mathcal{R}_m \\ 0 & \mathcal{R}_g & \mathcal{R}_m \\ 1 & 1 & -1 \end{bmatrix} \begin{bmatrix} \phi_1 \\ \phi_2 \\ \phi_3 \end{bmatrix} = \begin{bmatrix} 1 & 1 & 0 \\ 1 & 0 & -1 \\ 0 & 0 & 0 \end{bmatrix} \begin{bmatrix} \mathcal{F}_{mag} \\ \mathcal{F}_{coil1} \\ \mathcal{F}_{coil2} \end{bmatrix} \tag{A.11}$$

The linear system of equations can be solved manually or with the help of software such as *MATLAB*. The method outlined for determining flux values in this example can be used in any magnetic circuit and is used throughout this thesis.

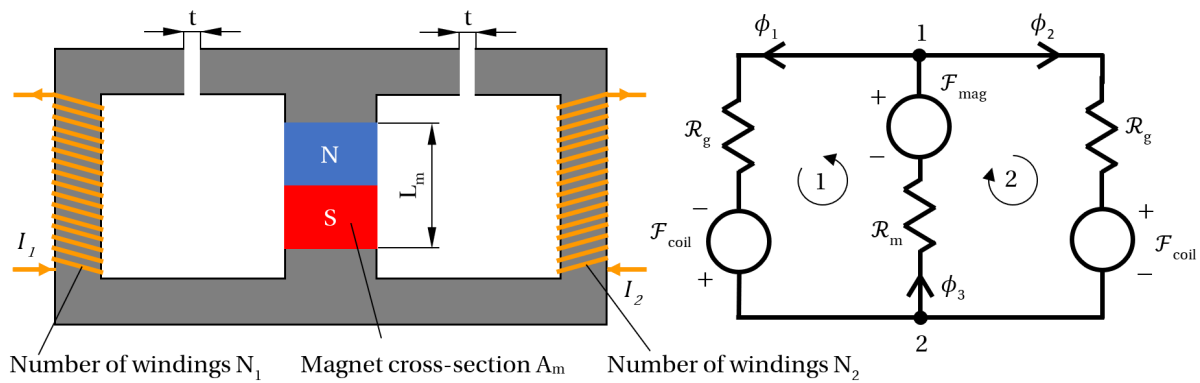


Figure A.2: Left: Magnetic circuit configuration with two loops. Right: Schematic of the magnetic circuit on the left.

## A.2. Determination of force

Two most common ways of determining magnetic forces are: the Maxwell stress tensor [13] and the energy/co-energy methods [25]. The former is used mostly in this thesis, as for the circuit configurations explored it provides the simplest expression of the force. The Maxwell stress tensor is a second order tensor expressed as:

$$\sigma_{ij} = \epsilon_0 E_i E_j + \frac{1}{\mu_0} B_i B_j - \frac{1}{2} \left( \epsilon_0 E^2 + \frac{1}{\mu_0} B^2 \right) \delta_{ij} \quad (\text{A.12})$$

where

$B_m$  = remnant magnetic flux density of the magnet [T]

$\sigma_{ij}$  = element of Maxwell stress tensor [MPa]

$\epsilon_0$  = electric constant [ $\text{F} \cdot \text{m}^{-1}$ ]

$E_i; E_j$  = electric field [V/m]

$\mu_0$  = magnetic constant [H/m]

$B_i; B_j$  = magnetic field density [T]

$E^2 = E_x^2 + E_y^2 + E_z^2$

$B^2 = B_x^2 + B_y^2 + B_z^2$

$\delta_{ij}$  = Kronecker delta. If  $i \neq j$   $\delta_{ij} = 0$ , if  $i = j$   $\delta_{ij} = 1$ .

During static operation of the reluctance actuator the electric field does not contribute to the stress tensor and during dynamic operation the contribution is insignificant therefore, it can be ignored. Then the stress tensor simplifies to:

$$\sigma_{ij} = \frac{1}{\mu_0} B_i B_j - \frac{1}{2} \left( \frac{1}{\mu_0} B^2 \right) \delta_{ij} \quad (\text{A.13})$$

When the magnetic field along the surface  $A$  of a body is known, the magnetic force acting on an object is described as:

$$F_i = \oint_A \sigma_{ij} n_j da \quad (\text{A.14})$$

where

$F_i$  = force acting on surface  $m$  [N]

$A$  = area of the surface [ $\text{m}^{-1}$ ]

$n_j$  = is the  $j$ -th component of unit vector  $\mathbf{n}$  normal to the surface  $A$  [-]

In this thesis most of the areas where the magnetic force needs, to be determined have uniform magnetic flux density normal to the area of interest. In such case, the Maxwell stress tensor has only one component which is expressed as:

$$\sigma_{xx} = \frac{1}{\mu_0} B_x B_x - \frac{1}{2} \left( \frac{1}{\mu_0} B_x^2 \right) \delta_{xx} = \frac{B_x^2}{2\mu_0} \quad (\text{A.15})$$

Then the magnetic force on a surface, which has uniform magnetic flux density normal to the surface is expressed as:

$$F_{mag.N} = \sigma_{xx} A_c = \frac{B_x^2}{2A_c \mu_0} = \frac{B_x^2 A_c}{2\mu_0} = \frac{\phi^2}{2A\mu_0} \quad (\text{A.16})$$

It is very simple to apply equation A.16 to find the magnetic force, as the only the flux  $\phi$  needs to be determined which is explained how to do in the appendix section A.1.

In situations where the net magnetic field acting on a surface also has a tangential component, the normal and the tangential forces are expressed as:

$$F_{mag.T} = \sigma_{xy} A = \frac{B_x B_y A}{\mu_0} \quad F_{mag.N} = \left( \frac{B_x^2}{\mu_0} - \frac{B_x^2 + B_y^2}{2\mu_0} \right) A = \frac{(B_x^2 - B_y^2) A}{2\mu_0} \quad (\text{A.17})$$

To properly evaluate the magnetic tensor on each surface the direction of the surface normal with respect to the axes directions of the reference coordinate system needs to be taken into account. A figure showcasing

the stress direction on a rectangular body is displayed in figure A.3. A detail explanation of the implementation of the Maxwell stress tensor can be found in [36].

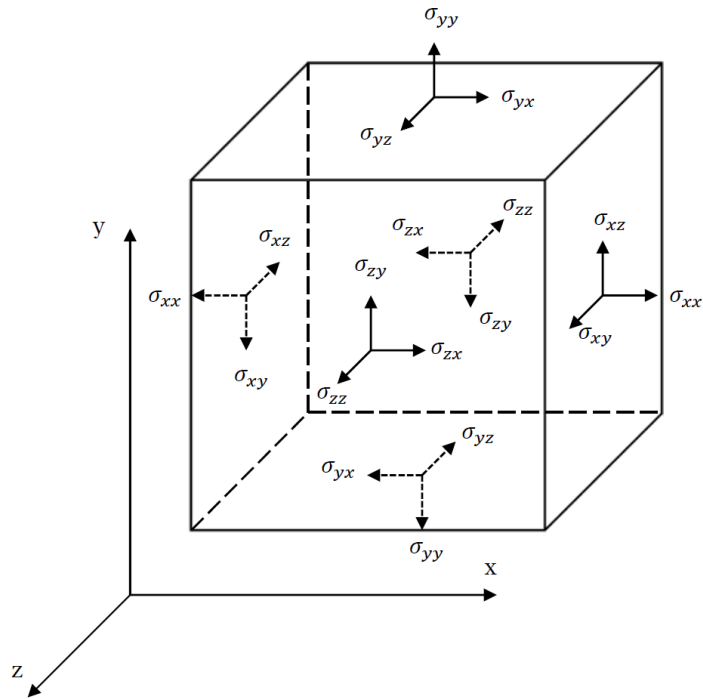


Figure A.3: Rectangular volume with stress tensor components highlighted

# B

## Piezo actuator technical data

### B.1. Maximum operational settings





Piezo actuator*	Maximum operating voltage range	Maximum operating frequency without load		Maximum power consumption
		A: Without considering thermal aspects	B: Considering thermal aspects	
				
P-882.1x	-20 V to 120 V	22.5 kHz	200 Hz	0.8 W
P-882.3x	-20 V to 120 V	15 kHz	190 Hz	1.1 W
P-882.5x	-20 V to 120 V	11.7 kHz	180 Hz	1.5 W
P-883.1x	-20 V to 120 V	22.5 kHz	170 Hz	0.9 W
P-883.3x	-20 V to 120 V	15 kHz	160 Hz	1.5 W
P-883.5x	-20 V to 120 V	11.7 kHz	150 Hz	1.9 W
P-885.1x	-20 V to 120 V	22.5 kHz	100 Hz	1.6 W
P-885.3x	-20 V to 120 V	15 kHz	90 Hz	2.6 W

Figure B.1: Maximum operating settings of various piezo actuators of *Physik Instrumente*

# C

## Magnetic circuit parameter expressions

In this appendix expressions of parameter for the magnetic circuit configurations of table 4.2. All of the expressions are derived when assuming that the scanner rotation  $x = 0$ .

### C.1. Configuration 1

Magneto motive force:

$$F_{mag} = \frac{B_r l_m}{\mu_0} \quad F_{coil} = \frac{NI}{2} \quad (C.1)$$

Reluctance:

$$R_{gapL} = R_{gapR} = \frac{g_0}{\mu_0 A_m} \quad R_m = \frac{l_m}{\mu_0 A_m} \quad R_{g_c} = \frac{g_c}{\mu_0 A_m} \quad (C.2)$$

Force:

$$F_{C1} = \frac{\Phi_L^2 - \Phi_R^2}{2\mu_0 A_m} = \frac{B_r N A_m I_c l_m}{(g_0(g_0 + 2g_c + 2l_m))} \quad (C.3)$$

### C.2. Configuration 2

Magneto motive force:

$$F_{mag} = \frac{B_r l_m}{\mu_0} \quad F_{coil} = \frac{NI}{2} \quad (C.4)$$

Reluctance:

$$R_{gapL} = R_{gapR} = \frac{g_0}{\mu_0 A_m} \quad R_m = \frac{l_m}{\mu_0 A_m} \quad R_{g_c} = \frac{g_c}{\mu_0 A_m} \quad (C.5)$$

Force:

$$F_{C2} = \frac{\Phi_L^2 - \Phi_R^2}{2\mu_0 A_m} = \frac{B_r N A_m I_c l_m}{((g_0 + l_m)(g_0 + 2g_c + l_m))} \quad (C.6)$$

### C.3. Configuration 3

Magneto motive force:

$$F_{mag} = \frac{B_r l_m}{\mu_0} \quad F_{coil} = \frac{NI}{2} \quad (C.7)$$

Reluctance:

$$R_{gapLL} = R_{gapLU} = R_{gapRU} = R_{gapRL} = \frac{g_0}{\mu_0 A_m} \quad R_m = \frac{l_m}{\mu_0 A_m} \quad (C.8)$$

Force:

$$F_{C3} = \frac{2(\Phi_L^2 - \Phi_R^2)}{2\mu_0 A_m} = \frac{B_r N A_m I_c l_m}{2g_0(g_0 + l_m)} \quad (C.9)$$



### C.4. Configuration 4

Magneto motive force:

$$F_{mag} = \frac{B_r l_m}{\mu_0} \quad F_{coil} = NI \quad (C.10)$$

Reluctance:

$$R_m = \frac{l_m}{\mu_0 A_m} \quad R_{LU} = R_{RU} = \frac{g_0}{\mu_0 A_m} \quad R_{LL} = R_{RL} = 2R_m \quad (C.11)$$

Force:

$$F_{C4} = F_5 - F_6 + F_3 + F_2 \quad F_5 = \frac{(B_5^2 - B_3^2) A_m}{2\mu_0} \quad F_6 = \frac{(B_6^2 - B_2^2) A_m}{2\mu_0} \quad F_3 = \frac{B_3 B_5 A_m}{\mu_0} \quad F_2 = \frac{B_6 B_2 A_m}{\mu_0} \quad (C.12)$$

### C.5. Configuration 5

Magneto motive force:

$$F_{mag} = \frac{B_r l_m}{\mu_0} \quad F_{coil} = NI \quad (C.13)$$

Reluctance:

$$R_{gapC} = \frac{g_0}{\mu_0 A_m} \quad R_m = \frac{l_m}{\mu_0 A_m} \quad (C.14)$$

Force:

$$F = F_{I=0,25} - F_{I=0} \quad F_{I=0} = \frac{(B_r^2 A_m l_m^2)}{\mu_0 (2g_0 + l_m)^2} \quad F_{I=0,25} = \frac{A_m (B_r l_m + NI_c \mu_0)^2}{\mu_0 (2g_0 + l_m)^2} \quad (C.15)$$

# D

## Inertia of a rectangular body

Inertia of a rectangular body about an axis  $O$  that is orthogonal to one of its faces is estimated as:

$$I = \frac{hL\rho w(h^2 + w^2 + 12x_c^2 + 12y_c^2)}{12} \quad (\text{D.1})$$

where

$I$  = mass moment of inertia [ $\text{kg} \cdot \text{m}^2$ ]

$w$  = body width [m]

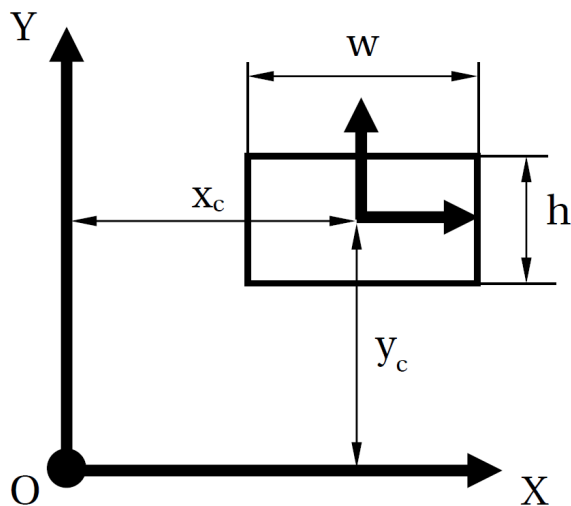
$h$  = body height [m]

$L$  = body length [m]

$x_c$  = distance between the axis of rotation and centre of mass [m]

$y_c$  = distance between the axis of rotation and centre of mass [m]

$\rho$  = material density [ $\text{kg}/\text{m}^3$ ]



Length of the body in the out of plane direction is noted as  $L$

Figure D.1: Inertia of a rectangular body about an axis  $O$

# Bibliography

- [1] Properties of stainless steel AISI430. <http://www.matweb.com/search/datasheet.aspx?matguid=1306bb472ffc40dea7b5acab1ee2f5a0&n=1&ckck=1>, .
- [2] Properties of stainless steel AISI301. <http://asm.matweb.com/search/SpecificMaterial.asp?bassnum=NL3014>, .
- [3] B-H curves for neodymium magnets. <https://www.kjmagnetics.com/bhcurves.asp>.
- [4] Technical data sheet of tough PLA by *Ultimaker*. [https://support.ultimaker.com/hc/en-us/article\\_attachments/360010175560/TDS\\_Tough\\_PLA\\_RB-en.pdf](https://support.ultimaker.com/hc/en-us/article_attachments/360010175560/TDS_Tough_PLA_RB-en.pdf).
- [5] Armco Pure Iron. [https://www.aksteel.eu/files/downloads/172888\\_armco\\_pure\\_iron\\_pdb\\_euro\\_final\\_secured\\_67.pdf](https://www.aksteel.eu/files/downloads/172888_armco_pure_iron_pdb_euro_final_secured_67.pdf).
- [6] Coercivity. <https://en.wikipedia.org/wiki/Coercivity>.
- [7] Technical information about the cross spring pivot by *Jensen precision* . <https://www.jpe-innovations.com/precision-point/cross-spring-pivot/>.
- [8] Damping ratio values of various structures by *JPE B.V.* <https://www.jpe-innovations.com/precision-point/structural-damping-properties-mechanical-systems/>.
- [9] Linear difuser of *Thorlabs*. <https://www.thorlabs.com/thorproduct.cfm?partnumber=ED1-L4100>.
- [10] Michiel Herman Mensink and Julien Coyne, 2010, *WO2012005579A2*, World Intellectual Property Organization.
- [11] Kirchhoff's circuit laws. [https://en.wikipedia.org/wiki/Talbot\\_effect](https://en.wikipedia.org/wiki/Talbot_effect).
- [12] Magnet wire. [https://en.wikipedia.org/wiki/Magnet\\_wire#Classification](https://en.wikipedia.org/wiki/Magnet_wire#Classification).
- [13] Maxwell stress tensor. [https://en.wikipedia.org/wiki/Maxwell\\_stress\\_tensor](https://en.wikipedia.org/wiki/Maxwell_stress_tensor).
- [14] Microjet Cutting services of *Flowcut* . <https://www.flowcut.com/solutions/microjet-cutting/>.
- [15] Motor constant. [https://en.wikipedia.org/wiki/Motor\\_constants](https://en.wikipedia.org/wiki/Motor_constants).
- [16] Mu-metal physical properties. <http://www.matweb.com/search/datasheet.aspx?matguid=65ed9db7ad344a5f80029a96e13008ce&ckck=1>.
- [17] Magnetic permeability. [https://en.wikipedia.org/wiki/Permeability\\_\(electromagnetism\)](https://en.wikipedia.org/wiki/Permeability_(electromagnetism)).
- [18] Ohm's law. [https://en.wikipedia.org/wiki/Ohm%27s\\_law](https://en.wikipedia.org/wiki/Ohm%27s_law).
- [19] Piezo actuator PL022 of *Physik Instrumente*. <https://www.physikinstrumente.com/en/products/piezoelectric-transducers-actuators/pl0xx-picma-chip-actuators-100800/>, .
- [20] Electrical operation of piezo actuators by *Physik Instrumente*. <https://www.physikinstrumente.com/en/technology/piezo-technology/properties-piezo-actuators/electrical-operation>, .
- [21] Retina. <https://en.wikipedia.org/wiki/Retina>.
- [22] Talbot pattern. [https://en.wikipedia.org/wiki/Talbot\\_effect](https://en.wikipedia.org/wiki/Talbot_effect).
- [23] Properties of titanium grade 5. <http://asm.matweb.com/search/SpecificMaterial.asp?bassnum=MTP641>.

- [24] Voice coils of *Akribis*. [http://www.akribis-sys.com/pro\\_detail/productId=35.html](http://www.akribis-sys.com/pro_detail/productId=35.html).
- [25] *Electric machinery*. McGraw-Hill Education, 2002. ISBN 9780070530393.
- [26] H E Boyer. *Atlas of fatigue curves*. 1 1986.
- [27] Nisbett J. K. & Shigley J. E. Budynas, R. G. *Shigley's mechanical engineering design*. New York: McGraw-Hill., 2011.
- [28] R.F.M.M. Hamelinck. *Adaptive deformable mirror : based on electromagnetic actuators*. PhD thesis, Department of Mechanical Engineering, 2010.
- [29] Jonathan B. Hopkins and Martin L. Culpepper. Synthesis of multi-degree of freedom, parallel flexure system concepts via freedom and constraint topology (fact) – part i: Principles. *Precision Engineering*, 34(2):259 – 270, 2010. ISSN 0141-6359. doi: <https://doi.org/10.1016/j.precisioneng.2009.06.008>. URL <http://www.sciencedirect.com/science/article/pii/S0141635909000920>.
- [30] In Magleby S. P. & In Olsen B. M. In Howell, L. L. *Handbook of compliant mechanisms*. Wiley, (2013).
- [31] Paul Oxley, Jennifer Goodell, and Robert Molt. Magnetic properties of stainless steels at room and cryogenic temperatures. *Journal of Magnetism and Magnetic Materials*, 321(14):2107 – 2114, 2009. ISSN 0304-8853. doi: <https://doi.org/10.1016/j.jmmm.2009.01.002>. URL <http://www.sciencedirect.com/science/article/pii/S0304885309000079>. Current Perspectives: Modern Microwave Materials.
- [32] Young W. C. & Budynas R. G. Roark, R. J. *Roark's formulas for stress and strain*. New York: McGraw-Hill, 2002.
- [33] J Schijve. *Fatigue of structures and materials*. Springer, 2008.
- [34] H. Soemers. *Design Principles for Precision Mechanisms*. Herman Soemers, 2011. ISBN 9789036531030.
- [35] T. Veijola. Simple but accurate models for squeeze-film dampers. In *SENSORS, 2007 IEEE*, pages 83–86, 2007. doi: 10.1109/ICSENS.2007.4388341.
- [36] H.H. Woodson and J.R. Melcher. *Electromechanical Dynamics - Part 2: Fields, Forces, and Motion*. John Wiley & Sons, Incorporated, 1968. URL <https://books.google.nl/books?id=325KAQAACAAJ>.